

Theoretical Description of the Forces on a Point Charge Moving Parallel to a Supported Two-dimensional Material

by

María Rosa Preciado Rivas

A thesis
presented to the University of Waterloo
in fulfillment of the
thesis requirement for the degree of
Master of Mathematics
in
Applied Mathematics

Waterloo, Ontario, Canada, 2022

© María Rosa Preciado Rivas 2022

Author's declaration

I hereby declare that I am the sole author of this thesis. This is a true copy of the thesis, including any required final revisions, as accepted by my examiners.

I understand that my thesis may be made electronically available to the public.

Abstract

A charged particle, moving at a certain distance and parallel to a target, experiences a stopping force that slows it down and an image force that deflects it towards the target's surface. In this work, we aimed to describe the forces acting on a point charge when the target is a system composed of a two-dimensional (2D) material and a semi-infinite substrate. To do so, we used an analytical model of the conductivity of the 2D material, which combines contributions coming from intra- and interband electronic transitions, paired with a simple dielectric function for the substrate in the terahertz and mid-infrared range of frequencies. We obtained an expression for the image force in terms of the energy loss function of the system using a Kramers-Kronig relation for the case of an isotropic material, illustrated using doped graphene supported with silicon carbide. This result implies that the image and stopping forces can be analyzed on an equal footing in the frequency-momentum domain. Additionally, we separated the forces into components that stem from individual plasmon-phonon hybrid modes. On the other hand, a transverse stopping force arose in the case of an anisotropic material. We found that this force, parallel to the target's surface and perpendicular to the particle's trajectory, has a magnitude comparable to the longitudinal stopping force, meaning that it should be measurable experimentally. Using doped phosphorene supported with silicon dioxide, we obtained that all forces showed speed-dependent anisotropy when the direction of motion is varied with respect to the principal axes of the 2D material's conductivity. Finally, we found that the image force became repulsive when the incident charge moves along the armchair direction of free-standing phosphorene. This implausible result stemmed from an insufficiency in the model used but is eliminated in the presence of the substrate.

Acknowledgements

First and foremost, I would like to acknowledge the work of my supervisor, Prof. Zoran Mišković. His advice, continuous support, and patience made this thesis possible. I am also deeply grateful for his guidance and invaluable lessons.

I acknowledge the contributions of my peer, Milad Moshayedi; I am thankful for being able to collaborate with him.

I also thank the graduate program coordinator, Erin Kelly, for her assistance.

Finally, I would like to express my gratitude to my family. *Agradezco infinitamente a mi mamá, Rosa Rivas Morejón, y a mis hermanos, Teodoro y Winston. Su trabajo de todos los días y el amor que me dan es lo que me permite seguir adelante.*

Dedication

I dedicate this work to my nephew Winston José, who was born when I was still writing this thesis.

Table of contents

List of figures	viii
Abbreviations	xii
1 Introduction	1
2 A charged particle moving parallel to a 2D material on a substrate	7
2.1 Induced electrostatic potential	7
2.2 Two dimensional dielectric function	12
2.3 Stopping and image forces	13
3 Modeling the polarization function for a 2D material at low frequencies	17
3.1 Polarization function in terms of the conductivity tensor	18
3.2 Optical model	18
3.2.1 Doped graphene	19
3.2.2 Doped phosphorene	21
3.2.3 Static screening due to interband electron transitions	25
3.3 Semiclassical model	27
3.3.1 Plasmon dispersion and non-local effects	27
3.3.2 Semiclassical model for doped phosphorene	28
3.3.3 Non-local effects in plasmon dispersion	30

4	Relation between image and stopping force via Kramers-Kronig relations using the energy loss function of a supported isotropic 2D material	33
4.1	Image force in terms of the energy loss function	34
4.2	Results for graphene on a silicon carbide substrate	36
5	Image force and stopping force for an anisotropic 2D material	43
5.1	Dispersion relations	44
5.1.1	Free phosphorene	45
5.1.2	Supported phosphorene	48
5.2	Force components	51
5.2.1	Dependence on speed and direction of motion	51
5.2.2	Exploring a broader parameter space	55
6	Conclusions	63
	References	68

List of Figures

2.1	(a) Representation of a two-dimensional material at the $z = 0$ plane and a substrate occupying the region $z < -h$. (b) Representation of a positively charged particle moving with velocity \mathbf{v} at a fixed distance z_0 above the material. The external charge density, ρ_{ext} , induces an areal charge density difference, $\rho_{2\text{D}}$, in the material.	8
2.2	A charged particle moves parallel to a sheet of a supported material. (a) The induced density in an isotropic material with density response function $\chi(q, \omega)$, like graphene, is expected to be symmetric with respect to an axis along the direction of the velocity of the particle. As a result, the transverse stopping force that would arise in (b) the case that the material is anisotropic with density response function $\chi(\mathbf{q}, \omega)$, like phosphorene, vanishes. We remark that the arrows represent forces with a negative sign.	15
3.1	Real part (red) and imaginary part (blue) of the interband optical conductivity along the AC (x) and the ZZ (y) axis of phosphorene, with different equilibrium densities, obtained by V. Despoja's group using <i>ab initio</i> calculations. The imaginary part is approximated by $-\alpha_j \omega$, with α_j calculated using Eq. (3.15) (green).	24
3.2	Cross sections of the dispersion surface $\omega = \omega_p(q_x, q_y)$ with the planes $q_x = 0$ (left side, $q_y < 0$) and $q_y = 0$ (right side, $q_x > 0$) for plasmon modes in free-standing phosphorene using: the Drude model (green curves), optical model (red curves) and the semiclassical model (blue curves). The two orange shaded regions indicate the continuum of e-h intraband excitations. The yellow lines show the cross sections of the plane $\omega = v(q_x \cos \theta_0 + q_y \sin \theta_0)$ enforcing the kinematic resonance for a particle moving at the speed $v = v_B$ with angles $\theta_0 = 0$ (AC direction) and $\theta_0 = -\pi/2$ (ZZ direction). The numerical values of the parameters used are listed in Chapter 5.	32

4.1	Modes $\omega_1(q)$ and $\omega_2(q)$ and weight functions $W_1(q)$ and $W_2(q)$ of plasmon-phonon hybridization in a graphene/SiC system	38
4.2	(a) Total normalized stopping force $\bar{F}_s = F_s/F_0$ as a function of the reduced speed $\bar{v} = v/v_B$ for several distances z_0 . (b) Components \bar{F}_{s1} and \bar{F}_{s2} of the total stopping force \bar{F}_s shown as a function of the reduced speed \bar{v} for several distances z_0	40
4.3	(a) Total normalized image force $\bar{F}_i = F_i/F_0$ as a function of the reduced speed $\bar{v} = v/v_B$ for several distances z_0 . (b) Components \bar{F}_{i1} and \bar{F}_{i2} of the normalized dynamic image force $\bar{F}_{i,KK}$ shown as a function of the reduced speed \bar{v} for several distances z_0	41
4.4	(a) Total normalized stopping force \bar{F}_s in the limit of zero damping and shown along with its components \bar{F}_{s1} and \bar{F}_{s2} . (b) Total normalized image force \bar{F}_i evaluated in the limit of zero damping and shown along with its components \bar{F}_{i1} , \bar{F}_{i2} and $\bar{F}_{i,\infty}$	42
5.1	(a) Isofrequency curves $\hbar\omega_p(q_x, q_y) = 50, 100, 150, 200$ and 250 meV of the dispersion relation surface for plasmon modes in free-standing phosphorene using: Drude model (green curves), optical model (red curves) and semiclassical model (blue curves). (b) Curves defined by $\omega_p(q_x, q_y) = v(q_x \cos \theta_0 + q_y \sin \theta_0)$ enforcing kinematic resonance for a particle moving above free-standing phosphorene using optical model (thick curves) and semiclassical model (thin curves) for the direction angles: $\theta_0 = 0$ (AC direction, brown curves), $\theta_0 = \pi/4$ (intermediate direction, cyan curves) and $\theta_0 = \pi/2$ (ZZ direction, navy curves), at the reduced speeds $\bar{v} = v/v_B = 0.25, 0.5, 1$ and 2 . (the curves with $\bar{v} = 2$ pass the closest to the coordinate origin for all three directions). Also shown is the circle $q = 1/(2z_0)$ with $z_0 = 2.5$ nm (yellow curve).	46
5.2	Three dispersion surfaces for plasmon-phonon hybrid modes in supported phosphorene, $\omega = \omega_{pk}(q_x, q_y)$, with $k = 1$ for the lowest-lying (cyan), $k = 2$ for the intermediate (red) and $k = 3$ for the highest-lying mode (navy), over the fourth quadrant of the (q_x, q_y) plane, with q_x and q_y oriented along the AC and ZZ directions, respectively. Also shown is a plasmon dispersion surface (gray) for free-standing phosphorene, $\hbar \rightarrow \infty$, as well as the plane $\omega = v(q_x \cos \theta_0 + q_y \sin \theta_0)$ (yellow), which enforces the kinematic resonance condition for a particle moving with the speed $v = 2 \times v_B$ in the direction with angle $\theta_0 = \pi/3$ with respect to the AC direction.	48

5.3	(a) Iso-frequency dispersion curves with $\hbar\omega = 50, 100, 150, 200$ and 250 meV for plasmon-phonon modes in phosphorene supported by a SiO_2 substrate using optical model (red curves) and semiclassical model (blue curves), and the corresponding iso-frequency lines for the plane $\omega = v_B(q_x \cos \theta_0 + q_y \sin \theta_0)$ with $\theta_0 = \pi/4$ (yellow lines). (b) Cross sections with the planes $q_x = 0$ (left side, $q_y < 0$) and $q_y = 0$ (right side, $q_x > 0$) are shown for dispersion surfaces of three plasmon-phonon modes, $\omega = \omega_{pk}(q_x, q_y)$ with $k = 1, 2, 3$ in phosphorene supported by SiO_2 using optical model (solid red curves) and semiclassical model (solid blue curves), and for the dispersion $\omega = \omega_p(q_x, q_y)$ in free phosphorene using Drude model (dashed green curves) and optical model (dashed red curves). The two grey shaded regions are the Reststrahlen bands of the SiO_2 substrate, while the two orange shaded areas are the electron-hole intraband continuum in phosphorene. Yellow lines show the cross sections for the plane $\omega = v_B(q_x \cos \theta_0 + q_y \sin \theta_0)$ with $\theta_0 = 0$ and $\theta_0 = -\pi/2$	50
5.4	Normalized longitudinal stopping force $\bar{F}_\ell = F_\ell/F_0$ as a function of the normalized speed $\bar{v} = v/v_B$ and direction angle θ_0 for a particle moving a distance $z_0 = 50$ nm above: (a) free phosphorene and (b) phosphorene supported by a SiO_2 substrate.	52
5.5	Normalized transverse stopping force $\bar{F}_t = F_t/F_0$ as a function of the normalized speed $\bar{v} = v/v_B$ and the direction angle θ_0 for a particle moving a distance $z_0 = 50$ nm above: (a) free phosphorene and (b) phosphorene supported by a SiO_2 substrate.	53
5.6	Normalized image force $\bar{F}_i = F_i/F_0$ as a function of the normalized speed $\bar{v} = v/v_B$ and the direction angle θ_0 for a particle moving a distance $z_0 = 50$ nm above: (a) free phosphorene and (b) phosphorene supported by a SiO_2 substrate.	54
5.7	Normalized forces vs the direction angle θ_0 for a particle moving a distance $z_0 = 50$ nm above free phosphorene (black curves) and phosphorene supported by a SiO_2 substrate (red curves) at the normalized speeds: $\bar{v} = 4$ (solid lines) and 9 (dashed lines) for the longitudinal stopping force \bar{F}_ℓ (a), and $\bar{v} = 2$ (solid lines) and 7 (dashed lines) for the transverse stopping force \bar{F}_t (b) and the image force \bar{F}_i (c).	56
5.8	Normalized image force \bar{F}_i as a function of reduced speed \bar{v} for a particle moving above free phosphorene at distances $z_0 = 10$ nm and 50 nm with $\theta_0 = 0$	57

5.9	Normalized image force $\overline{F}_i = F_i/F_0$ as a function of distance for a particle moving above free phosphorene with three reduced speeds \overline{v} and with direction $\theta_0 = 0$	57
5.10	Normalized longitudinal stopping force \overline{F}_ℓ as a function of reduced speed \overline{v} for a particle moving above free phosphorene at distances $z_0 = 10$ nm and 50 nm and with direction $\theta_0 = 0$	58
5.11	Normalized transverse stopping force \overline{F}_t as a function of reduced speed \overline{v} for for a particle moving above free phosphorene at distances $z_0 = 10$ and 50 nm and with direction $\theta_0 = \pi/4$	59
5.12	Normalized image force $\overline{F}_i = F_i/F_0$ as a function of: (a) the distance z_0 (in nm) for fixed normalized speed $\overline{v} = v/v_B = 5$, and (b) the normalized speed \overline{v} for fixed distance $z_0 = 20$ nm. Results are shown for a Drude model of doped phosphorene with $n = 10^{13}$ cm ⁻² where the product of the reduced electron masses is kept fixed at $\overline{m}_x^* \overline{m}_y^* = 0.149$, while their ratio $R = \overline{m}_x^*/\overline{m}_y^*$ is varied in an interval from $R = 0.1$ to $R = 1$ in steps of 0.1.	60
5.13	(a) Normalized image force $\overline{F}_i = F_i/F_0$ and (b) normalized longitudinal stopping force $\overline{F}_\ell = F_\ell/F_0$ vs normalized speed $\overline{v} = v/v_B$ with distance $z_0 = 5$ nm and the direction angles $\theta_0 = 0$ (solid lines) and $\theta_0 = \pi/2$ (dashed lines), obtained for free-standing phosphorene using: Drude model (green curves), optical model (red curves) and the semiclassical model (blue curves).	60
5.14	Normalized transverse stopping force $\overline{F}_t = F_t/F_0$ vs incidence angle θ_0 for three normalized speeds: (a) $\overline{v} = 0.5$, (b) 1 and (c) 2, with distance $z_0 = 5$ nm, obtained for free-standing phosphorene using: Drude model (green curves), optical model (red curves) and the semiclassical model (blue curves).	61
5.15	Normalized forces vs the direction angle θ_0 for a particle moving a distance $z_0 = 50$ nm above free phosphorene (black curves) and phosphorene supported by a SiO ₂ substrate (red curves), using the optical model (solid curves) and the semiclassical model (dashed curves). Panels (a) and (a') show the longitudinal stopping force \overline{F}_ℓ for the the normalized speeds $\overline{v} = 4$ and 9, respectively, panels (b) and (b') show the transverse stopping force \overline{F}_t for the speeds $\overline{v} = 2$ and 7, respectively, and panels (c) and (c') show the image force \overline{F}_i for the speeds $\overline{v} = 2$ and 7, respectively.	62

Abbreviations

2D two-dimensional 2–6

2DEG 2D electron gas 28–30

AC armchair 3, 31, 52, 65

EELS electron energy loss spectroscopy 1–3, 64

ELF energy loss function 2, 33, 34, 36, 39–42, 47, 51, 64

HREELS high resolution electron energy loss spectroscopy 1–5, 33, 65, 66

KK Kramers-Kronig 3, 34–36, 47, 55, 64

MIR mid-infrared 2–5

RPA random phase approximation 10, 17

RTA relaxation time approximation 28, 29

SiO₂ silicon dioxide 44, 48, 49, 54, 55, 65, 66

SO surface optical 37, 44

STEM scanning transmission electron microscopy 1–3

THz terahertz 1–5

TO transverse optical 36, 37, 44, 64

ZZ zigzag 3, 31, 52, 65

Chapter 1

Introduction

In experiments of [electron energy loss spectroscopy \(EELS\)](#), a target is exposed to a beam of electrons whose initial kinetic energy lies within a certain range. Some of these electrons undergo inelastic scattering, transferring energy and momentum to the target. Phonon excitations, plasmon excitations, inner shell ionizations, intra and interband electron transitions are some of the events that occur in the target depending on the energy and momentum lost by the electrons. Accordingly, the energy distribution and deflection angle of the beam of the scattered electrons provide information about the physical and chemical properties of the target.

[EELS](#) has different flavors depending on the geometry of the setup: electrons with kinetic energy of some 100 keV are typically shot perpendicularly to the sample in transmission [EELS](#), while electrons with several tens of eV are typically reflected at a certain angle with respect to the surface in reflection [EELS](#). Additionally, in [EELS](#) with aloof trajectories, electrons only interact with the sample at a distance. Another characteristic that determines the type of [EELS](#) is the range of energy loss. For example, losses larger than 50 eV usually correspond to inner shell ionizations; meanwhile, losses smaller than 50 eV provide information about the band structure and dielectric properties of the target, like the band gap and surface plasmons. [1]

Recent developments in monochromators and spectrometers have improved the resolution of the measured energy distribution to around 4.2 meV. [2] This is known as [high resolution electron energy loss spectroscopy \(HREELS\)](#) and usually takes place in a [scanning transmission electron microscopy \(STEM\)](#) setup with incident electrons in the 100 keV energy range. [3] Such an improvement in energy resolution has promising applications in surface science, like probing surface plasmons and phonons in the [terahertz \(THz\)](#) to the

mid-infrared (MIR) frequency range. Note that the THz-MIR range roughly consists of the interval of frequencies with associated energy between 1 and 500 meV. Some examples of particle-based spectroscopy techniques particularly relevant for sampling low-energy surface excitations include the vibrational and valence aloof beam EELS in a monochromated STEM, [2, 4–6] HREELS using low-energy electron reflection from surfaces in the 2-20 eV incident energy range [7–12] and grazing scattering of medium-energy ions from surfaces. [13–18] An advantage of these techniques is that they can be used to obtain the optical response of two-dimensional (2D) materials for different frequencies and momenta [19, 20] and complement other techniques that are restricted to a fixed frequency for exploring plasmon polaritons in nanostructures, such as polarization-resolved optical spectroscopies and radiating dipole sources acting as localized probes.

The energy distribution of electrons that results from EELS experiments is predominantly determined by the energy loss function (ELF), [7, 9, 21] which is expressed in terms of the frequency- and momentum-dependent complex dielectric function or permittivity of the target. The permittivity relates the induced potential, whose source is the charge density induced in the target, to the external potential, whose source is the incident electron. Generally, the real part and imaginary part of the permittivity indicate the storage of energy and dielectric loss, respectively, in the target. [22] Considering this, we can envisage how the ELF is defined in the Fourier domain as minus the imaginary part of the inverse of the dielectric function.

As expected, the induced potential gives rise to forces acting on the incident electron. In the regime of grazing incidence of reflection EELS, which have the most pronounced effects in HREELS [8, 23] and ion-surface scattering, [17] the forces can be separated considering whether they are expressed in terms of the real part or the imaginary part of the inverse of the dielectric function, which is achieved with its symmetry properties. Such distinction originates the definitions of image force and stopping force. The image force, whose investigation has a long history, [8, 14, 24–32] depends on the real part and is conservative; meanwhile, the stopping force depends on the imaginary part, or ELF, and is dissipative. The image force acts in the perpendicular direction and causes a deflection of the trajectory toward the target’s surface. On the other hand, the stopping force acts parallel to the surface and causes the slowing down of the incident particle. [16] The stopping force is of primary interest in all particle-based spectroscopies because it is directly related to the ELF of the target, however the image force can affect the interaction times of the incident particle with a surface, [8, 13] as well as the angular distributions of the scattered particles. [14, 33]

The resolution of reflection HREELS has enabled the probing of the optical response of heterostructures containing 2D materials in the THz-MIR frequency range, [12, 34–38]

with potential applications in nanoplasmonics and nanophotonics. [39–43] One of these 2D materials is graphene, the carbon-based honeycomb lattice that is one-atom thick. Namely, STEM-EELS [44] and HREELS [12] have successfully probed its collective excitations, such as plasmon [45–51] and phonon modes [52]. One of the reasons graphene has been widely studied is its exceptional mechanical, electrical and optical properties. These characteristics are explained by its band structure that places graphene as a zero-gap semiconductor, because its valence and conduction bands meet at the Dirac points of the reciprocal lattice. Another reason why graphene is of interest is the tunability of its properties. For example, the electrical capacitance and conductivity can be controlled by applying an electrostatic potential to a gate parallel to graphene. [53, 54] It has also been observed that heterostructures made of graphene, insulating spacer layers and/or a substrate exhibit strong hybridization between the sheet plasmon of doped graphene and the optical phonons of the substrate. [35, 36, 55–60] For instance, one of the most studied heterostructures is epitaxial graphene grown on a SiC substrate, which involves plasmon-phonon hybridization as probed by low-energy electron reflection under oblique incidence HREELS in the THz-MIR regime. [34–36, 38]

In these classic applications of HREELS, where the incident particle moves in a reflection geometry with grazing angle, the image force has received less attention than the stopping force because the latter is directly related to the ELF. However, it is our goal to show that the image force can be relevant in current research about plasmon-phonon hybridization in nanostructures involving 2D materials. [12, 34–38] To achieve this, we demonstrate that the image force can be expressed in terms of the ELF of the target, when the target is a layered structure of an isotropic 2D material supported by a substrate which is also isotropic along the plane parallel to the 2D material. To do so, we rely on a Kramers-Kronig (KK) relation between the imaginary and real part of the inverse of the complex dielectric function of the system and its translational invariance. We find that the resulting “shortcut” between the image force and the ELF enable us to take full advantage of a modal decomposition of the ELF and, hence, find components of the forces that correspond to individual plasmon-phonon hybrid modes. This could be especially useful for targets that support well-defined and long-lived collective excitations. Moreover, expressing the image force in terms of the ELF enables it to be analyzed on an equal footing with the stopping force.

Another 2D material of interest is phosphorene, the building block of black phosphorus (BP), [61] because it has a pronounced in-plane anisotropy. [62–67] The structure of phosphorene is a puckered honeycomb with two principal crystalline axes, known as arm-chair (AC) and zigzag (ZZ) [64, 68, 69], along which its mechanical, electrical and optical properties are exhibited with a large variation. Besides being a direct-gap semiconductor,

phosphorene has a strong anisotropic in-plane conductivity, which places it as a candidate for naturally occurring hyperbolic metasurfaces. These surfaces can support a plasmon whose isofrequency dispersion curves are hyperbolic.¹ A hyperbolic plasmon mode in phosphorene would propagate with a strong in-plane directionality and large wavenumbers, making hyperbolic metasurfaces based on phosphorene wanted for waveguiding, hyperlensing and negative refraction applications. [71] Advantages of these metasurfaces for device applications include their ease of fabrication and the tunability of their optical response. [66, 72, 73]

Theoretically, the tunability of the optical response of BP has been studied with respect to its doping density and nearby dielectrics. [74–78] Moreover, it was shown experimentally that plasmon polariton modes in BP in the MIR frequency range can be tuned by controlling its intraband transitions, which was achieved by changing the doping density in a system of BP, cladding layers of hexagonal boron nitride (hBN) and a silicon dioxide (SiO₂) substrate. [74–78] Other theoretical studies have shown that changing the density of quasi-free charge carriers can originate a transition of the plasmon polariton in phosphorene from the elliptic regime in the THz frequency range to the hyperbolic regime in the MIR frequency range. [79–82] In studies about the relation between the tunability and the direction of propagation effects of elliptic and hyperbolic plasmons induced by a stationary radiating dipole with adjustable polarization [80, 83–85], the modeling of the optical anisotropy has been aided by introducing the in-plane conductivity tensor. [75, 81] Analytical models of the optical conductivity in the THz-MIR regime have been extensively used for doped phosphorene [75, 80, 81, 83–86]. However, there are *ab initio* calculations for the conductivity over a broader range of frequencies. [87–90] Since aloof or reflection electron HREELS experiments have probed the sheet plasmon in graphene in the THz-MIR frequency range, we expect that similar techniques could probe the plasmon in doped phosphorene in both the elliptic and hyperbolic regime.

Previous theoretical works on particles traversing uniaxial crystals, which are bulk anisotropic materials like highly-oriented pyrolytic graphite [91] or hBN, [92] predict that the stopping force will have strong directionality effects because the dielectric function of the materials is anisotropic. Based on that prediction, we expect that the stopping force on an incident charge moving above an anisotropic 2D material will have two components which act in the direction of motion of the incident particle and perpendicular to it. We call these components the *longitudinal* and *transverse* stopping forces, respectively.

¹The plasmon mode on a 2D material with isotropic permittivity has circular isofrequency dispersion curves. On the other hand, an anisotropic material has elliptic curves. Furthermore, when the anisotropy of the surface is extreme, i.e., it behaves like a metal in one direction and a dielectric in the other, the isofrequency dispersion curves open into hyperbolae. [70]

A natural comparison arises between the forces on a particle probing systems with isotropic and anisotropic materials. As it will be shown in Chapter 4, the image force for an isotropic material is necessarily attractive, and the stopping force has a single component in the direction of the particle’s velocity. Therefore, it is our goal to assess the character of the image force, which is no longer *a priori* always attractive, and both the transverse and longitudinal stopping forces for a particle moving above doped phosphorene and a substrate of SiO₂ in the THz-MIR frequency regime, which should be relevant to future experiments of HREELS.

Outline

This work is organized in the following manner. In Chapter 2, we show the derivation of the image force and stopping force that act on an incident charged particle moving parallel to a system composed of a planar material on top of a semi-infinite substrate. Specifically, we derive the electrodynamic forces for the case when the 2D material is either isotropic or anisotropic. To achieve this, we solve the Poisson equation to find the induced electrostatic potential whose source is the areal induced density in the 2D material. In turn, the areal induced density is modeled to stem from the longitudinal polarization of non-interacting charges in the 2D material using a local density response function within the random phase approximation formalism. The density response function and the substrate’s permittivity define an *effective* 2D dielectric function that relates the induced electrostatic potential to the external potential whose source is the incident charged particle.

Next, in Chapter 3, we describe the analytical models that are used in this work to build the density response function or polarization function of the 2D material suitable for the THz-MIR regime of frequencies. First, we express the density response function in terms of the in-plane conductivity tensor of the 2D material. Then, we take the optical limit of the conductivity and use analytical models to describe the contributions attributed to intraband and interband electronic transitions in the 2D material. Additionally, we use a linear approximation in the static limit of the interband conductivity to account for high energy transitions. For an anisotropic material, we also show the derivation of model that accounts for non-local effects in the intraband transitions. Finally, in this chapter we also present expressions for the effective 2D dielectric function and the dispersion relations of its eigenfrequencies.

Having the theoretical background of the previous chapters, in Chapter 4 we use a Kramers-Kronig relation to derive an expression for the image force in terms of the energy loss function function of a system consisting of an isotropic 2D material, which in turn

depends on the effective 2D dielectric function. Then, we evaluate the stopping and the image force. Additionally, we show the components of the electrodynamic forces that correspond to the collective modes of the system by performing a modal decomposition of the energy loss function. To illustrate the results, we use a system consisting of doped graphene and a substrate of silicon carbide.

On the other hand, in Chapter 5 we focus on an anisotropic material using doped phosphorene supported by silicon dioxide and in comparing different models for its dielectric function. First, we calculate the dispersion relations of the collective modes and find the regimes in which they are either elliptic or hyperbolic. Then, we compute the longitudinal stopping force, transverse stopping force, and image forces as functions of the particle's trajectory parameters as speed, direction of motion and distance from the plane of the 2D material to compare the performance of the different models.

Lastly, in Chapter 6 we summarize our key findings and present our concluding remarks.

Chapter 2

A charged particle moving parallel to a 2D material on a substrate

In this chapter, we solve macroscopic Maxwell's equations in the non-retarded regime for the canonical problem of a point-like charged particle that moves along a prescribed classical trajectory, i.e., without recoil, above the surface of a layered structure. We describe several simplifying assumptions that reduce the problem at hand to the Poisson equation, which we solve for the electric potential as a function of the perpendicular coordinate, while taking the polarization functions for the constituent materials in the structure as input functions. The solution for the potential is used to derive expressions for the components of a force that acts on the charged particle as a result of the electric polarization of the structure.

2.1 Induced electrostatic potential

We use a system with Cartesian coordinates (\mathbf{r}, z) , where $\mathbf{r} = (x, y)$, and consider a sheet of a two-dimensional (2D) conductive material that is placed in the $z = 0$ plane. A semi-infinite substrate occupies the region $z \leq -h$, and the region $z > -h$ is vacuum or air, as in Ref. 93. We also consider an external point charge $+Ze$ that moves classically at constant velocity $\mathbf{v} = (v_x, v_y)$, parallel to the 2D material at a fixed distance $z_0 > 0$, so that its density is

$$\rho_{\text{ext}}(\mathbf{r}, z, t) = Ze \delta(\mathbf{r} - \mathbf{v}t) \delta(z - z_0). \quad (2.1)$$

This external charge density is the source of an external potential $\Phi_{\text{ext}}(\mathbf{r}, z, t)$ that disturbs the system and produces a change in the areal charge density of the 2D material. [94]

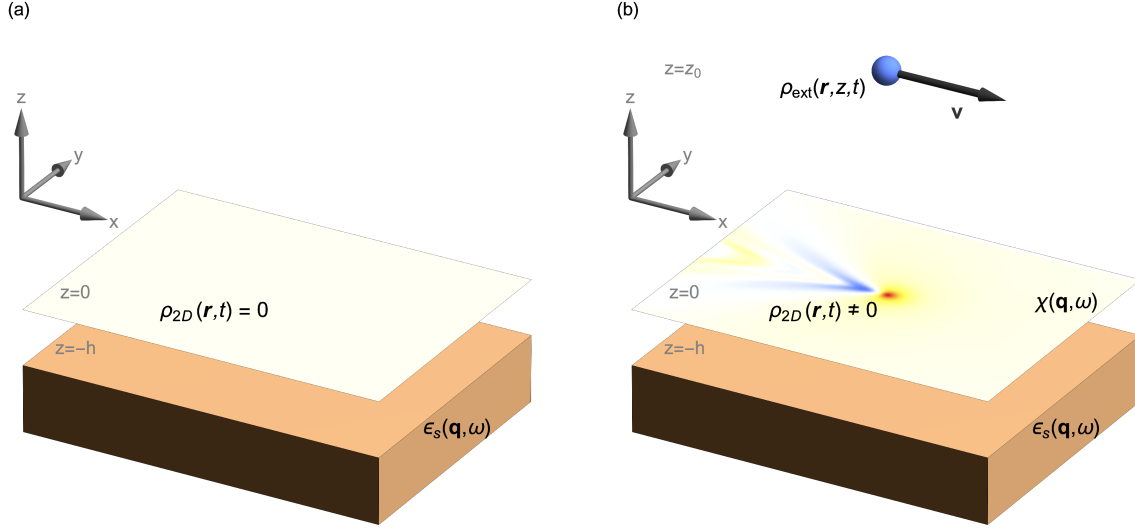


Figure 2.1: (a) Representation of a two-dimensional material at the $z = 0$ plane and a substrate occupying the region $z < -h$. (b) Representation of a positively charged particle moving with velocity \mathbf{v} at a fixed distance z_0 above the material. The external charge density, ρ_{ext} , induces an areal charge density difference, ρ_{2D} , in the material.

This difference in density is $\rho_{2D}(\mathbf{r}, t)$ or the induced charge density. Correspondingly, the induced charge density is the source of an induced potential, $\Phi_{\text{ind}}(\mathbf{r}, z, t)$ (see Fig. 2.1).

We consider that the displacement field and the electric field are described by the Maxwell's equations for matter in the so-called quasi-static regime, i.e., the effects of relativistic retardation are neglected mathematically by letting the speed of light become infinite. This results in the magnetic field becoming negligible and the displacement and electric fields being described by

$$\nabla \cdot \mathbf{D}(\mathbf{r}, z, t) = 4\pi [\rho_{\text{ext}}(\mathbf{r}, z, t) + \delta(z)\rho_{2D}(\mathbf{r}, t)] \quad (2.2)$$

and

$$\nabla \times \mathbf{E}(\mathbf{r}, z, t) = 0, \quad (2.3)$$

where Gaussian electrostatic units are used. We can see that, by Eq. (2.3), the electric field is conservative and, therefore, is the gradient of the total electrostatic potential, or

$$\mathbf{E} = -\nabla\Phi(\mathbf{r}, z, t). \quad (2.4)$$

The constitutive relation between the displacement and electric fields is generally given

by

$$\mathbf{D}(\mathbf{r}, z, t) = \int_{\mathbb{R}^2} d^2\mathbf{r}' \int_{\mathbb{R}} dz' \int_{\mathbb{R}} dt' \mathcal{E}(\mathbf{r}, \mathbf{r}', z, z', t - t') \mathbf{E}(\mathbf{r}', z', t'), \quad (2.5)$$

where \mathcal{E} is the dielectric response function of the system and vanishes for $t - t' < 0$ because of causality. For the system we are considering, a stationary layered structure, the dielectric function is restricted to depend solely on the difference of \mathbf{r} -coordinates by assuming that the layers have a large area with translational invariance along the (x, y) -plane. Additionally, we assume that the dielectric function can be spatially local with respect to the z -coordinate. That is, the dielectric response function in Eq. (2.5) is replaced by $\varepsilon(\mathbf{r} - \mathbf{r}', z, t - t')\delta(z - z')$. Consequently, we can use the convolution theorem to obtain

$$\tilde{\mathbf{D}}(\mathbf{q}, z, \omega) = \varepsilon(\mathbf{q}, z, \omega) \tilde{\mathbf{E}}(\mathbf{q}, z, \omega), \quad (2.6)$$

where ω is frequency, $\mathbf{q} = (q_x, q_y)$ is a 2D wavevector, and

$$\tilde{\mathbf{E}}(\mathbf{q}, z, \omega) = \int_{\mathbb{R}^2} d^2\mathbf{r} \int_{\mathbb{R}} dt e^{-i(\mathbf{q}\mathbf{r} - \omega t)} \mathbf{E}(\mathbf{r}, z, t) \quad (2.7)$$

is the Fourier transform of \mathbf{E} with respect to time, $t \rightarrow \omega$, and the \mathbf{r} -coordinate of space, $\mathbf{r} \rightarrow \mathbf{q}$. Accordingly, similar definitions apply for $\tilde{\mathbf{D}}$, ε (\mathcal{E}), $\tilde{\Phi}$, $\tilde{\rho}_{\text{ext}}$, and $\tilde{\rho}_{\text{ind}}$. Note that the constitutive relation is nonlocal in Eq. (2.5), a convolution of two functions; however, it is local in Eq. (2.6), a pointwise product of two functions. For our layered system, the dielectric function in Eq. (2.6) is

$$\varepsilon(\mathbf{q}, z, \omega) = \begin{cases} 1, & z > 0 \text{ or } -h < z < 0, \\ \varepsilon_s(\mathbf{q}, \omega), & z < -h, \end{cases} \quad (2.8)$$

where ε_s is the dielectric function or permittivity of the substrate.

Loosely speaking, $\nabla = (\partial/\partial x, \partial/\partial y, \partial/\partial z)$ becomes $(-iq_x, -iq_y, \partial/\partial z)$ when performing the Fourier transform in Eq. (2.7). Therefore, by combining Eqs. (2.2), (2.4), (2.6) and (2.8), we can obtain a second-order ordinary differential equation in z alone for the Fourier transform of the electrostatic potential $\tilde{\Phi}(\mathbf{q}, z, \omega)$,

$$\frac{\partial^2 \tilde{\Phi}}{\partial z^2}(\mathbf{q}, z, \omega) - q^2 \tilde{\Phi}(\mathbf{q}, z, \omega) = -\frac{4\pi}{\varepsilon(\mathbf{q}, z, \omega)} \tilde{\rho}_{\text{ext}}(\mathbf{q}, z, \omega) \quad \text{for } z \neq 0. \quad (2.9)$$

Recall that the dielectric function is not defined for $z = 0$ and that the induced density vanishes for $z \neq 0$. Eq. (2.9) is complemented by the boundary condition

$$\lim_{z \rightarrow \pm\infty} \tilde{\Phi}(\mathbf{q}, z, \omega) = 0, \quad (2.10)$$

which ensures that the solutions have *physical* significance, two matching conditions that ensure that the total electric potential is a continuous scalar function,

$$\tilde{\Phi}(\mathbf{q}, z, \omega) \Big|_{z=-h^-} = \tilde{\Phi}(\mathbf{q}, z, \omega) \Big|_{z=-h^+} \quad \text{and} \quad (2.11)$$

$$\tilde{\Phi}(\mathbf{q}, z, \omega) \Big|_{z=0^-} = \tilde{\Phi}(\mathbf{q}, z, \omega) \Big|_{z=0^+}, \quad (2.12)$$

and two other constraints that follow the well-known jump condition for the normal component of the displacement field at a boundary containing a surface charge density,[54, 95]

$$\epsilon_s(\mathbf{q}, \omega) \frac{\partial \tilde{\Phi}}{\partial z}(\mathbf{q}, z, \omega) \Big|_{z=-h^-} - \frac{\partial \tilde{\Phi}}{\partial z}(\mathbf{q}, z, \omega) \Big|_{z=-h^+} = 0 \quad \text{and} \quad (2.13)$$

$$\frac{\partial \tilde{\Phi}}{\partial z}(\mathbf{q}, z, \omega) \Big|_{z=0^-} - \frac{\partial \tilde{\Phi}}{\partial z}(\mathbf{q}, z, \omega) \Big|_{z=0^+} = 4\pi \tilde{\rho}_{2D}(\mathbf{q}, \omega). \quad (2.14)$$

Additionally, by postulating the existence of a linear density response function $\chi(\mathbf{q}, \omega)$, the induced density that surges from the dynamical, longitudinal polarization of non-interacting electrons in the 2D material is expressed in terms of the total potential evaluated at the plane $z = 0$, $\tilde{\Phi}^0(\mathbf{q}, \omega) = \tilde{\Phi}(\mathbf{q}, z = 0, \omega)$,

$$\tilde{\rho}_{2D}(\mathbf{q}, \omega) = -e^2 \chi(\mathbf{q}, \omega) \tilde{\Phi}^0(\mathbf{q}, \omega). \quad (2.15)$$

The density response function $\chi(\mathbf{q}, \omega)$ in Eq. (2.15) exists within the formalism of the [random phase approximation \(RPA\)](#).¹ [96] Note that $\tilde{\Phi}^0(\mathbf{q}, \omega)$ can be defined by means of the boundary condition in Eq. (2.12). Finally, the constitutive relation in Eq. (2.15) allows us to obtain a self-consistent solution to Eq. (2.9) when replaced in the matching condition of Eq. (2.14),

$$\frac{\partial \tilde{\Phi}}{\partial z}(\mathbf{q}, z, \omega) \Big|_{z=0^-} - \frac{\partial \tilde{\Phi}}{\partial z}(\mathbf{q}, z, \omega) \Big|_{z=0^+} = -4\pi e^2 \chi(\mathbf{q}, \omega) \tilde{\Phi}^0(\mathbf{q}, \omega). \quad (2.16)$$

To find a solution, we may decompose the total potential according to $\tilde{\Phi}(\mathbf{q}, z, \omega) = \tilde{\Phi}_{\text{ext}}(\mathbf{q}, z, \omega) + \tilde{\Phi}_{\text{ind}}(\mathbf{q}, z, \omega)$ because of the linearity of Eq. (2.9). Then, Eq. (2.9) can be

¹The RPA density response function is valid for extrinsic graphene, and it is also considered to be valid to model intrinsic graphene when it is placed on top of a suitable substrate. [96] In Ref. 97 and 98, the RPA density response function is derived for the π -electron bands near the Dirac points of graphene.

split into two equations, one for each source charge, as

$$\frac{\partial^2 \tilde{\Phi}_{\text{ext}}}{\partial z^2}(\mathbf{q}, z, \omega) - q^2 \tilde{\Phi}_{\text{ext}}(\mathbf{q}, z, \omega) = -\frac{4\pi}{\epsilon(\mathbf{q}, z, \omega)} \tilde{\rho}_{\text{ext}}(\mathbf{q}, z, \omega) \quad \text{and} \quad (2.17)$$

$$\frac{\partial^2 \tilde{\Phi}_{\text{ind}}}{\partial z^2}(\mathbf{q}, z, \omega) - q^2 \tilde{\Phi}_{\text{ind}}(\mathbf{q}, z, \omega) = 0 \quad \text{for } z \neq 0. \quad (2.18)$$

The solutions to the homogenous system associated with Eq. (2.17), e^{qz} and e^{-qz} with $q = \|\mathbf{q}\|$, and the boundary condition in (2.10) yield the Green's function [99]

$$G(q, z, z') = \begin{cases} -\frac{e^{qz'} e^{-qz}}{2q}, & -\infty \leq z' \leq z, \\ -\frac{e^{qz} e^{-qz'}}{2q}, & z \leq z' \leq \infty, \end{cases} \quad (2.19)$$

which is used to find the particular solution of Eq. (2.17) as

$$\tilde{\Phi}_{\text{ext}}(\mathbf{q}, z, \omega) = - \int_{\mathbb{R}} dz' G(q, z, z') \frac{4\pi}{\epsilon(\mathbf{q}, z', \omega)} \tilde{\rho}_{\text{ext}}(\mathbf{q}, z', \omega), \quad (2.20)$$

where

$$\tilde{\rho}_{\text{ext}}(\mathbf{q}, z, \omega) = 2\pi Z e \delta(\omega - \mathbf{q} \cdot \mathbf{v}) \delta(z - z_0), \quad (2.21)$$

which is given by the definition of the Fourier transform of the delta function. In Eq. (2.21), the external charge does not vanish when $\omega = \mathbf{q} \cdot \mathbf{v}$ and $z = z_0$. Ultimately, the expression for the external potential is

$$\tilde{\Phi}_{\text{ext}}(\mathbf{q}, z, \omega) = 2\pi Z e \delta(\omega - \mathbf{q} \cdot \mathbf{v}) \frac{2\pi}{q} e^{-q|z-z_0|}. \quad (2.22)$$

On the other hand, Eq. (2.18) for the induced potential is solved in a piecewise manner using

$$\tilde{\Phi}_{\text{ind}}(\mathbf{q}, z, \omega) = \begin{cases} A(\mathbf{q}, \omega) e^{qz} + B(\mathbf{q}, \omega) e^{-qz}, & z > 0, \\ C(\mathbf{q}, \omega) e^{qz} + D(\mathbf{q}, \omega) e^{-qz}, & -h < z < 0, \\ E(\mathbf{q}, \omega) e^{qz} + F(\mathbf{q}, \omega) e^{-qz}, & z < -h, \end{cases} \quad (2.23)$$

where the coefficients $A(\mathbf{q}, \omega)$ and $F(\mathbf{q}, \omega)$ are zero in order to satisfy the boundary condition in (2.10), and the other coefficients are determined by the matching conditions (2.11), (2.12), (2.13), and (2.16). The external potential at $z = 0$,

$$\tilde{\Phi}_{\text{ext}}^0(\mathbf{q}, \omega) = \tilde{\Phi}_{\text{ext}}(\mathbf{q}, z = 0, \omega) = 2\pi Z e \delta(\omega - \mathbf{q} \cdot \mathbf{v}) \frac{2\pi}{q} e^{-qz_0}, \quad (2.24)$$

lets us write the matching conditions as

$$E - C - De^{2qh} = 0, \quad (2.25)$$

$$C + D - B = 0, \quad (2.26)$$

$$\epsilon_s E + (\epsilon_s - 1)\tilde{\Phi}_{\text{ext}}^0 - C + De^{2qh} = 0, \quad \text{and} \quad (2.27)$$

$$\left(1 + \frac{4\pi}{q}e^2\chi\right) B + C - D = -\frac{4\pi}{q}e^2\chi\tilde{\Phi}_{\text{ext}}^0, \quad (2.28)$$

where the \mathbf{q} - and ω -dependence is dropped for brevity. The expressions for the coefficients are then

$$B = \left[\frac{1}{(1 - \Lambda)^{-1} + \Gamma} - 1 \right] \tilde{\Phi}_{\text{ext}}^0, \quad (2.29)$$

$$C = -\frac{\Gamma}{(1 - \Lambda)^{-1} + \Gamma} \tilde{\Phi}_{\text{ext}}^0, \quad (2.30)$$

$$D = \left[\frac{1 + \Gamma}{(1 - \Lambda)^{-1} + \Gamma} - 1 \right] \tilde{\Phi}_{\text{ext}}^0, \quad \text{and} \quad (2.31)$$

$$E = \left[\frac{1 + \Gamma - e^{-2qh}\Gamma}{(1 - \Lambda)^{-1} + \Gamma} - 1 \right] e^{2qh}\tilde{\Phi}_{\text{ext}}^0, \quad (2.32)$$

where

$$\Gamma \equiv \frac{2\pi}{q}e^2\chi \quad \text{and} \quad (2.33)$$

$$\Lambda \equiv \frac{\epsilon_s - 1}{\epsilon_s + 1}e^{-2qh}. \quad (2.34)$$

Finally, the induced potential for $z > 0$ is

$$\tilde{\Phi}_{\text{ind}}^>(\mathbf{q}, z, \omega) = \left\{ \frac{1}{[1 - \Lambda(\mathbf{q}, \omega)]^{-1} + \Gamma(\mathbf{q}, \omega)} - 1 \right\} \tilde{\Phi}_{\text{ext}}^0(\mathbf{q}, \omega)e^{-qz}. \quad (2.35)$$

2.2 Two dimensional dielectric function

In the constitutive relation between the displacement and electric fields of Eq. (2.5), the dielectric function \mathcal{E} is replaced by $\varepsilon(\mathbf{r} - \mathbf{r}', z - z', t - t')$ for a structure that has translational invariance in the (x, y) -plane as well as translational invariance in the z coordinate. That

would be the case for a system with no layers, for example. Consequently, a Fourier transform can be applied for all space coordinates, resulting in

$$\tilde{\Phi}'_{\text{ind}}(\mathbf{Q}, \omega) = \left(\frac{1}{\epsilon_{3\text{D}}(\mathbf{Q}, \omega)} - 1 \right) \tilde{\Phi}'_{\text{ext}}(\mathbf{Q}, \omega), \quad (2.36)$$

which stems from $\tilde{\Phi}'(\mathbf{Q}, \omega) = \tilde{\Phi}'_{\text{ext}}(\mathbf{Q}, \omega)/\epsilon_{3\text{D}}(\mathbf{Q}, \omega)$ and $\tilde{\Phi}'(\mathbf{Q}, \omega) = \tilde{\Phi}'_{\text{ext}}(\mathbf{Q}, \omega) + \tilde{\Phi}'_{\text{ind}}(\mathbf{Q}, \omega)$ and where $\mathbf{Q} = (\mathbf{q}, q_z)$.

On the other hand, we consider the induced potential at $z = 0$ for our layered structure,

$$\tilde{\Phi}^0_{\text{ind}}(\mathbf{q}, \omega) = \left\{ \frac{1}{[1 - \Lambda(\mathbf{q}, \omega)]^{-1} + \Gamma(\mathbf{q}, \omega)} - 1 \right\} \tilde{\Phi}^0_{\text{ext}}(\mathbf{q}, \omega), \quad (2.37)$$

where $\tilde{\Phi}^0_{\text{ind}}(\mathbf{q}, \omega) = \tilde{\Phi}^0_{\text{ind}}(\mathbf{q}, z \rightarrow 0, \omega)$ as given in Eq. (2.35). The relation in Eq. (2.37) resembles the relation in Eq. (2.36). By comparison, we can identify a *two dimensional* counterpart of the dielectric function $\epsilon_{3\text{D}}$, which is $\epsilon_{2\text{D}}(\mathbf{q}, \omega) = [1 - \Lambda(\mathbf{q}, \omega)]^{-1} + \Gamma(\mathbf{q}, \omega)$ or

$$\epsilon_{2\text{D}}(\mathbf{q}, \omega) = \epsilon_{\text{bg}}(q, \omega) + V_{\text{C}}(q)\chi(\mathbf{q}, \omega), \quad (2.38)$$

where $V_{\text{C}}(q) = 2\pi e^2/q$ is the Fourier transform of the in-plane Coulomb interaction energy between two electrons of charge e , and

$$\epsilon_{\text{bg}}(q, \omega) = [1 - R(q, \omega) e^{-2qh}]^{-1}, \quad (2.39)$$

is the background dielectric function with the surface response [9, 55]

$$R(q, \omega) = \frac{\epsilon_{\text{s}}(q, \omega) - 1}{\epsilon_{\text{s}}(q, \omega) + 1}.$$

We have assume in Eq. (2.38) that the substrate is isotropic in the (x, y) plane, so that non-local effects imply a dependence on $q = \|\mathbf{q}\|$ alone. Therefore, the induced potential for $z > 0$ in Eq. (2.35) is rewritten as

$$\tilde{\Phi}^0_{\text{ind}}(\mathbf{q}, z, \omega) = \left[\frac{1}{\epsilon_{2\text{D}}(\mathbf{q}, \omega)} - 1 \right] \tilde{\Phi}^0_{\text{ext}}(\mathbf{q}, \omega) e^{-qz}. \quad (2.40)$$

2.3 Stopping and image forces

Having calculated the induced electrostatic potential for the region in which the charged particle is restricted to move, it is straightforward to derive the forces acting on the particle.

Namely, the total force is obtained from the induced electric field, upon substitution of $\mathbf{r} = \mathbf{v}t$ and $z = z_0$, as $\mathbf{F} = Ze\mathbf{E}_{\text{ind}}(\mathbf{v}t, z_0, t)$, where

$$\begin{aligned}\mathbf{E}_{\text{ind}}(\mathbf{r}, z, t) &= - \left(\nabla_{\mathbf{r}} + \hat{\mathbf{z}} \frac{\partial}{\partial z} \right) \Phi_{\text{ind}}^>(\mathbf{r}, z, t), \\ &= - \int_{\mathbb{R}^2} \frac{d^2\mathbf{q}}{(2\pi)^2} \int_{\mathbb{R}} \frac{d\omega}{2\pi} e^{i(\mathbf{q}\cdot\mathbf{r} - \omega t)} \left(i\mathbf{q} + \hat{\mathbf{z}} \frac{\partial}{\partial z} \right) \tilde{\Phi}_{\text{ind}}^>(\mathbf{q}, z, \omega),\end{aligned}\quad (2.41)$$

with $\tilde{\Phi}_{\text{ind}}^>(\mathbf{q}, z, \omega)$ given in Eq. (2.40) and $\hat{\mathbf{z}}$ being a unit vector in the direction of the z axis. Taking into account the symmetry property of the 2D dielectric function, $\epsilon_{2\text{D}}(-\mathbf{q}, -\omega) = \epsilon_{2\text{D}}^*(\mathbf{q}, \omega)$,² which ensures that the real part is even and the imaginary part is odd, the total force is decomposed into a parallel and a perpendicular component, according to $\mathbf{F} = \mathbf{F}_{\parallel} + \hat{\mathbf{z}}F_{\text{i}}$, where

$$\mathbf{F}_{\parallel} = \frac{(Ze)^2}{2\pi} \int_{\mathbb{R}^2} d^2\mathbf{q} e^{-2qz_0} \hat{\mathbf{q}} \Im \left[\frac{1}{\epsilon_{2\text{D}}(\mathbf{q}, \mathbf{q}\cdot\mathbf{v})} \right] \quad (2.42)$$

is the *stopping force* with $\hat{\mathbf{q}} = \mathbf{q}/q$, and

$$F_{\text{i}} = \frac{(Ze)^2}{2\pi} \int_{\mathbb{R}^2} d^2\mathbf{q} e^{-2qz_0} \Re \left[\frac{1}{\epsilon_{2\text{D}}(\mathbf{q}, \mathbf{q}\cdot\mathbf{v})} - 1 \right] \quad (2.43)$$

is the *image force*. Notice that the designation of stopping and image forces stems from the fact that they are expressed in terms of the imaginary and real parts of the inverse of the 2D permittivity $\epsilon_{2\text{D}}(\mathbf{q}, \omega)$, respectively. [101] Also notice that the frequency in Eqs. (2.42) and (2.43) is substituted according to $\omega = \mathbf{q}\cdot\mathbf{v}$, which stems from the Dirac delta function in Eq. (2.22), and expresses Galilean kinematic resonance between the layer's and particle's frames of reference. The stopping force acts parallel to the surface and slows down the particle; meanwhile, the image force acts in the perpendicular direction and deflects the trajectory of the particle towards the surface. These forces are observed in the regime of glancing incidence of a charged particle upon a target surface. [16]

If the direction of the velocity \mathbf{v} is defined by an angle θ_0 with respect to the x axis, so that $v_x = v \cos \theta_0$ and $v_y = v \sin \theta_0$, then the frequency is substituted according to $\omega = \mathbf{q}\cdot\mathbf{v} = v(q_x \cos \theta_0 + q_y \sin \theta_0)$ in Eqs. (2.42) and (2.43). This substitution is crucial for the emergence of directionality effects. Furthermore, it is physically revealing to decompose the

²If a function $f(t)$ is real, then its Fourier transform $\tilde{f}(\omega)$ satisfies the reality condition, $\tilde{f}(-\omega) = \tilde{f}^*(\omega)$. This means that $\epsilon_{2\text{D}}(\mathbf{q}, \omega)$ is the Fourier transform of a real function $\epsilon_{2\text{D}}(\mathbf{r} - \mathbf{r}', t - t')$, which is true for any susceptibility with physical meaning. [100]

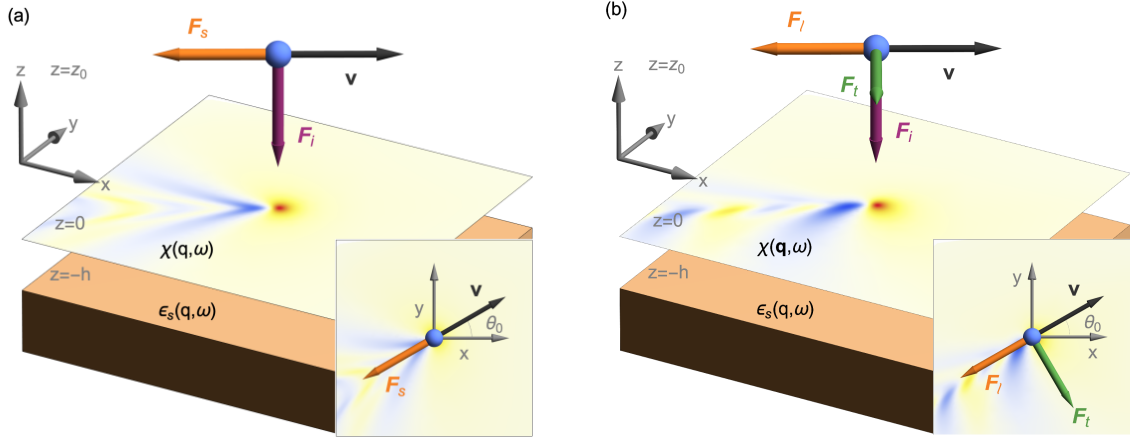


Figure 2.2: A charged particle moves parallel to a sheet of a supported material. (a) The induced density in an isotropic material with density response function $\chi(q, \omega)$, like graphene, is expected to be symmetric with respect to an axis along the direction of the velocity of the particle. As a result, the transverse stopping force that would arise in (b) the case that the material is anisotropic with density response function $\chi(\mathbf{q}, \omega)$, like phosphorene, vanishes. We remark that the arrows represent forces with a negative sign.

stopping force into a *longitudinal component*, F_ℓ , and *transverse component*, F_t , according to $\mathbf{F}_\parallel = \hat{\mathbf{v}}F_\ell + (\hat{\mathbf{z}} \times \hat{\mathbf{v}})F_t$, where $\hat{\mathbf{v}} = \mathbf{v}/v$. Accordingly, we may write $\hat{\mathbf{q}} = \hat{\mathbf{v}} \cos(\theta - \theta_0) + (\hat{\mathbf{z}} \times \hat{\mathbf{v}}) \sin(\theta - \theta_0)$ and switch to polar coordinates for integration over the wavevector $\mathbf{q} = (q, \theta)$ in both Eqs. (2.42) and (2.43), to finally express the three force components as

$$F_\ell = \frac{(Ze)^2}{2\pi} \int_0^\infty dq q e^{-2qz_0} \int_0^{2\pi} d\theta \cos(\theta - \theta_0) \Im \left[\frac{1}{\epsilon_{2D}(q, \theta, \mathbf{q} \cdot \mathbf{v})} \right], \quad (2.44)$$

$$F_t = \frac{(Ze)^2}{2\pi} \int_0^\infty dq q e^{-2qz_0} \int_0^{2\pi} d\theta \sin(\theta - \theta_0) \Im \left[\frac{1}{\epsilon_{2D}(q, \theta, \mathbf{q} \cdot \mathbf{v})} \right], \quad (2.45)$$

$$F_i = \frac{(Ze)^2}{2\pi} \int_0^\infty dq q e^{-2qz_0} \int_0^{2\pi} d\theta \Re \left[\frac{1}{\epsilon_{2D}(q, \theta, \mathbf{q} \cdot \mathbf{v})} - 1 \right], \quad (2.46)$$

where the frequency to be substituted in the 2D dielectric permittivity $\epsilon_{2D}(q, \theta, \omega)$ is given by $\omega = \mathbf{q} \cdot \mathbf{v} = qv \cos(\theta - \theta_0)$. See Fig. 2.2(b) for a depiction of the listed forces.

While the above expressions for the forces on the moving particle are generally valid for an anisotropic 2D material with a density response function $\chi(\mathbf{q}, \omega)$ that depends on the direction of the wavevector \mathbf{q} , a significant simplification occurs for an isotropic material, with a density response function $\chi(q, \omega)$ that does not depend on the direction

of the wavevector \mathbf{q} . In particular, the transverse stopping force F_t vanishes by symmetry whereas the longitudinal force is reduced to the well-known concept of stopping force in an isotropic medium, $F_t \equiv F_s$. Thus, we can write

$$F_s = \frac{(Ze)^2}{2\pi} \int_{\mathbb{R}^2} d^2\mathbf{q} e^{-2qz_0} \hat{\mathbf{q}} \cdot \hat{\mathbf{v}} \Im \left[\frac{1}{\epsilon_{2D}(q, \mathbf{q} \cdot \mathbf{v})} \right], \quad (2.47)$$

$$F_i = \frac{(Ze)^2}{2\pi} \int_{\mathbb{R}^2} d^2\mathbf{q} e^{-2qz_0} \Re \left[\frac{1}{\epsilon_{2D}(q, \mathbf{q} \cdot \mathbf{v})} - 1 \right], \quad (2.48)$$

where we have indicated that the effective dielectric function only depends of the wavenumber and frequency, $\epsilon_{2D}(q, \omega)$ and $\omega = \mathbf{q} \cdot \mathbf{v} = qv \cos \theta$. We can see in Fig. 2.2(a) a representation of the simplified problem in the case of an isotropic 2D material.

Chapter 3

Modeling the polarization function for a 2D material at low frequencies

The RPA density response function $\chi(\mathbf{q}, \omega)$, or longitudinal polarization function, as in Eqs. (2.15) and (2.38), is crucial to the linear response theory of layered structures involving 2D materials. [102] In its quantum mechanical formulation, the polarization function can be obtained by using the Lindhard function [103], which has been calculated with different methods for 2D materials. One of these methods includes a full band structure within the tight-binding approximation of graphene. [104] With more sophisticated and accurate methodology, the polarization function is obtained using *ab initio* calculations based on time-dependent density functional theory for graphene [47] and phosphorene [90]. Alternatively, various approximations can be invoked retaining only the relevant electron energy band structure of the material. Namely, the polarization function has been calculated using the so-called Dirac cone approximation for the bands of π electrons in doped graphene [97, 98] and using a reduced Hamiltonian for low-energy electronic excitations in doped phosphorene [75, 105]. In this work, however, the polarization function is estimated by using the conductivity tensor $\overleftrightarrow{\sigma}(\mathbf{q}, \omega)$, in order to incorporate the in-plane anisotropy of the 2D material.

3.1 Polarization function in terms of the conductivity tensor

The relation between the two stems from the in-plane Ohm's law in the Fourier domain given by

$$\tilde{\mathbf{J}}_{2\text{D}}(\mathbf{q}, \omega) = \overleftrightarrow{\sigma}(\mathbf{q}, \omega) \cdot \tilde{\mathbf{E}}_{\parallel}^0(\mathbf{q}, \omega), \quad (3.1)$$

where the in-plane charge current density in the 2D material induced by the presence of an external charge source, $\tilde{\mathbf{J}}_{2\text{D}}(\mathbf{q}, \omega)$, is proportional to the tangential component of the total electric field evaluated at $z = 0$, $\tilde{\mathbf{E}}_{\parallel}^0(\mathbf{q}, \omega) = -i\mathbf{q}\tilde{\Phi}^0(\mathbf{q}, \omega)$. We invoke the continuity equation, which relates the induced charge density in the 2D material with the induced current density, also in the Fourier domain, $\omega\tilde{\rho}_{2\text{D}}(\mathbf{q}, \omega) = \mathbf{q} \cdot \tilde{\mathbf{J}}_{2\text{D}}(\mathbf{q}, \omega)$. Thus, by replacing this last expression in Eqs. (2.15) and (3.1), we can express the polarization function in terms of the in-plane conductivity tensor as

$$\chi(\mathbf{q}, \omega) = \frac{i}{e^2\omega} \mathbf{q} \cdot \overleftrightarrow{\sigma}(\mathbf{q}, \omega) \cdot \mathbf{q}. \quad (3.2)$$

The conductivity tensor can be written in a basis given by the unit vectors $\hat{\mathbf{x}}$ and $\hat{\mathbf{y}}$, which are along the x and y axes, as

$$\overleftrightarrow{\sigma}(\mathbf{q}, \omega) = \begin{pmatrix} \sigma_{xx}(\mathbf{q}, \omega) & \sigma_{xy}(\mathbf{q}, \omega) \\ \sigma_{yx}(\mathbf{q}, \omega) & \sigma_{yy}(\mathbf{q}, \omega) \end{pmatrix}, \quad (3.3)$$

with the coefficients satisfying certain symmetry conditions. [106, 107]

3.2 Optical model

We are interested in finding an expression for the polarization function in the limit of low frequencies and small wavenumbers q . This approximation is well suited for frequencies ranging from the THz to mid-infrared (MIR) regime, which is technologically relevant. [39–43] By taking the limit $\mathbf{q} \rightarrow \mathbf{0}$ in the components of the in-plane conductivity tensor $\sigma_{ij}(\mathbf{q}, \omega)$, we neglect the non-local effects in the 2D material. This is known as the *optical response*. In this regime, the conductivity tensor becomes diagonalizable; [75, 90, 105] the off-diagonal elements vanish, $\sigma_{xy} = \sigma_{yx} = 0$, whereas the diagonal elements become a

function of the frequency only, $\sigma_{xx} = \sigma_x(\omega)$ and $\sigma_{yy} = \sigma_y(\omega)$. Thus, the density response function in the optical limit is

$$\chi(\mathbf{q}, \omega) = \frac{i}{e^2 \omega} [q_x^2 \sigma_x(\omega) + q_y^2 \sigma_y(\omega)]. \quad (3.4)$$

Eq. (3.4) may be more conveniently written by switching to polar coordinates for the wavevector, $\mathbf{q} = (q, \theta)$, as $\chi(q, \theta, \omega) = i \frac{q^2}{e^2 \omega} \sigma(\theta, \omega)$, where $q = \sqrt{q_x^2 + q_y^2}$ and the angle-dependent optical conductivity in the optical limit is

$$\sigma(\theta, \omega) = \sigma_x(\omega) \cos^2 \theta + \sigma_y(\omega) \sin^2 \theta. \quad (3.5)$$

For an isotropic 2D material, the diagonal components of the in-plane conductivity are equal and correspond to the scalar optical conductivity of the material, $\sigma_x(\omega) = \sigma_y(\omega) = \sigma(\omega)$. This will be the case of doped graphene. [106, 108] In the case of a material showing anisotropy, the diagonal components generally differ, $\sigma_x(\omega) \neq \sigma_y(\omega)$. For doped phosphorene, the x and y components of the conductivity can be taken along the armchair (AC) and zigzag (ZZ) directions, respectively, so that the polar angle θ is taken with respect to the AC direction. [90, 105]

As it has been shown for the longitudinal polarization function in its quantum mechanical formulation, [60, 90] the diagonal components of the conductivity tensor in the optical limit can be decomposed into contributions coming from *intraband* and *interband electron transitions*,

$$\sigma_j(\omega) = \sigma_j^{\text{intra}}(\omega) + \sigma_j^{\text{inter}}(\omega) \quad \text{for } j = x, y. \quad (3.6)$$

It turns out that the intraband and interband contributions to the conductivity tensor components of 2D materials can be calculated for frequencies in the THz-MIR range with relatively simple phenomenological models. [75, 90, 108–111] Below, we illustrate the cases of doped graphene, an isotropic material, and of doped phosphorene, an anisotropic material.

3.2.1 Doped graphene

The Dirac cone approximation is used to model the conduction and valence electronic bands of graphene near the K points of the Brillouin zone, and it yields a good description of the nearly-free π electrons of the material. [112, 113] In this approximation, the electron energy dispersion is given by a linear relation with the momentum of the electron's Bloch wave in the (x, y) plane, $p = \hbar k = \sqrt{p_x^2 + p_y^2}$. That is $\varepsilon_{\mathbf{p}} = \pm v_F p$, where $v_F \approx c/300$ is

the Fermi speed that defines the opening of the Dirac cones. Considering that graphene is doped with an equilibrium electron (or hole) areal density n , the Dirac cone approximation is used to calculate the intraband and interband contributions to its scalar conductivity as

$$\sigma_{\text{D}}^{\text{intra}}(\omega) = i \frac{v_{\text{B}}}{\pi} \frac{\omega_{\text{F}}}{\omega + i\gamma} \quad (3.7)$$

and

$$\sigma_{\text{D}}^{\text{inter}}(\omega) = i \frac{v_{\text{B}}}{4\pi} \ln \left(\frac{2\omega_{\text{F}} - \omega - i\gamma}{2\omega_{\text{F}} + \omega + i\gamma} \right), \quad (3.8)$$

where $v_{\text{B}} = e^2/\hbar \approx c/137$ is the Bohr velocity and $\omega_{\text{F}} = \varepsilon_{\text{F}}/\hbar = v_{\text{F}}k_{\text{F}}$ is the frequency related to the Fermi energy ε_{F} , with $k_{\text{F}} = \sqrt{\pi|n|}$ being the Fermi wavenumber, whereas γ is a phenomenological damping rate. The intraband contribution in Eq. (3.7) is given by the widely used Drude model, which has been confirmed to accurately describe this contribution in *ab initio* calculations [60]. As regards the interband transitions, the contribution in Eq. (3.8) is better understood in the limit of zero damping, which yields

$$\sigma_{\text{D}}^{\text{inter}}(\omega) = \frac{v_{\text{B}}}{4} \left[H(|\omega| - 2\omega_{\text{F}}) + \frac{i}{\pi} \ln \left| \frac{\omega - 2\omega_{\text{F}}}{\omega + 2\omega_{\text{F}}} \right| \right], \quad (3.9)$$

where $H(\cdot)$ is the Heaviside unit step function. The first term in Eq. (3.9) corresponds to the Pauli blocking of interband transitions in graphene. This means that transitions are mostly suppressed for $|\omega| < 2\omega_{\text{F}}$. And, by using the Kramers-Kronig relations, the second, imaginary term follows from the first, real term. When $n = 0$, that is for intrinsic or undoped graphene, $\sigma_{\text{D}}^{\text{intra}}(\omega) \rightarrow 0$ and $\sigma_{\text{D}}^{\text{inter}}(\omega) \rightarrow v_{\text{B}}/4$, which is the universal conductivity of intrinsic graphene. [109] The *Dirac conductivity* $\sigma_{\text{D}}(\omega) = \sigma_{\text{D}}^{\text{intra}}(\omega) + \sigma_{\text{D}}^{\text{inter}}(\omega)$ has been verified to yield plasmon dispersion curves that compare extremely well to those obtained by means of *ab initio* calculations in the THz-MIR regime for graphene doped with typical densities around $n = 10^{13} \text{ cm}^{-2}$, so that $\varepsilon_{\text{F}} \approx 0.37 \text{ eV}$. [60]

The effects of transitions between bands separated by *large* energy gaps are not considered in the interband conductivity of Eq. (3.8) or (3.9). The way these large energy gaps are identified depends on the cut-off energy ε_{cut} that is used to separate the band structure of graphene's π electrons into a portion that is described by the Dirac cone, such that $|\varepsilon_{\mathbf{p}}| < \varepsilon_{\text{cut}}$, and another portion that is not. But, the cut-off energy is not precisely defined, and neither are the frequencies of these transitions at large energies. However, if the value of the cut-off energy is chosen such that it is much larger than the Fermi energy in doped graphene, then the resulting expression for the Dirac interband conductivity is independent of the cut-off energy. [109] Under those circumstances, the interband transitions with large energy gaps may be loosely defined as those transitions between valence

and conduction bands that are separated by energies $\varepsilon_{\text{large}} \gtrsim \varepsilon_{\text{cut}}$. Such a contribution to the total interband conductivity in graphene may be obtained, in principle, from full-band *ab initio* calculations by removing the interband transitions within the low-energy portions of the π bands, which are captured by the Dirac cone approximation. Denoting the contribution of the interband transitions with large energy gaps by some function $\sigma_{\text{large}}^{\text{inter}}(\omega)$, the *total interband conductivity* of graphene may be then written in the optical limit as

$$\sigma_{\text{inter}}(\omega) = \sigma_{\text{D}}^{\text{inter}}(\omega) + \sigma_{\text{large}}^{\text{inter}}(\omega). \quad (3.10)$$

Because the exact value of ε_{cut} is not known (although one could estimate it to be on the order of $\varepsilon_{\text{cut}} \sim 1$ eV), little can be said about the exact behaviour of the function $\sigma_{\text{large}}^{\text{inter}}(\omega)$ over a broad range of frequencies.

However, a useful and robust approximation can be deduced for the total interband conductivity of graphene in Eq. (3.10) in the THz-MIR range of frequencies. First, notice that the *real* parts of both $\sigma_{\text{D}}^{\text{inter}}(\omega)$ and $\sigma_{\text{large}}^{\text{inter}}(\omega)$ are negligible over certain finite intervals of frequency adjacent to $\omega = 0$. While this is true in the interval $0 < \omega < 2\omega_{\text{F}}$ for the Dirac interband contribution, as can be seen in Eq. (3.9), the vanishing of $\Re[\sigma_{\text{large}}^{\text{inter}}(\omega)]$ should occur in an even broader interval, say, $0 < \omega < \omega_{\text{large}}$, where $\hbar\omega_{\text{large}} \gtrsim 1$ eV. At the same time, the *imaginary* parts of $\sigma_{\text{D}}^{\text{inter}}(\omega)$ and $\sigma_{\text{large}}^{\text{inter}}(\omega)$ are generally non-zero at low frequencies, but they both vanish when $\omega \rightarrow 0$ as linear functions with negative slopes, as can be surmised from a Kramers-Kronig analysis (see the discussion for phosphorene). For a sufficiently high doping density of graphene, one may use Eq. (3.9) to approximate the Dirac-cone term in Eq. (3.10) as $\sigma_{\text{D}}^{\text{inter}}(\omega) \approx -i\alpha_{\text{D}}\omega$ when $\omega \rightarrow 0$, where $\alpha_{\text{D}} = e^2/(4\pi\varepsilon_{\text{F}})$. While this approximation is valid at frequencies $\omega \ll \omega_{\text{F}}$, the contribution from the interband transitions with large energy gaps also admits a linear approximation, $\sigma_{\text{large}}^{\text{inter}}(\omega) \approx -i\alpha_{\text{large}}\omega$, which should be valid in a broader frequency range. An empirical value of $\alpha_{\text{large}} \approx 1.3$ Å was deduced from *ab initio* calculations in Ref. 102, and was verified by the group of V. Despoja. By comparing the slopes α_{D} and α_{large} , one concludes that the correction due to the interband transitions with large energy gaps becomes relevant at doping densities n exceeding $\sim 5.72 \times 10^{13} \text{ cm}^{-2}$.

3.2.2 Doped phosphorene

In the THz-MIR frequency range, the intraband optical conductivity tensor of doped phosphorene is adequately represented by an *anisotropic Drude model*, [75, 90, 110, 111]

$$\sigma_j^{\text{intra}}(\omega) = \frac{i}{\pi} \frac{D_j}{\omega + i\gamma_j}, \quad (3.11)$$

where the Drude weight, D_j , may be expressed at zero temperature in terms of the equilibrium doping density n and an effective electron or hole mass m_j^* as $D_j = \pi e^2 |n| / m_j^*$ for the direction $j = x, y$. The damping rate $\gamma_j = 1/\tau_j$ in Eq. (3.11) is allowed to depend on the direction as well, and it may be expressed in terms of the mobility tensor of phosphorene having Cartesian components μ_j . By using a relation involving the dc conductivity tensor, $\sigma_j^{\text{intra}}(0) = e|n|\mu_j$, we may write $\tau_j = \mu_j m_j^* / e$ for $j = x, y$.

On the other hand, for a 2D semiconductor with the band gap energy ε_g , the real part of its interband conductivity, $\Re[\sigma_j^{\text{inter}}(\omega)]$, is negligible at frequencies $0 < \omega \lesssim \omega_g$, where $\omega_g = \varepsilon_g/\hbar$. Therefore, because $\varepsilon_g \approx 2$ eV for phosphorene, in order to take into account the interband contribution to its optical conductivity at the THz-MIR frequencies, for which $\omega \ll \omega_g$, it is sufficient to find an approximation for the imaginary part of the interband conductivity, $\Im[\sigma_j^{\text{inter}}(\omega)]$, in the limit $\omega \rightarrow 0$. The *ab initio* data show that, quite generally for a 2D material, [90, 114] $\Im[\sigma_j^{\text{inter}}(\omega)]$ behaves as linear function when $\omega \rightarrow 0$, having a negative slope, say $-\alpha_j$. Accordingly, we can approximate the interband conductivity of doped phosphorene in the THz-MIR frequency range by using

$$\sigma_j^{\text{inter}}(\omega) \approx -i\alpha_j\omega \quad (3.12)$$

for $j = x, y$, where $\alpha_j > 0$ may be regarded as the Cartesian components of its in-plane polarizability tensor in the *static limit*, which arise from high-energy interband electronic transitions. It is expected that the values of α_j are rather independent from the doping density for sufficiently small values of $|n|$, which was confirmed by *ab initio* calculations for phosphorene.

One may determine the numerical values of α_j in two ways by using *ab initio* data for $\sigma_j^{\text{inter}}(\omega)$. First, α_j can be evaluated as the slope of the imaginary part of the interband optical conductivity at vanishing frequency,

$$\alpha_j = -\lim_{\omega \rightarrow 0} \frac{1}{\omega} \Im[\sigma_j^{\text{inter}}(\omega)]. \quad (3.13)$$

An alternate method for determining α_j can be deduced from a Kramers-Kronig relation between the real and imaginary parts of $\sigma_j^{\text{inter}}(\omega)$,

$$\Im[\sigma_j^{\text{inter}}(\omega)] = -\frac{2}{\pi} \omega \mathcal{P} \int_0^\infty \frac{d\omega'}{(\omega')^2 - \omega^2} \Re[\sigma_j^{\text{inter}}(\omega')], \quad (3.14)$$

where \mathcal{P} indicates a Cauchy principal value type of the integral over ω' . Therefore, referring to Eqs. (3.13) and (3.14), α_j may be computed from *ab initio* data for the real part of the

interband optical conductivity as an integral in the form of a sum rule for each direction $j = x, y$,

$$\alpha_j = \frac{2}{\pi} \int_0^{\infty} \frac{d\omega}{\omega^2} \Re [\sigma_j^{\text{inter}}(\omega)]. \quad (3.15)$$

We can observe in Fig. 3.1 that the imaginary part of the interband conductivity of phosphorene, which is obtained using *ab initio* calculations, can be approximated by a linear function of the frequency given in Eq. (3.12) with the slope α_j computed as in Eq. (3.15) for frequencies corresponding to energies smaller than the energy of the band gap in phosphorene.

Finally, using the decomposition of the conductivity in Eq. (3.6) in the expression in Eq. (3.4) gives rise to a decomposition of the optical polarization function as

$$\chi(\mathbf{q}, \omega) = \chi_{\text{intra}}(\mathbf{q}, \omega) + \chi_{\text{inter}}(\mathbf{q}), \quad (3.16)$$

where the intraband component follows from the Drude conductivity in Eq. (3.11) as

$$\chi_{\text{intra}}(\mathbf{q}, \omega) = -\frac{1}{\pi e^2 \omega} \left(\frac{D_x q_x^2}{\omega + i\gamma_x} + \frac{D_y q_y^2}{\omega + i\gamma_y} \right), \quad (3.17)$$

whereas the linear approximation $\sigma_j^{\text{inter}}(\omega) \approx -i\alpha_j \omega$ gives rise to a correction to the optical polarization function due to interband transitions in a form that is independent of frequency,

$$\chi_{\text{inter}}(\mathbf{q}) = \frac{1}{e^2} (\alpha_x q_x^2 + \alpha_y q_y^2). \quad (3.18)$$

Accordingly, the effective 2D dielectric permittivity for a free-standing anisotropic 2D material can be obtained from Eq. (2.38) with $\epsilon_{\text{bg}} = 1$ in the optical limit as

$$\epsilon_{2\text{D}}(\mathbf{q}, \omega) = 1 + \frac{2\pi}{q} (\alpha_x q_x^2 + \alpha_y q_y^2) - \frac{2}{q\omega} \left(\frac{D_x q_x^2}{\omega + i\gamma_x} + \frac{D_y q_y^2}{\omega + i\gamma_y} \right). \quad (3.19)$$

This constitutes what we call the *optical model* of the dynamic polarization of phosphorene, which is expected to work well in the THz-MIR range of frequencies. In the case of doped graphene, the corresponding expression is

$$\epsilon_{2\text{D}}(q, \omega) = 1 + 2\pi\alpha q - \frac{2qv_{\text{B}}\omega_{\text{F}}}{\omega(\omega + i\gamma)}, \quad (3.20)$$

with $\alpha = \frac{e^2}{4\pi\epsilon_{\text{F}}} + \alpha_{\text{large}}$.

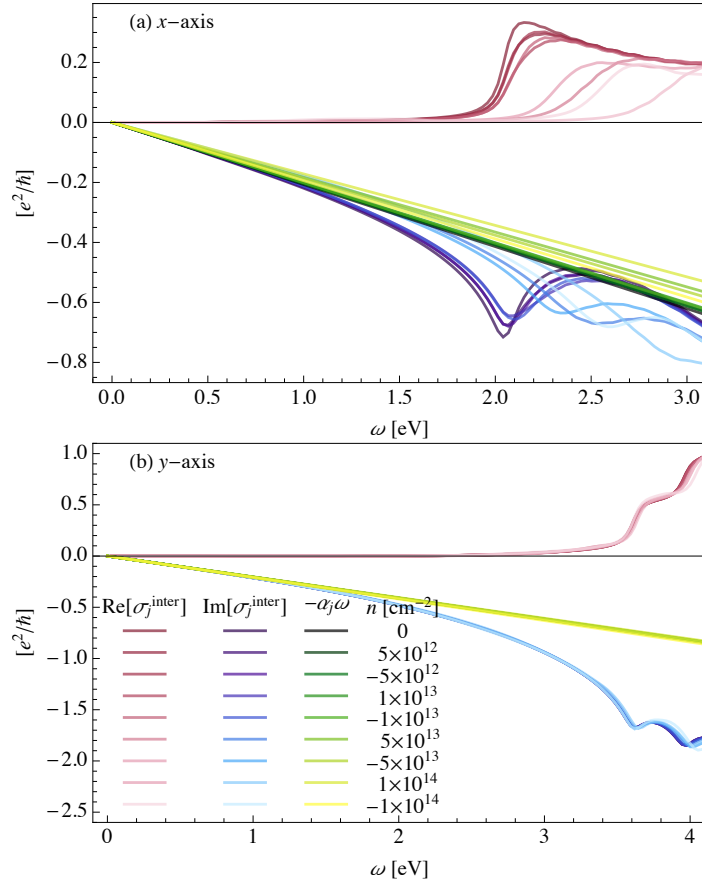


Figure 3.1: Real part (red) and imaginary part (blue) of the interband optical conductivity along the AC (x) and the ZZ (y) axis of phosphorene, with different equilibrium densities, obtained by V. Despoja's group using *ab initio* calculations. The imaginary part is approximated by $-\alpha_j \omega$, with α_j calculated using Eq. (3.15) (green).

3.2.3 Static screening due to interband electron transitions

Notice that, for intrinsic (or undoped) phosphorene and for undoped graphene, the intraband contributions in Eqs. (3.19) and (3.20) are zero, so that the remaining first two terms in the right-hand sides of those expressions describe static screening of the in-plane Coulomb interaction provided by the interband electron transitions, which can also be viewed as the effect of dipolar polarizability of the bound electrons in the host atoms within those two materials.

A similar phenomenological treatment of high-energy interband electronic transitions was recently proposed by Gjerding *et al.* [102] in order to expand the domain of applicability of the Dirac-cone model for the conductivity of doped graphene. The concept of *static screening by interband transitions* was developed in modeling of the binding energy of excitons in isotropic [115] and anisotropic [116] 2D materials. Following the ideas of those authors, we can develop a model for the total polarization function of phosphorene, given in Eq. (3.16), which combines static screening by the interband transitions with a polarization function for the intraband transitions, $\chi_{\text{intra}}(\mathbf{q}, \omega)$, obtained from a suitable model for the dynamics of (quasi-) free charge carriers in doped phosphorene.

To that effect, we can decompose the induced charge density in Eqs. (2.2) and (2.15) as

$$\rho_{2\text{D}}(\mathbf{r}, t) = \rho_{2\text{D}}^{\text{intra}}(\mathbf{r}, t) + \rho_{2\text{D}}^{\text{inter}}(\mathbf{r}, t) \quad (3.21)$$

where the charge density due to the intraband electron excitations may be obtained from a linear relation in the Fourier domain, analogous to Eq. (2.15),

$$\tilde{\rho}_{2\text{D}}^{\text{intra}}(\mathbf{q}, \omega) = -e^2 \chi_{\text{intra}}(\mathbf{q}, \omega) \tilde{\Phi}^0(\mathbf{q}, \omega). \quad (3.22)$$

In a search for suitable model for $\chi_{\text{intra}}(\mathbf{q}, \omega)$, it may be convenient to develop a model for the intraband conductivity tensor in doped phosphorene, $\overleftrightarrow{\sigma}_{\text{intra}}$, in which case we can write, in analogy with Eq. (3.2),

$$\chi_{\text{intra}}(\mathbf{q}, \omega) = \frac{i}{e^2 \omega} \mathbf{q} \cdot \overleftrightarrow{\sigma}_{\text{intra}}(\mathbf{q}, \omega) \cdot \mathbf{q}. \quad (3.23)$$

On the other hand, the induced charge density due to interband electron transitions in Eq. (3.21) may be expressed in terms of a 2D polarization vector field $\mathbf{P}_{2\text{D}}$ as

$$\rho_{2\text{D}}^{\text{inter}}(\mathbf{r}, t) = -\nabla_{\mathbf{r}} \cdot \mathbf{P}_{2\text{D}}(\mathbf{r}, t), \quad (3.24)$$

where $\nabla_{\mathbf{r}}$ is the in-plane gradient. The above relation can be written in the Fourier domain as

$$\tilde{\rho}_{2\text{D}}^{\text{inter}}(\mathbf{q}, \omega) = -i\mathbf{q} \cdot \tilde{\mathbf{P}}_{2\text{D}}(\mathbf{q}, \omega). \quad (3.25)$$

Invoking a constitutive relation with polarization tensor $\overleftarrow{\alpha}(\mathbf{q}, \omega)$ in the form

$$\tilde{\mathbf{P}}_{2\text{D}}(\mathbf{q}, \omega) = \overleftarrow{\alpha}(\mathbf{q}, \omega) \cdot \tilde{\mathbf{E}}_{\parallel}^0(\mathbf{q}, \omega), \quad (3.26)$$

where $\tilde{\mathbf{E}}_{\parallel}^0(\mathbf{q}, \omega) = -i\mathbf{q} \tilde{\Phi}^0(\mathbf{q}, \omega)$ is the in-plane electric field, enables us to finally write

$$\tilde{\rho}_{2\text{D}}^{\text{inter}}(\mathbf{q}, \omega) = -\mathbf{q} \cdot \overleftarrow{\alpha}(\mathbf{q}, \omega) \cdot \mathbf{q} \tilde{\Phi}^0(\mathbf{q}, \omega). \quad (3.27)$$

From this equation and in analogy with Eq. (3.22), we may deduce that the component of the polarization function due to the interband transitions in phosphorene may be expressed in terms of the polarization tensor for its bound electrons as

$$\chi_{\text{inter}}(\mathbf{q}, \omega) = \frac{1}{e^2} \mathbf{q} \cdot \overleftarrow{\alpha}(\mathbf{q}, \omega) \cdot \mathbf{q}. \quad (3.28)$$

The expression in Eq. (3.18) for the interband correction in static regime is obtained by taking the limit $\omega \rightarrow 0$ in the polarization tensor $\overleftarrow{\alpha}$ in Eq. (3.28) and assuming that all its components are independent of \mathbf{q} , i.e., by neglecting the non-local effects in the interband transitions in phosphorene. [116]

A connection can be made with a more traditional view of the intraband and interband electronic transitions, which are often described in the literature on electromagnetic properties of materials as the polarization processes of (*quasi-*) *free* and *bound charge carriers*, respectively. In that respect, the two components in the induced charged density decomposition in Eq. (3.21) can be renamed as $\rho_{2\text{D}}^{\text{intra}}(\mathbf{r}, t) \mapsto \rho_{2\text{D}}^{\text{free}}(\mathbf{r}, t)$ and $\rho_{2\text{D}}^{\text{inter}}(\mathbf{r}, t) \mapsto \rho_{2\text{D}}^{\text{bound}}(\mathbf{r}, t)$, while the components of the polarization function in Eq. (3.16) can be accordingly renamed as $\chi_{\text{intra}}(\mathbf{q}, \omega) \mapsto \chi_{\text{free}}(\mathbf{q}, \omega)$ and $\chi_{\text{inter}}(\mathbf{q}) \mapsto \chi_{\text{bound}}(\mathbf{q}, \omega)$. Also the conductivity tensor can be generally decomposed as

$$\overleftrightarrow{\sigma}(\mathbf{q}, \omega) = \overleftrightarrow{\sigma}_{\text{intra}}(\mathbf{q}, \omega) + \overleftrightarrow{\sigma}_{\text{inter}}(\mathbf{q}, \omega), \quad (3.29)$$

with the components appropriately renamed as $\overleftrightarrow{\sigma}_{\text{intra}} \mapsto \overleftrightarrow{\sigma}_{\text{free}}$ and $\overleftrightarrow{\sigma}_{\text{inter}} \mapsto \overleftrightarrow{\sigma}_{\text{bound}}$, where the resulting relation

$$\overleftrightarrow{\sigma}_{\text{bound}}(\mathbf{q}, \omega) = -i\omega \overleftarrow{\alpha}(\mathbf{q}, \omega) \quad (3.30)$$

ensures that the continuity equation is satisfied by the charge density $\rho_{2\text{D}}^{\text{bound}}(\mathbf{r}, t)$ for the bound charges.

3.3 Semiclassical model

In this subsection, we derive a semiclassical expression for the intraband polarization function $\chi_{\text{intra}}(\mathbf{q}, \omega)$ in doped phosphorene, which includes non-local effects to the leading order, and combine it with the interband correction in Eq. (3.18) to obtain the full polarization function for this material in what we call semiclassical model.

3.3.1 Plasmon dispersion and non-local effects

The simplest expression for the plasmon dispersion relation in free-standing phosphorene, $\omega = \omega_p(q_x, q_y)$, is obtained in a long-wavelength limit by solving the equation $\epsilon_{2\text{D}}(q_x, q_y, \omega) = 0$ for ω with $\epsilon_{2\text{D}}$ given in Eq. (3.19), where we set $\gamma_x = \gamma_y = 0$ and neglect the interband corrections by setting $\alpha_x = \alpha_y = 0$. Then, the resulting anisotropic Drude terms for the intraband transitions in Eq. (3.19) give for doped phosphorene

$$\omega_p^{\text{Drude}}(q_x, q_y) = \sqrt{\frac{2}{q} (D_x q_x^2 + D_y q_y^2)}. \quad (3.31)$$

Similarly, solving the equation $\epsilon_{2\text{D}}(q, \omega) = 0$ with $\epsilon_{2\text{D}}(q, \omega)$ given in Eq. (3.20) where we set $\gamma = 0$ and $\alpha = 0$ gives a plasmon dispersion in the Drude limit for doped graphene as $\omega_p^{\text{Drude}}(q) = \sqrt{2q v_B \omega_F}$. One can see that plasmon frequencies in both materials increase as $\propto \sqrt{q}$ when the wavenumber q increases.

Solving the equation $\epsilon_{2\text{D}}(q_x, q_y, \omega) = 0$ with $\epsilon_{2\text{D}}$ given in Eq. (3.19) where we keep the interband correction with finite α_x and α_y yields plasmon frequency in doped phosphorene in the optical limit as

$$\omega_p^{\text{optical}}(q_x, q_y) = \sqrt{2 \frac{D_x q_x^2 + D_y q_y^2}{q + a_x q_x^2 + a_y q_y^2}}, \quad (3.32)$$

where $a_j = 2\pi\alpha_j$ for $j = x, y$. Similarly, solving the equation $\epsilon_{2\text{D}}(q, \omega) = 0$ with $\epsilon_{2\text{D}}(q, \omega)$ given in Eq. (3.20) in the limit when $\gamma \rightarrow 0$ gives a plasmon dispersion for doped graphene as

$$\omega_p^{\text{optical}}(q) = \sqrt{\frac{2q v_B \omega_F}{1 + aq}}, \quad (3.33)$$

where $a = 2\pi\alpha$. The above two expressions show that our inclusion of the interband correction in the optical model causes plasmon frequencies ω_p in both materials to level off at constant values in the MIR frequency range when the wavenumber q exceeds $\sim 1/\min(a_x, a_y) \approx 0.3 \text{ nm}^{-1}$ for doped phosphorene or $\sim 1/\alpha \gtrsim 0.036 \text{ nm}^{-1}$ for doped

graphene. This fact calls for an estimate of the non-local effects in the dielectric response of those materials in the THz-MIR range. We shall assume that the correction due to the interband electron transitions is still given by the approximation in Eq. (3.18) for phosphorene and by $\chi_{\text{inter}}(q) = \alpha q^2/e^2$ for graphene, and we shall seek improvements to the intraband polarization function χ_{intra} that can describe the so-called continuum of low-energy electron-hole (e-h) excitations. In the case of doped graphene, this continuum can be described by using the Dirac cone approximation to obtain a function $\chi_{\text{intra}}(q, \omega)$ from the quantum mechanical approach, [97, 98] as well as from a semiclassical approach based on the Boltzmann equation. [94] In the following section, we generalize the semiclassical approach of Ref. 94 to the case of an anisotropic 2D material representing doped phosphorene.

3.3.2 Semiclassical model for doped phosphorene

We consider intraband electron transitions within the lowest conduction band of an electron-doped 2D material with an equilibrium doping density of n per unit area, where the low-energy dispersion of the electronic band is approximated by an anisotropic paraboloid, which is given for a Bloch wave with the momentum vector $\mathbf{p} = p_x \hat{\mathbf{x}} + p_y \hat{\mathbf{y}}$ by

$$\varepsilon_{\mathbf{p}} = \frac{p_x^2}{2m_x} + \frac{p_y^2}{2m_y}, \quad (3.34)$$

with m_x and m_y being the effective electron masses in the x and y directions, respectively. It can be shown that the intraband polarization function for such an anisotropic 2D electron gas (2DEG) may be obtained as [102, 117]

$$\chi_{\text{intra}}(q_x, q_y, \omega) = \chi_{\text{iso}}(Q, \omega) \quad (3.35)$$

where $\chi_{\text{iso}}(Q, \omega)$ is the polarization function of an equivalent *isotropic* 2DEG with the same doping density, having the electron mass $m_d = \sqrt{m_x m_y}$ and the wavenumber Q that depends on the wavevector components and the effective electron masses of the anisotropic 2DEG according to

$$Q(q_x, q_y) = \sqrt{q_x^2 \sqrt{\frac{m_y}{m_x}} + q_y^2 \sqrt{\frac{m_x}{m_y}}}. \quad (3.36)$$

An expression for the polarization function of an isotropic 2DEG is obtained in a semiclassical limit from the Boltzmann equation in the *relaxation time approximation*

(RTA) as [94, 106]

$$\chi_{\text{iso}}(Q, \omega) = \chi_s^0 \int_0^\infty d\varepsilon f_0'(\varepsilon) \int_0^{2\pi} d\vartheta \frac{v_\varepsilon Q \cos \vartheta}{\omega + i\gamma - v_\varepsilon Q \cos \vartheta}, \quad (3.37)$$

where $\chi_s^0 = m_d/(\pi\hbar^2)$ is the static polarizability at zero temperature, $f_0(\varepsilon)$ is the Fermi-Dirac distribution, and $v_\varepsilon = \sqrt{2\varepsilon/m_d}$ is the speed of an electron with the energy ε relative to the band bottom. A result for the integration over the angle ϑ in (3.37) is given in Eqs.(24) and (25) of Ref. 94, which can be readily used to obtain $\chi_{\text{intra}}(q_x, q_y, \omega)$ for doped phosphorene at zero temperature. In that limit, the integration over energy ε in (3.37) results in replacing v_ε by the Fermi speed of the equivalent isotropic 2DEG, $v_F^{\text{iso}} = \hbar k_F^{\text{iso}}/m_d$, with $k_F^{\text{iso}} = \sqrt{2\pi n}$ being its Fermi wavenumber. For finite values of the damping parameter γ , one needs to implement Mermin's procedure, [93, 118] giving

$$\chi_{\text{intra}} = \frac{\chi_{\text{iso}}}{1 - \frac{i\gamma}{\omega + i\gamma} \left(1 - \frac{\chi_{\text{iso}}}{\chi_s}\right)}, \quad (3.38)$$

where χ_s is the static polarization function of the equivalent isotropic 2DEG, obtained from (3.37) when both $\omega \rightarrow 0$ and $\gamma \rightarrow 0^+$ at finite temperature. Note that a Mermin-corrected expression (3.38) normally arises when the Bhatnagar-Gross-Krook [119] method is implemented in the process of solving the linearized Boltzmann equation in the RTA. [106]

According to Ref. 94, the intraband polarization function for finite damping is given by

$$\chi_{\text{intra}}(q_x, q_y, \omega) = \frac{q_s}{2\pi e^2} \frac{1 - \chi_r - i\chi_i}{1 - \frac{i\gamma}{\omega + i\gamma} (\chi_r + i\chi_i)} \quad (3.39)$$

where

$$\chi_r(q_x, q_y, \omega) = \frac{|\Omega| \sqrt{A + \sqrt{A^2 + B^2}} + \Gamma \sqrt{-A + \sqrt{A^2 + B^2}}}{\sqrt{2(A^2 + B^2)}}, \quad (3.40)$$

$$\chi_i(q_x, q_y, \omega) = \frac{\text{sign}(\Omega) \Gamma \sqrt{A + \sqrt{A^2 + B^2}} - \Omega \sqrt{-A + \sqrt{A^2 + B^2}}}{\sqrt{2(A^2 + B^2)}}. \quad (3.41)$$

Here, $A = \Omega^2 - \Gamma^2 - 1$ and $B = 2\Omega\Gamma$, where $\Omega(q_x, q_y, \omega) = \omega/(v_F^{\text{iso}}Q)$ and $\Gamma(q_x, q_y) = \gamma/(v_F^{\text{iso}}Q)$ with $Q(q_x, q_y)$ given in Eq. (3.36).

In the limit of zero temperature and for vanishing damping, we finally obtain from

Eqs. (3.35) and (3.37) [94]

$$\Re\{\chi_{\text{intra}}\} = \chi_s^0 \left[1 - |\omega| \frac{H\left(\omega^2 - (v_{\text{F}}^{\text{iso}}Q)^2\right)}{\sqrt{\omega^2 - (v_{\text{F}}^{\text{iso}}Q)^2}} \right], \quad (3.42)$$

$$\Im\{\chi_{\text{intra}}\} = \chi_s^0 \omega \frac{H\left((v_{\text{F}}^{\text{iso}}Q)^2 - \omega^2\right)}{\sqrt{(v_{\text{F}}^{\text{iso}}Q)^2 - \omega^2}}, \quad (3.43)$$

with Q given in Eq. (3.36).

The applicability of the above semiclassical model for χ_{intra} is limited to the range of small wavenumbers, such that $Q \ll k_{\text{F}}^{\text{iso}}$. [106] In the long-wavelength limit, it may be shown that the polarization function in Eq. (3.38) is given to the leading order in $v_{\text{F}}^{\text{iso}}Q/|\omega|$ by

$$\chi_{\text{intra}} \sim -\frac{\chi_s^0}{2} \frac{(v_{\text{F}}^{\text{iso}}Q)^2}{\omega(\omega + i\gamma)}, \quad (3.44)$$

which is, with Eq. (3.36), essentially equivalent to the use of anisotropic Drude model for intraband conductivity in our optical model in Eq. (3.17) with isotropic damping, $\gamma_x = \gamma_y = \gamma$.

In the opposite limit of vanishing frequency (and finite γ), one recovers from Eq. (3.38) $\chi_{\text{intra}} \rightarrow \chi_s^0 \equiv \frac{q_s}{2\pi e^2}$, which is better suited for describing static screening by the intraband transitions in a 2DEG than the Drude model, with $q_s = 2m_d e^2 / \hbar^2$ being the Thomas-Fermi inverse screening length at zero temperature.

3.3.3 Non-local effects in plasmon dispersion

We discuss non-local effects for plasmon dispersion in a free-standing phosphorene doped with $n = 10^{13} \text{ cm}^{-2}$. We use three models of increasing complexity:

- (a) anisotropic *Drude model* for intraband electron transitions,
- (b) full *optical model*, consisting of the anisotropic Drude model plus the interband correction given in Eq. (3.18), and
- (c) *semiclassical model*, consisting of the semiclassical model for the intraband polarization function, plus the same interband contribution given in Eq. (3.18).

The latter model is described by the effective 2D permittivity of free-standing phosphorene, $\epsilon_{\text{bg}} = 1$, given in the limit of vanishing damping and for frequencies $|\omega| > v_{\text{F}}^{\text{iso}}Q$ by

$$\epsilon_{2D}^{\text{semi}}(q_x, q_y, \omega) = 1 + \frac{A}{q} + \frac{q_s}{q} \left[1 - \frac{|\omega|}{\sqrt{\omega^2 - (v_{\text{F}}^{\text{iso}}Q)^2}} \right], \quad (3.45)$$

where Q stands for the function $Q(q_x, q_y)$ given in Eq. (3.36) and A stands for the function

$$A(q_x, q_y) = 2\pi (\alpha_x q_x^2 + \alpha_y q_y^2), \quad (3.46)$$

which describes a contribution from the static polarizabilities due to the interband transitions.

An important nonlocal effect in the semiclassical model is the appearance of a region in the (q_x, q_y, ω) space characterized by a continuum of the intraband electron-hole (e-h) excitations that occur (in the limit of $\gamma \rightarrow 0$) for frequencies $|\omega| < v_{\text{F}}^{\text{iso}}Q(q_x, q_y)$, see Eq. (3.43). This region can have significant effects of the plasmon dispersion curves in free-standing phosphorene, which can only occur at frequencies $\omega > v_{\text{F}}^{\text{iso}}Q(q_x, q_y)$ for small wavenumbers, see Eq. (3.42), and are prevented from crossing the boundary $\omega = v_{\text{F}}^{\text{iso}}Q(q_x, q_y)$ as the wavenumbers increase. This can be seen by solving the equation $\epsilon_{2D}^{\text{semi}}(q_x, q_y, \omega) = 0$ using Eq. (3.45), which yields a plasmon frequency in the semiclassical model as

$$\omega_p^{\text{semi}}(q_x, q_y) = \frac{v_{\text{F}}^{\text{iso}}Q(q_s + q + A)}{\sqrt{(q + A)(2q_s + q + A)}}, \quad (3.47)$$

with Q given in Eq. (3.36) and A given in Eq. (3.46). Notice that the above expressions generalizes the plasmon dispersion given in Eq. (3.32) that was based on the optical model.

In Fig. 3.2, we show the plasmon dispersion curves along the **AC** and the **ZZ** directions for all three models over an extended range of wavenumbers, which exceeds the domain of applicability of the semiclassical model. We see that the interband contribution quickly slows down (already for $q \gtrsim 0.1 \text{ nm}^{-1}$) the rapid increase of the dispersion seen in the Drude model (green curves), but the non-local effects from the semiclassical model (blue curves) prevent the levelling off (already for $q \gtrsim 0.3 \text{ nm}^{-1}$) of the dispersion in the optical model (red curves), making them softly approach the edges of the e-h continuum (orange curves) at large wavenumbers. The V-shaped region above the yellow lines in Fig. 3.2 indicates the range of incident particle speeds exceeding the Bohr's speed, showing that the non-local effects in the forces will likely be negligible compared to the results from the optical model.

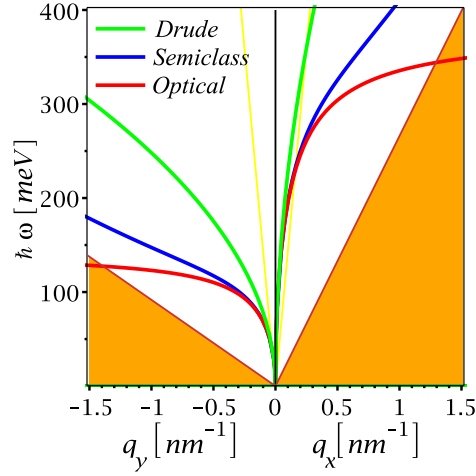


Figure 3.2: Cross sections of the dispersion surface $\omega = \omega_p(q_x, q_y)$ with the planes $q_x = 0$ (left side, $q_y < 0$) and $q_y = 0$ (right side, $q_x > 0$) for plasmon modes in free-standing phosphorene using: the Drude model (green curves), optical model (red curves) and the semiclassical model (blue curves). The two orange shaded regions indicate the continuum of e-h intraband excitations. The yellow lines show the cross sections of the plane $\omega = v(q_x \cos \theta_0 + q_y \sin \theta_0)$ enforcing the kinematic resonance for a particle moving at the speed $v = v_B$ with angles $\theta_0 = 0$ (AC direction) and $\theta_0 = -\pi/2$ (ZZ direction). The numerical values of the parameters used are listed in Chapter 5.

Chapter 4

Relation between image and stopping force via Kramers-Kronig relations using the energy loss function of a supported isotropic 2D material

In particle-based spectroscopy, the stopping force accounts for inelastic interactions in the target material, that is, it is directly related to the [ELF](#) of the target. On the other hand, the image force, which deflects the incident charge towards the target's surface, is a conservative force arising from elastic processes in the dynamic polarization of charge carriers in the target. The signature of the stopping force is a decrease in the velocity of the particle, whereas the image force affects the interaction times with the target [\[8, 13\]](#) and the angular distribution of the scattered particles.[\[14, 33\]](#) Although the image force has been neglected in favor of the stopping force in classic [HREELS](#) applications, [\[11\]](#) herein we show that it can be of interest in the study of plasmon-phonon hybridization for layered nanostructures with 2D materials. [\[12, 34–38\]](#)

The electrodynamic response of the target is calculated as in [Sections 2.1 and 2.2](#), which can be used to model the typical settings for [HREELS](#) [\[7–9, 11, 12\]](#) or ion-surface scattering under grazing incidence, [\[13–18\]](#), so that we are allowed to neglect the perpendicular motion of the particle provided that it may be treated as adiabatically slow on the time scale of the target response.

4.1 Image force in terms of the energy loss function

The stopping force for a charged particle moving on top an isotropic material, Eq. (2.47), can be expressed in terms of the [ELF](#),

$$L(q, \omega) = \Im \left[\frac{-1}{\epsilon_{2D}(q, \omega)} \right]. \quad (4.1)$$

To do so, we use polar coordinates $\mathbf{q} = (q, \theta)$ and $\omega = \mathbf{q} \cdot \mathbf{v} = qv \cos \theta$ to perform a change of variables¹ so that the integration over $\theta \in [0, 2\pi]$ is replaced by an integral over $\omega \in [0, qv]$, resulting in [\[93\]](#)

$$F_s = -\frac{2}{\pi} \frac{(Ze)^2}{v} \int_0^\infty dq e^{-2qz_0} \int_0^{qv} d\omega \frac{\omega}{\sqrt{q^2v^2 - \omega^2}} L(q, \omega), \quad (4.2)$$

where we have used that $L(q, \omega)$ is odd. The stopping force in Eq. (4.2) is a double integral over the region $0 < \omega < qv$ in the first quadrant of the (q, ω) -plane.

The image force in Eq. (2.48) can be expressed in terms of a double integral analogous to Eq. (4.2), [\[93\]](#)

$$F_i = \frac{2}{\pi} (Ze)^2 \int_0^\infty dq q e^{-2qz_0} \int_0^{qv} d\omega \frac{1}{\sqrt{q^2v^2 - \omega^2}} \Re \left[\frac{1}{\epsilon_{2D}(q, \omega)} - 1 \right], \quad (4.3)$$

where we have used that $\Re [1/\epsilon_{2D}(q, \omega) - 1]$ is even. However, it is insightful to express the image force in terms of the [ELF](#) $L(q, \omega)$. This can be done by using the [KK](#) relation for $1/\epsilon_{2D}(q, \omega)$,

$$\Re \left[\frac{1}{\epsilon_{2D}(q, \omega)} - \frac{1}{\epsilon_{2D}(q, \infty)} \right] = \frac{1}{\pi} \mathcal{P} \int_{-\infty}^{\infty} \frac{d\omega'}{\omega' - \omega} \Im \left[\frac{1}{\epsilon_{2D}(q, \omega')} \right], \quad (4.4)$$

where \mathcal{P} indicates a Cauchy principal value integral.

$\epsilon_{2D}(q, \infty)$ in Eq. (4.4) is the dielectric function of the system at “infinite” frequency, which theoretically should be equal to one. [\[120\]](#) However, the dielectric function is modeled with a density response $\chi(q, \omega)$, or conductivity $\sigma(q, \omega)$, valid exclusively for frequencies $0 < \omega < \omega_{\max}$ within the THz-MIR region. Besides that, phenomenological contributions

¹ $dq d\theta = J(q, \omega) dq d\omega$, where the Jacobian is $J(q, \omega) = -1/\sqrt{q^2v^2 - \omega^2}$ for $\theta \in [0, \pi]$ and $J(q, \omega) = 1/\sqrt{q^2v^2 - \omega^2}$, otherwise.

coming from high-energy interband electronic transitions can be considered with a density response $\chi_{\text{high}}(q, \omega)$, which should be valid for frequencies $\omega \geq \omega_{\text{high}}$ with ω_{high} being the onset of these transitions. If $\omega_{\text{max}} \ll \omega_{\text{high}}$, then we can place the infinite-frequency limit of $\chi(q, \omega)$ inside the interval $(\omega_{\text{max}}, \omega_{\text{high}})$ and extend the range of applicability of $\chi(q, \omega)$ by making corrections based on the zero-frequency limit of $\chi_{\text{high}}(q, \omega)$. As a result, $\epsilon_{2\text{D}}(q, \infty) \neq 1$ in general. The treatment is also applicable to the substrate permittivity in the optical regime, $\epsilon_s(\omega)$, and is routinely done for insulators and semiconductors in the gap interval of frequencies, [121] and for polar materials in the range of their optical phonon frequencies. [122] More recently, it was used by Gjerding *et al.* [102] for the Dirac conductivity of graphene, as discussed in Section 3.2.1, Eq. (3.10).

In order to apply the KK relation, the factor $\Re[\dots]$ in Eq. (2.48) is decomposed as

$$\Re \left[\frac{1}{\epsilon_{2\text{D}}(q, \omega)} - 1 \right] = \Re \left[\frac{1}{\epsilon_{2\text{D}}(q, \omega)} - \frac{1}{\epsilon_{2\text{D}}(q, \infty)} \right] + \left[\frac{1}{\epsilon_{2\text{D}}(q, \infty)} - 1 \right], \quad (4.5)$$

where $\epsilon_{2\text{D}}(q, \infty)$ is necessarily real-valued given the symmetry property of $\epsilon_{2\text{D}}(q, \omega)$. [123] Replacing Eq. (4.5) in Eq. (2.48), the image force is given as a sum $F_i = F_{i, KK} + F_{i, \infty}$, where

$$F_{i, KK} = \frac{(Ze)^2}{2\pi^2} \int_0^\infty dq q e^{-2qz_0} \int_{-\infty}^\infty d\omega \Im \left[\frac{1}{\epsilon_{2\text{D}}(q, \omega)} \right] \mathcal{P} \int_0^{2\pi} \frac{d\theta}{\omega - qv \cos \theta}, \quad (4.6)$$

and

$$F_{i, \infty} = (Ze)^2 \int_0^\infty dq q e^{-2qz_0} \left[\frac{1}{\epsilon_{2\text{D}}(q, \infty)} - 1 \right]. \quad (4.7)$$

$F_{i, KK}$ comes from using the KK relation on the first term in Eq. (4.5), and $F_{i, \infty}$ corresponds to the dielectric function at “infinite” frequency. The Cauchy principal value integral in Eq. (4.6) is

$$\mathcal{P} \int_0^{2\pi} \frac{d\theta}{\omega - qv \cos \theta} = 2\pi \frac{\text{sign}(\omega)}{\sqrt{\omega^2 - q^2 v^2}} H(|\omega| - qv), \quad (4.8)$$

where $H(\cdot)$ is the Heaviside unit step function. Thus, the KK term of the image force in Eq. (4.6) becomes

$$F_{i, KK} = -\frac{2}{\pi} (Ze)^2 \int_0^\infty dq q e^{-2qz_0} \int_{qv}^\infty \frac{d\omega}{\sqrt{\omega^2 - q^2 v^2}} L(q, \omega). \quad (4.9)$$

In Eq. (4.9), we have obtained one component of the image force as a function of the **ELF**. The double integral is also restricted to the first quadrant of the (q, ω) -plane, but over the region $\omega > qv$, which complements the region of integration in Eq. (4.2). We note that the component that stems from the **KK** relation, $F_{i, KK}$, may be considered the *dynamic* image force, which vanishes for $v \rightarrow \infty$. On the other hand, $F_i \rightarrow F_{i, \infty}$ for $\omega \rightarrow \infty$. The image force at “infinite” frequency has the form of a force on a static point charge involving $\epsilon_{2D}(q, \omega)$, which is in agreement with the previous discussion on the response functions that account for high-energy electronic transitions with onset frequency ω_{high} . Moreover, we estimate that $F_i = F_{i, \infty}$ when $v \gtrsim z_0 \omega_{\text{high}}$. If $\epsilon_{2D}(q, \infty) = 1$, as if all the high-energy interband transitions are included, then F_i would vanish.

In a classical regime with no recoil, the image force is conservative. However, we are able to express it as a function of the **ELF** which, in theory, should account for all the loss channels in the target material. Some of these loss channels include collective modes, like optical phonons in a polar substrate and a sheet plasmon in doped graphene that hybridize in the THz-MIR range of frequencies. The signature of the hybrid modes are delta-like peaks, and a modal decomposition of the **ELF** can reveal what is the contribution of individual hybrid modes to the image force. This could not be possible without an equation like (4.9) that relates the image force to the **ELF**. We remark that such a modal decomposition might be useful to the design of EELS experiments, given that the hybrid modes will contribute to both forces with different weights, depending on the velocity v and the distance z_0 of the particle, which are parameters that can be externally controlled. Additionally, we can assess models for the response functions $\sigma(q, \omega)$ and $\epsilon_s(q, \omega)$ in the image and stopping force on an equal footing, given that they both are expressed in terms of the **ELF** but with integrals over complementary regions the (q, ω) -plane. Hence, the models can be tested by whether they cover or miss the features happening in the different regions.

4.2 Results for graphene on a silicon carbide substrate

We illustrate the contributions coming from the hybrid modes between the **transverse optical (TO)** phonon in silicon carbide (SiC) and the sheet plasmon in doped graphene.

The dielectric function in the optical limit for the SiC substrate is

$$\epsilon_s(\omega) = \epsilon_\infty + (\epsilon_0 - \epsilon_\infty) \frac{\omega_{\text{TO}}^2}{\omega_{\text{TO}}^2 - \omega(\omega + i\gamma_{\text{TO}})}, \quad (4.10)$$

where $\epsilon_0 = 9.7$ and $\epsilon_\infty = 6.5$ are the static and infinite-frequency dielectric constants. $\omega_{\text{TO}} = 97$ meV is the frequency of a **TO** phonon mode with γ_{TO} being its damping rate.

Setting the gap $h = 0$ between the sheet of graphene and SiC, from Eqs. (2.38), (2.39), (3.4), (3.7) and $\sigma_{\text{inter}}(\omega) \approx -i\alpha\omega$ with $\alpha = \alpha_{\text{D}}$, we obtain the 2D dielectric function of the system as

$$\epsilon_{2\text{D}}(q, \omega) = \frac{\epsilon_s(\omega) + 1}{2} - \frac{2v_B\omega_F q}{\omega(\omega + i\gamma)} + 2\pi\alpha q, \quad (4.11)$$

with $\epsilon_s(\omega)$ given in Eq. (4.10). Taking $\omega \rightarrow \infty$, $\epsilon_{2\text{D}}(q, \infty) = \frac{\epsilon_\infty + 1}{2} + 2\pi\alpha q$, which is used in calculating the image force at “infinite” frequency in Eq. (4.7). This results in

$$F_{i,\infty} = \frac{(Ze)^2}{4z_0^2} \left\{ -1 + \frac{2\zeta}{\epsilon_\infty + 1} [1 - \zeta e^\zeta \text{Ei}(\zeta)] \right\}, \quad (4.12)$$

where $\zeta = z_0 \frac{\epsilon_\infty + 1}{2\pi\alpha}$ and Ei is the exponential integral. In the limit $z_0 \gg \alpha$, the expression in the curly brackets becomes $-(\epsilon_\infty - 1)/(\epsilon_\infty + 1)$, which is the image force on a static point charge a distance z_0 above a substrate with dielectric constant ϵ_∞ .

We can solve $\epsilon_{2\text{D}}(q, \omega) = 0$ analytically by setting γ_{TO} and γ to zero. Thus we find expressions for the eigenfrequencies of the hybrid plasmon-phonon modes, which are

$$\omega_{1,2}(q) = \frac{1}{\sqrt{2X}} \sqrt{Y + Z \mp \sqrt{(Y + Z)^2 - 4\omega_{\text{TO}}^2 XZ}}, \quad (4.13)$$

where $X(q) = \epsilon_\infty + 1 + 4\pi\alpha q$, $Y(q) = \omega_{\text{TO}}^2(\epsilon_0 + 1 + 4\pi\alpha q)$, and $Z(q) = 4v_B\omega_F q$. In Fig. 4.1(a), the dispersion relations $\omega = \omega_1(q)$ and $\omega = \omega_2(q)$ are shown in solid red and blue lines, respectively. The Fermi energy was chosen to be $\epsilon_F = \hbar\omega_F = 0.3$ eV in order to match the experimental data from Ref. 36, which is shown as black dots with error bars. Recalling that we are using $v_B = \frac{e^2}{\hbar}$ and $\alpha = \frac{e^2}{4\pi\epsilon_F}$, we can observe that the lower-frequency mode $\omega_1(q)$ behaves as $\hbar\omega_{\text{sheet}}(q) = \sqrt{4e^2\epsilon_F q/(\epsilon_0 + 1)}$, which is the usual sheet plasmon in graphene (not shown), when $q \rightarrow 0$. As q increases, the lower-frequency mode approaches from below ω_{TO} , the bulk **TO** phonon of the substrate (dashed-dotted green). On the other hand, the higher-frequency mode $\omega_2(q)$ starts at $\omega_{\text{SO}} = \omega_{\text{SO}} \sqrt{(\epsilon_0 + 1)/(\epsilon_\infty + 1)}$, the frequency of the **surface optical (SO)** or Fuchs-Kliwer phonon (dotted green). Finally, as q increases the higher-frequency mode approaches from above $\hbar\omega_{\text{sat}}(q) = \sqrt{4e^2\epsilon_F q/(\epsilon_\infty + 1 + e^2 q/\epsilon_F)}$, the frequency of a sheet plasmon in graphene with saturated dispersion (dashed-dotted blue). The dispersion curves of the hybrid modes when the interband contribution is neglected, $\alpha = 0$, are also shown (dashed lines) in Fig. 4.1(a). We can observe that the experimental

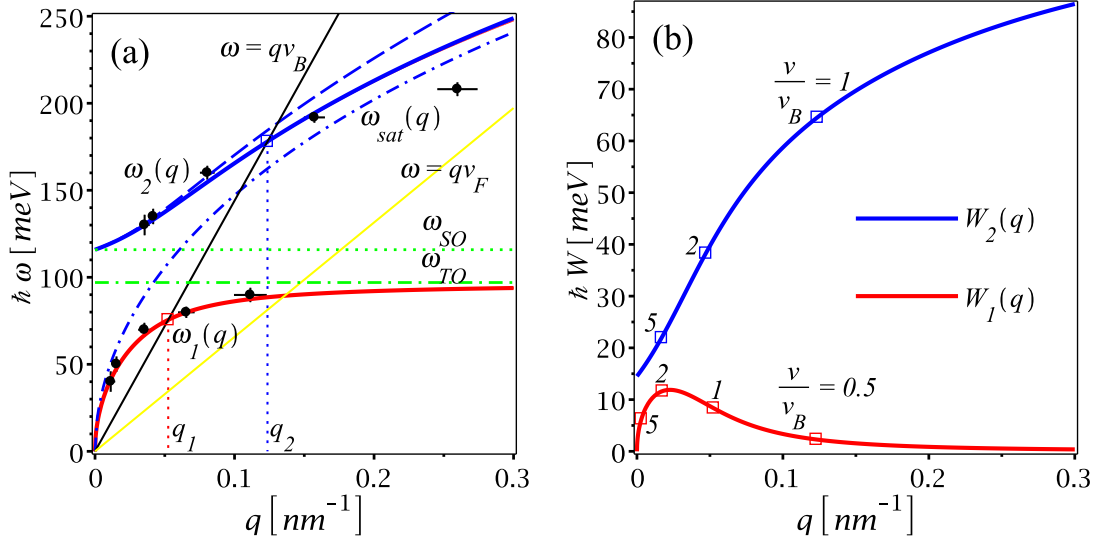


Figure 4.1: (a) Modes $\omega_1(q)$ (red lines) and $\omega_2(q)$ (blue lines) of and (b) the corresponding weight functions $W_1(q)$ and $W_2(q)$ for plasmon-phonon hybridization in a graphene/SiC system. Results are shown for a model of graphene’s conductivity involving intraband and interband electron transitions (solid lines) and for a model neglecting the interband transitions (a, dashed lines). A plasmon dispersion curve is shown for graphene on a substrate with dielectric constant ϵ_∞ (a, dash-dotted blue line). The experimental data points from Ref. 36 are shown as black dots with error bars in panel (a). The other content is described in the text.

data is more closely reproduced by the full optical model for conductivity of graphene, which includes the interband transitions contribution, than the Dirac model [Eq. (3.44)] for the intraband contribution alone. However, we note that the lower-frequency mode $\omega_1(q)$ is not affected when neglecting the interband contribution. In Fig. 4.1(a), the line $\omega = v_F q$ (yellow line) indicates the upper edge of intraband electron-hole excitations continuum in doped graphene, where the collective modes may undergo Landau damping when $\omega < v_F q$. [60]

The kinematic resonance condition $\omega = v_B q$ for an incident charged particle moving with velocity $v_B \approx 2.2v_F$ is shown as a black line that separates the regions that corresponds to the integrals of the image and the stopping force in Eqs. (4.9) and (4.2). The intersection points of $\omega = v_B q$ and the hybrid modes $\omega_{1,2}(q)$ are indicated by squares; and they are at $q_1 \approx 0.052 \text{ nm}^{-1}$ and $q_2 \approx 0.12 \text{ nm}^{-1}$.

The dielectric function is real when the damping parameters are set to zero, that is,

$\epsilon_{2D}(q, \omega) = \Re[\epsilon_{2D}(q, \omega)]$ when $\gamma_{TO}, \gamma \rightarrow 0$. Then, the **ELF** can be expressed as a delta function centered the (q, ω) -points where the real part of the dielectric function become zero. Using the latter, it can be shown that the **ELF** can be written as a modal decomposition [9, 124]

$$L(q, \omega) = \delta(\Re[\epsilon_{2D}(q, \omega)]) = \sum_{j=1}^2 W_j(q) \delta(\omega - \omega_j(q)), \quad (4.14)$$

where the weight functions in the right-hand side of the previous equation are analytically evaluated as

$$W_j(q) = \left\{ \frac{Z(q)}{\omega_j(q)} + \frac{(\epsilon_0 - \epsilon_\infty)\omega_{TO}^2\omega_j(q)}{[\omega_{TO}^2 - \omega_j(q)]^2} \right\}^{-1}. \quad (4.15)$$

The weight functions $W_j(q)$ of the **ELF** are shown in Fig. 4.1(b) and correspond to delta functions centered at the dispersions $\omega = \omega_j(q)$ in Fig. 4.1(a). By inserting the modal decomposition of the **ELF** from Eq. (4.14) in Eqs. (4.2) and (4.9), we can immediately obtain a modal decomposition of the stopping force and the dynamic image force as $F_s = F_{s1} + F_{s2}$ and $F_{i, KK} = F_{i1} + F_{i2}$, respectively. By substituting the delta functions in the double integrals of Eqs. (4.2) and (4.9), these are reduced to a single integral over $q \in (q_j, \infty)$ for the stopping force F_{s_j} and over $q \in (0, q_j)$ for the image force F_{i_j} . In the latter, $q_j(v)$ is the abscissa of the intersection point between the hybrid mode dispersion $\omega = \omega_j(q)$ and the kinematic resonance condition $\omega = qv$, that is, $\omega_j = q_j v$. For example, we show q_1 and q_2 for $v = v_B$ in Fig. 4.1(a). Further, we illustrate in Fig. 4.1(b) the relative contributions from the weight functions to the image and stopping forces by indicating with squares the abscissae of $q_j(v)$ in the plots of $W = W_j(q)$ at $v/v_B = 0.5, 1, 2$ and 5.

The stopping and image force are presented in a reduced form by normalizing them using $F_0 = (Ze)^2/(2z_0)^2$, which is the image force on a static point charge Ze a distance z_0 above a flat conductive surface, or $|\epsilon_s| \rightarrow \infty$. Both forces are negative, but we reverse the sign for convenience.

In Fig. 4.2, the normalized stopping force on the incident charge, $\bar{F}_s = F_s/F_0$, is plotted as a function of its reduced speed, $\bar{v} = v/v_B$, for different distances above graphene, z_0 . In panel (a), the stopping force calculated with the modal decomposition of the **ELF** at vanishing damping, Eq. (4.14), is shown with solid lines. On the other hand, the stopping force with non-zero damping, $\gamma_{TO} = \gamma = 10$ meV, calculated using the 2D dielectric function in Eq.(4.11) with Eq. (4.10) is shown with dotted lines. We can observe that the curves are close to each other, meaning that the we can use the modal decomposition approximation of the **ELF** when the damping in the target materials is small. We also

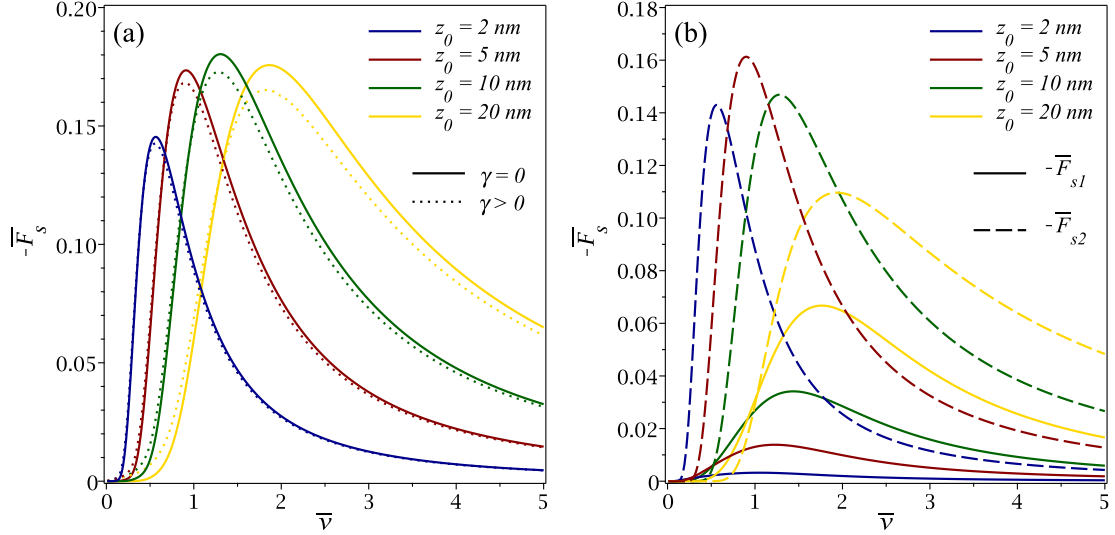


Figure 4.2: (a) The total normalized stopping force, $\bar{F}_s = F_s/F_0$, is evaluated in the limit of zero damping (solid lines) and with finite damping $\gamma_{\text{TO}} = \gamma = 10$ meV (dotted lines) and is shown as a function of the reduced speed $\bar{v} = v/v_B$ for several distances z_0 . (b) The components \bar{F}_{s1} and \bar{F}_{s2} of the total stopping force \bar{F}_s , which come from the modes with frequency $\omega_1(q)$ (solid lines) and $\omega_2(q)$ (dashed lines), are shown as a function of the reduced speed \bar{v} for several distances z_0 .

observe that the stopping force displays a typical behavior [59, 93] with the peak at a speed that increases with z_0 . In panel (b), we compare the components F_{s1} (solid lines) and F_{s2} (dashed lines) of the total stopping force, $F_s = F_{s1} + F_{s2}$. Recall that these are calculated using the modal decomposition of ELF in the zero damping limit and that correspond to the hybrid modes with frequencies ω_1 and ω_2 . We can observe that the stopping force components have maxima at about the same speed. However, the speed of the peak steadily increases with z_0 for F_{s1} , whereas it has a non-monotonous behavior for F_{s2} as z_0 increases. Additionally, we observe that F_{s2} is greater than F_{s1} , except for speeds well below the their peaks. Yet the difference is less pronouce with increasing z_0 at high speeds, where the F_{s1} becomes a larger fraction of F_{s2} .

In Fig. 4.3, we show the image force on a charged particle as a function of its reduced speed, in a manner similar to Fig. 4.2 for the stopping force. In panel (a), the total image force is evaluated using the modal decomposition of the ELF at the limit of zero damping, $\gamma_{\text{TO}}, \gamma \rightarrow 0$, as $F_i = F_{i1} + F_{i2} + F_{i,\infty}$ (solid lines). Meanwhile, the total image force calculated using Eq. (4.6) with non-vanishing damping $\gamma_{\text{TO}} = \gamma = 10$ meV is calculated as

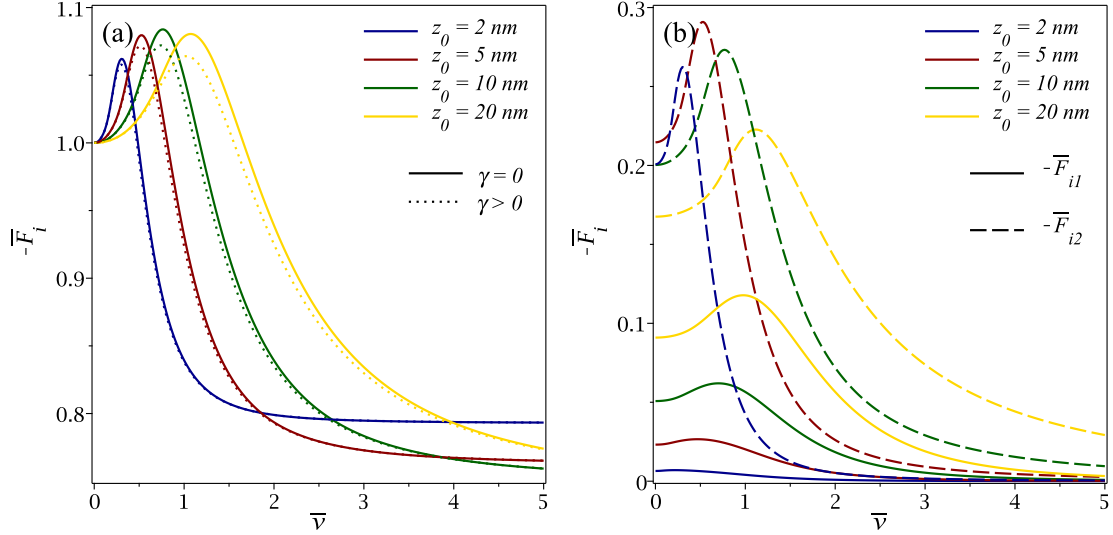


Figure 4.3: (a) The total normalized image force, $\bar{F}_i = F_i/F_0$, is evaluated in the limit of zero damping (solid lines) and with finite damping $\gamma_{\text{TO}} = \gamma = 10$ meV (dotted lines) and is shown as a function of the reduced speed $\bar{v} = v/v_B$ for several distances z_0 . (b) The components \bar{F}_{i1} and \bar{F}_{i2} of the normalized dynamic image force, $\bar{F}_{i,KK}$, which come from the modes with frequency $\omega_1(q)$ (solid lines) and $\omega_2(q)$ (dashed lines), are shown as a function of the reduced speed \bar{v} for several distances z_0 .

$F_i = F_{i,KK} + F_{i,\infty}$ (dotted lines). We observe that the two sets of curves are close and have trends discussed in other works. [59, 93] We also observe that the normalized image force tends to unity, $\bar{F}_i \rightarrow 1$, as the speed of the particle vanishes, $v \rightarrow 0$, which is the the image force on a static charge above an ideal conductor surface with $|\epsilon_s| \rightarrow \infty$. This is explained by the fact that the Drude model for the intraband conductivity yields $\epsilon_{2D}(q, \omega) \rightarrow -\infty$ as $\omega \rightarrow 0$. On the other hand, the image force tends to level off to $F_{i,\infty}$ when the speed is greater than $z_0\omega_{\text{high}}$ by approximately a factor of two, where $\omega_{\text{high}} = 2\omega_F = 0.6$ eV is the onset frequency of interband transitions in graphene corresponding to the Pauli blocking. In panel (b), the components of the dynamic image force, F_{i1} and F_{i2} , are calculated using the modal decomposition of the ELF with vanishing damping. They stem from the hybrid modes $\omega_1(q)$ and $\omega_2(q)$, respectively. Note that $F_{i,KK} = F_{i1} + F_{i2}$, meaning that the image force at infinity frequency $F_{i,\infty}$ has to be added in order to obtain the total image force. We observe that the velocity of the peaks and their height have the same behavior as the components of the stopping force in Fig. 4.2(b). We also observe that the component F_{s2} is dominant for all the speeds, but at high velocities F_{s1} becomes a sizable fraction of F_{s2} .

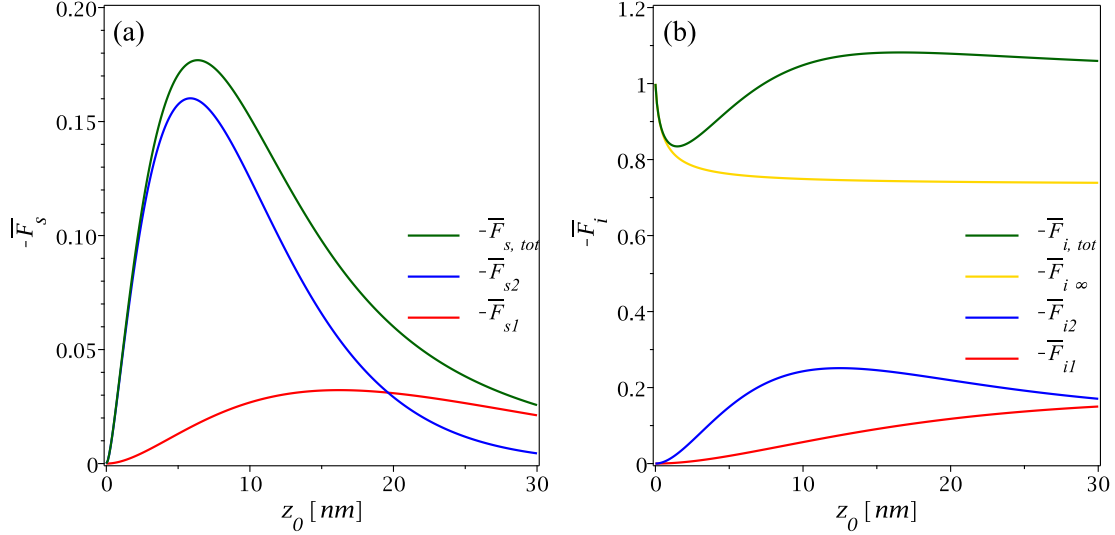


Figure 4.4: (a) The total normalized stopping force, \bar{F}_s , is evaluated in the limit of zero damping and is shown along with its components \bar{F}_{s1} and \bar{F}_{s2} as a function of distance z_0 for the speed $v = v_B$. (b) The total normalized image force, \bar{F}_i , is evaluated in the limit of zero damping and is shown along with its components \bar{F}_{i1} , \bar{F}_{i2} and $\bar{F}_{i,\infty}$ as a function of distance z_0 for the speed $v = v_B$.

Finally, in Fig. 4.4 the stopping and image forces evaluated using the modal decomposition of the ELF in the zero damping limit are shown as functions of the distance from graphene to the incident particle, z_0 , when the velocity of the particle is $v = v_B$. In panel (a), the components of the stopping force F_{s1} and F_{s2} , corresponding to the lower- and higher-frequency hybrid modes $\omega_1(q)$ and $\omega_2(q)$, add up to the total stopping force. Likewise, the components of the dynamic image force F_{i1} and F_{i2} are added to the image force at infinite-frequency from Eq. 4.7, $F_{i,\infty}$, to obtain the total image force in panel (b). We can observe that the peaks of the components F_{s2} and F_{i2} are higher than the peaks of F_{s1} and F_{i1} , respectively. F_{s2} and F_{i2} are dominant for lower speeds, however $F_{s1} = F_{s2}$ for $z_0 \approx 20$ nm, and $F_{i1} = F_{i2}$ for some $z_0 \gtrsim 30$ nm. This can be explained by the fact that for larger values of z_0 , the contributions from smaller q values become dominant in the q -integrals in Eq. (4.2) and Eq. (4.9). Namely, for $z_0 \sim 20 - 30$ nm the contributions are dominant for $q \lesssim 0.03 - 0.05$ nm⁻¹. We can see in Fig. 4.1 that the hybrid modes, and their corresponding weight functions, have closest values in this range, thus yielding force components with similar magnitude.

Chapter 5

Image force and stopping force for an anisotropic 2D material

We use the 2D dielectric functions of doped phosphorene valid for frequencies in the THz-MIR range that were obtained in Chapter 3 using models of increasing complexity. The first one is the anisotropic *Drude model* for intraband electron transitions given Eq. (3.19) with the second term omitted. The second one is the full *optical model* consisting of the anisotropic Drude model plus the interband correction given in Eq. (3.19). The last one is the *semiclassical model*, given in Eq. (3.45), consisting of the spatially dispersive semiclassical intraband polarization function plus the same interband contribution as the optical model.

Note that the first term in Eqs. (3.19) and (3.45) is replaced with $\epsilon_{\text{bg}}(q, \omega)$ to take into account the substrate when needed. Thus, changing the momentum variable from cartesian to polar coordinates, $(q_x, q_y) \rightarrow (q, \theta)$, the dielectric function in Eq. (3.19) for the optical model becomes

$$\epsilon_{2D}(q, \theta, \omega) = \epsilon_{\text{bg}}(q, \omega) + 2\pi q (\alpha_x \cos^2 \theta + \alpha_y \sin^2 \theta) - 2\frac{q}{\omega} D_0 \left(\frac{1}{\bar{m}_x^*} \frac{\cos^2 \theta}{\omega + i\gamma_x} + \frac{1}{\bar{m}_y^*} \frac{\sin^2 \theta}{\omega + i\gamma_y} \right), \quad (5.1)$$

where $D_0 = \pi e^2 |n| / m_0$, whereas $\bar{m}_x^* = m_x^* / m_0$ and $\bar{m}_y^* = m_y^* / m_0$ are the reduced electron or hole effective masses with m_0 being the bare electron mass.

For finite damping, the last term of Eq. (3.45) is replaced accordingly using the density response in Eq. (3.39). Then, the dielectric function for the semiclassical model is

$$\epsilon_{2D}^{\text{semi}}(q_x, q_y, \omega) = \epsilon_{\text{bg}}(q_x, q_y, \omega) + \frac{2\pi}{q} (\alpha_x q_x^2 + \alpha_y q_y^2) + \frac{q_s}{q} \frac{1 - \chi_r - i\chi_i}{1 - \frac{i\gamma}{\omega + i\gamma} (\chi_r + i\chi_i)}, \quad (5.2)$$

with $\chi_r(q_x, q_y, \omega)$ and $\chi_i(q_x, q_y, \omega)$ given in Eq. (3.40) and Eq. (3.41), respectively.

Using the *ab initio* data from Ref. 90 of doped phosphorene with density $n = 10^{13} \text{ cm}^{-2}$ and Fermi energy of 52.2 meV with respect to the lowest-lying conduction band, we adopt the values $\alpha_x = 0.572 \text{ nm}$ and $\alpha_y = 0.488 \text{ nm}$ for static polarizabilities due to interband transitions. Besides that, *ab initio* data for the “effective number of charge carriers”, n_j^e , is used to calculate the reduced effective electron masses as $\bar{m}_x^* = n/n_x^e \approx 0.133$ and $\bar{m}_y^* = n/n_y^e \approx 1.119$. Lastly, the damping rates are calculated with an estimate of the mobility due to electron scattering on charged impurities from Ref. 125, $\mu_x \approx 700 \text{ cm}^2/(\text{V s})$ and $\mu_y \approx 113 \text{ cm}^2/(\text{V s})$, yielding $\hbar\gamma_x \approx 12.4 \text{ meV}$ and $\hbar\gamma_y \approx 9.2 \text{ meV}$, respectively.

For the semiclassical model, we use the same parameters as for the optical model resulting in a Thomas-Fermi inverse screening length of $q_s = 14.58 \text{ nm}^{-1}$ and Fermi speed of $v_F^{\text{iso}} = 7.28 \times 10^{-4}c$, which are obtained using $m_d = 0.20 \text{ MeV}/c^2$. [90] However, the damping rates are chosen to be $\hbar\gamma_x = \hbar\gamma_y = 10 \text{ meV}$ in Eq. 5.2.

On the other hand, we consider a substrate of **silicon dioxide** (SiO_2), whose dielectric function in the THz-MIR range exhibits two **TO** phonon modes with frequencies ω_{TO1} and ω_{TO2} , [59]

$$\epsilon_s(\omega) = \epsilon_\infty + (\epsilon_0 - \epsilon_i) \frac{\omega_{\text{TO1}}^2}{\omega_{\text{TO1}}^2 - \omega(\omega + i\gamma_{\text{TO1}})} + (\epsilon_i - \epsilon_\infty) \frac{\omega_{\text{TO2}}^2}{\omega_{\text{TO2}}^2 - \omega(\omega + i\gamma_{\text{TO2}})}, \quad (5.3)$$

where ϵ_0 , ϵ_i and ϵ_∞ are the static, intermediate and infinite-frequency dielectric constants, and γ_{TO1} and γ_{TO2} the corresponding damping rates.

The parameters used in Eq. (5.3) are: [59] $\epsilon_0 = 3.9$, $\epsilon_i = 3.05$ and $\epsilon_\infty = 2.5$; $\hbar\omega_{\text{TO1}} = 55.6 \text{ meV}$ and $\hbar\omega_{\text{TO2}} = 138.1 \text{ meV}$; $\hbar\gamma_{\text{TO1}} = 5.37 \text{ meV}$ and $\hbar\gamma_{\text{TO2}} = 8.95 \text{ meV}$. From this, we obtain two **SO** or Fuchs-Kliwer phonon modes, $\hbar\omega_{\text{SO1}} \approx 60.9 \text{ meV}$ and $\hbar\omega_{\text{SO2}} \approx 146.5 \text{ meV}$, corresponding to the bulk **TO** modes. Hence, there are two Reststrahlen bands, $\omega_{\text{TO1}} < \omega < \omega_{\text{SO1}}$ and $\omega_{\text{TO2}} < \omega < \omega_{\text{SO2}}$.

Considering it represents the van der Waals distance, the gap between phosphorene and the SiO_2 substrate is $h = 0.4 \text{ nm}$.

As in Chapter 4, the speed of the incident charge is normalized as $\bar{v} = v/v_B$, where $v_B = e^2/\hbar \approx c/137$ is the Bohr velocity.

5.1 Dispersion relations

The dispersion relations of the plasmon mode in free-standing phosphorene, $h \rightarrow \infty$, is found by setting $\epsilon_{2D}(q_x, q_y, \omega) = 0$ in the zero damping limit and were given analytical

expressions in Chapter 3: Eq. (3.31) for the Drude model, Eq. (3.32) for optical model, and Eq. (3.47) for the semiclassical model. We first consider this case to assess the role of the interband contributions in the conductivity models.

5.1.1 Free phosphorene

In Fig. 5.1(a), we show the isofrequency curves $\hbar\omega_p(q_x, q_y) = 50, 100, 150, 200$ and 250 meV of the dispersion relation surface of the plasmon mode in free-standing phosphorene using the Drude model (green curves), optical model (red curves) and semiclassical model (blue curves). We observe that the curves are closed or quasi-elliptical, with the shape of an elongated “8” for the sets of curves of the Drude model and the semiclassical model. Whereas, the curves of 150, 200 and 250 meV are open, or hyperbolic-shaped, for the optical model. Having that $\omega_p(q_x, q_y) = \sqrt{\frac{D_i}{\pi\alpha_i}} = e\sqrt{\frac{n}{m_j^*\alpha_i}}$ when $q_i \rightarrow \infty$ for $i = x, y$, we know that the hyperbolic regime of the dispersion relation of the optical model is in the interval $\omega_{h1} < \omega < \omega_{h2}$, where $\omega_{h1,2} = \min, \max\left(e\sqrt{\frac{n}{m_x^*\alpha_x}}, e\sqrt{\frac{n}{m_y^*\alpha_y}}\right)$. Namely, for free-standing phosphorene the hyperbolic regime is in between $\hbar\omega_{h1} = \hbar e\sqrt{\frac{n}{m_y^*\alpha_y}} \approx 141.4$ meV and $\hbar\omega_{h2} = \hbar e\sqrt{\frac{n}{m_x^*\alpha_x}} \approx 378.6$ meV, which is in the MIR frequency range. Accordingly, in Fig. 3.2 we observe that the cross sections of the dispersion relation surface in the optical model approach ω_{h1} and ω_{h2} from below as $|q_y|$ and $|q_x|$ increases, respectively.

Additionally, we note that the semiclassical model curves are close to the curves of optical model in the MIR range of frequencies, having an quasi-hyperbolic shape even though they are closed. On the other hand, the curves are quasi-elliptic in the THz range for all models. Such range corresponds to wavenumbers much smaller than 1 nm^{-1} . Consequently, we assess that the Drude model should suffice to describe the elliptic behavior of phosphorene, given that the interband correction and non-local effects are negligible in this regime.

In Fig. 5.1(a), we also show the circle $q = 1/(2z_0)$ with $z_0 = 2.5 \text{ nm}$. This circle encloses the relevant region of the (ω, q) -plane to the integrals of the forces in Eqs. (2.44) and (2.45) as indicated by the $\exp(-2qz_0)$ factor. We observe that within this region, the iso-frequency curves of the semiclassical model are close to the curves of the optical model. However, the curves of the Drude model are close to the ones of the other models only for the frequencies near 50 meV. Finally, we note that the isofrequency curves do not cross each other within the set of curves for each model.

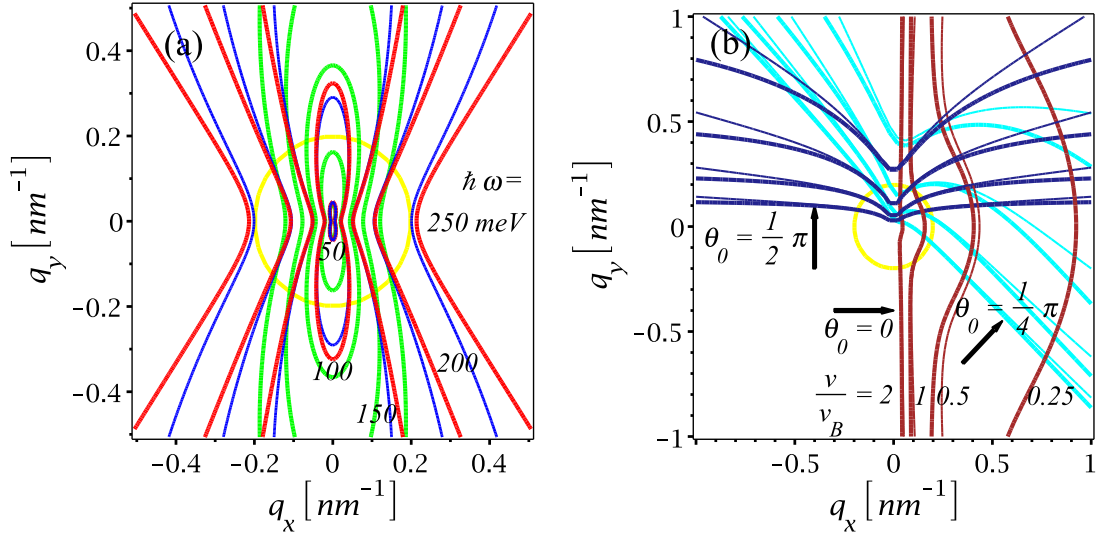


Figure 5.1: (a) Isofrequency curves $\hbar\omega_p(q_x, q_y) = 50, 100, 150, 200$ and 250 meV of the dispersion relation surface for plasmon modes in free-standing phosphorene using: Drude model (green curves), optical model (red curves) and semiclassical model (blue curves). (b) Curves defined by $\omega_p(q_x, q_y) = v(q_x \cos \theta_0 + q_y \sin \theta_0)$ enforcing kinematic resonance for a particle moving above free-standing phosphorene using optical model (thick curves) and semiclassical model (thin curves) for the direction angles: $\theta_0 = 0$ (AC direction, brown curves), $\theta_0 = \pi/4$ (intermediate direction, cyan curves) and $\theta_0 = \pi/2$ (ZZ direction, navy curves), at the reduced speeds $\bar{v} = v/v_B = 0.25, 0.5, 1$ and 2 . (the curves with $\bar{v} = 2$ pass the closest to the coordinate origin for all three directions). Also shown is the circle $q = 1/(2z_0)$ with $z_0 = 2.5$ nm (yellow curve).

We now study the effects of the direction of the velocity of the charged particle moving above free-standing phosphorene in the stopping and image forces. We recognize that the expressions for the longitudinal stopping force in Eq. (2.44) and the transverse stopping force in Eq. (2.45) involve an integral of $\Im [1/\epsilon_{2D}(q_x, q_y, \omega)]$, which is related to the ELF and is strongly peaked at the plasmon frequency $\omega = \omega_p(q_x, q_y)$ when losses are negligible. At the same time, the kinematic resonance condition $\omega = \mathbf{q} \cdot \mathbf{v}$ substitutes the frequency in the dielectric function $\epsilon_{2D}(q_x, q_y, \omega)$ in the integrands of the stopping forces. Then, the main contribution to these two forces comes from $\omega_p(q_x, q_y) = v(q_x \cos \theta_0 + q_y \sin \theta_0)$, where θ_0 is the direction angle of the moving charged particle with respect to the x or AC axis of phosphorene.

The above is the motivation to show in Fig. 5.1(b) the intersection curves of the plasmon dispersion surface of free-standing phosphorene and the kinematic resonance condition plane of the incident charged particle for different reduced speeds $\bar{v} = 0.25, 0.5, 1$ and 2 . We show three sets of curves, each set for a trajectory direction given by $\theta_0 = 0$ (AC direction, brown curves), $\theta_0 = \pi/4$ (an intermediate direction, cyan curves) and $\theta_0 = \pi/2$ (ZZ direction, navy curves). The curves are shown for the optical model (thick lines) and the semiclassical model (thin lines). We observe that the curves with the highest speed passes the closest to the origin of the (q_x, q_y) -plane. The curve for $\bar{v} = 0.25$ and $\theta_0 = 0$ lies outside of the plane shown in Fig. 5.1(b). Also, we note that the curves bend away from the origin for a particle moving along the AC direction ($\theta_0 = 0$), but bend toward the origin for a particle moving along the ZZ direction ($\theta_0 = \pi/2$). Evidently, the parameters that describe the particle's trajectory, θ_0 , v and z_0 , determine the portion, and hence the features, of the plasmon dispersion that contributes the most to the stopping forces. Therefore, we should be able to sample different plasmon dispersion relations, e.g. elliptic or hyperbolic, by tuning the trajectory of the incident particle.

In Fig. 5.1(b), we show the same circle, $q = 1/(2z_0)$ with $z_0 = 2.5$ nm, as in Fig. 5.1(a), which encloses the region of small wavenumbers with dominant contribution in the forces. We again observe that the optical model and semiclassical model yield similar results within this region.

We now regard the effect of the incident particle's trajectory on the image force. The image force in Eq. (2.46) involves a factor of $\Re [1/\epsilon_{2D}(q_x, q_y, \omega) - 1]$ in its integrand. This factor is related to the ELF of the system through a KK transform. As a result, near the plasmon dispersion, that is, when the ELF peaks, the factor in the integrand of the image force changes sign rapidly. Therefore, while the longitudinal and transverse stopping forces are strictly negative because $\Im [1/\epsilon_{2D}(q_x, q_y, \omega)] < 0$, it is not guaranteed that the image force will always be attractive for an anisotropic material. This contrasts with the case of an isotropic material, where the image force is always attractive, as it is shown in

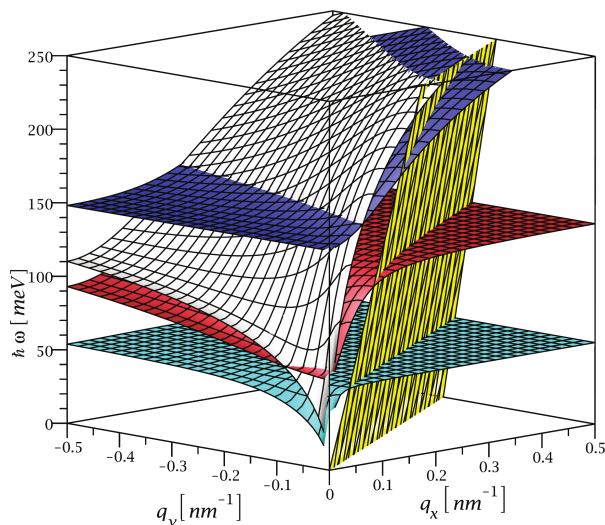


Figure 5.2: Three dispersion surfaces for plasmon-phonon hybrid modes in supported phosphorene, $\omega = \omega_{pk}(q_x, q_y)$, with $k = 1$ for the lowest-lying (cyan), $k = 2$ for the intermediate (red) and $k = 3$ for the highest-lying mode (navy), over the fourth quadrant of the (q_x, q_y) plane, with q_x and q_y oriented along the AC and ZZ directions, respectively. Also shown is a plasmon dispersion surface (gray) for free-standing phosphorene, $h \rightarrow \infty$, as well as the plane $\omega = v(q_x \cos \theta_0 + q_y \sin \theta_0)$ (yellow), which enforces the kinematic resonance condition for a particle moving with the speed $v = 2 \times v_B$ in the direction with angle $\theta_0 = \pi/3$ with respect to the AC direction.

Chapter 4.

5.1.2 Supported phosphorene

Opposed to the case of free-standing phosphorene, that shows a single plasmon mode, the dispersion relation for which the dielectric function vanishes shows three hybridized plasmon-phonon modes for supported phosphorene with SiO_2 . In Fig. 5.2, we show the optical model plasmon-phonon hybrid modes $\omega = \omega_{pk}(q_x, q_y)$, with $k = 1, 2, 3$ for the lowest-lying (cyan), intermediate (red) and highest-lying modes (navy), respectively. Note that a zero gap between the substrate and phosphorene is assumed, or $h = 0$. For comparison, the optical model plasmon mode for free-standing phosphorene (gray) is also shown.

Next, we regard the dispersion relations of the hybrid plasmon-phonon modes of phosphorene and a SiO_2 substrate with a gap distance of $h = 0.4$ nm between the two. In

Fig. 5.3(a), we show the isofrequency curves of the hybrid modes dispersion relation surfaces obtained with the optical model (red curves) and the semiclassical model (blue curves). The curves are given for the same set of frequencies in Fig. 5.1(a). We can observe that the optical model and the semiclassical model yield close isofrequency curves for $q \lesssim 0.2 \text{ nm}^{-1}$, as in Fig. 5.1. We remark that the frequency curve with $\hbar\omega = 50 \text{ meV}$ intersects the lowest-lying mode $\hbar\omega_{p1}$; the frequency curve with $\hbar\omega = 100 \text{ meV}$ intersects the intermediate mode $\hbar\omega_{p2}$; whereas the frequency curves with $\hbar\omega = 100 \text{ meV}$ and above intersect the highest-lying mode $\hbar\omega_{p3}$. This is also shown in Fig. 5.2 and 5.1(b). Additionally, we note that the curves with $\hbar\omega = 50$ and 100 meV intersect the curve with 150 meV for both models, which do not occur in the case of free-standing phosphorene.

In Fig. 5.3(a), we also show the isofrequency curves of the plane $\omega = v(q_x \cos \theta_0 + q_y \sin \theta_0)$ using the same set of frequencies as before. The plane represents the kinematic resonance condition for an incident particle moving with speed $v = v_B$ and direction angle $\theta_0 = \pi/4$. In the figure, the black arrow indicates the direction of increasing frequency. We observe that the intersections of those lines with the optical model curves are close to the intersections with the semiclassical model. Thus, we can confirm that the non-local effects are negligible when compared to the optical model in THz-MIR range for a particle's trajectory with $z_0 \gtrsim 1 \text{ nm}$ and $v \gtrsim v_B$.

In Fig. 5.3(b), we show the cross section of the dispersion relation surfaces with the plane $q_x = 0$ (left side) and the plane $q_y = 0$ (right side) for the optical model (red curves) and the semiclassical model (blue curves). We observe that the three hybrid plasmon-phonon modes, $\omega_{pk}(q_x, q_y)$ with $k = 1, 2, 3$, do not exhibit crossings over the entire (q_x, q_y) plane within each model. The same can be observed in Fig. 5.2. In Fig. 5.3(b), we also show the Reststrahlen bands of the SiO_2 substrate as gray shaded areas. We notice that, in the optical model, the cross section of $\omega_{p1}(q_x, q_y)$ starts at zero and enters the lower-lying Reststrahlen band as both $|q_x|$ and $|q_y|$ increase; the cross section of $\omega_{p2}(q_x, q_y)$ starts at ω_{SO1} , enters the highest-lying Reststrahlen band as $|q_x|$ increases, and increases toward ω_{TO1} with $|q_y|$; whereas the cross section of $\omega_{p3}(q_x, q_y)$ starts at ω_{SO2} , increases with $|q_x|$ but remains almost constant on top of the second Reststrahlen band or ω_{SO1} with increasing $|q_y|$. We see that the dispersion curves of the semiclassical model are indistinguishable from those of the optical model, except on the left side of the intermediate hybrid mode, $\omega_{p2}(q_x, q_y)$, and the right side of the highest-lying hybrid mode, $\omega_{p3}(q_x, q_y)$. These correspond to regions of the (q_x, q_y, ω) -space where the phosphorene plasmon does not hybridized with the SiO_2 phonons. Hence, we can state that the non-local effects of the semiclassical model are negligible when compared to the optical model in regions characterized by a strong plasmon-phonon hybridization.

Additionally, we show in Fig. 5.3(b) the cross sections of the plasmon mode dispersion

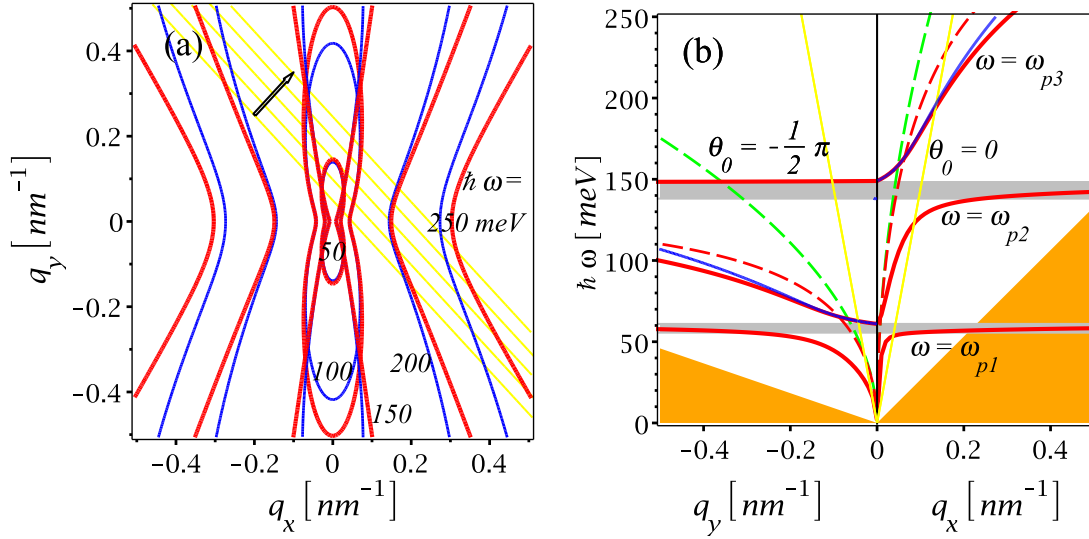


Figure 5.3: (a) Iso-frequency dispersion curves with $\hbar\omega = 50, 100, 150, 200$ and 250 meV for plasmon-phonon modes in phosphorene supported by a SiO₂ substrate using optical model (red curves) and semiclassical model (blue curves), and the corresponding iso-frequency lines for the plane $\omega = v_B(q_x \cos \theta_0 + q_y \sin \theta_0)$ with $\theta_0 = \pi/4$ (yellow lines). (b) Cross sections with the planes $q_x = 0$ (left side, $q_y < 0$) and $q_y = 0$ (right side, $q_x > 0$) are shown for dispersion surfaces of three plasmon-phonon modes, $\omega = \omega_{pk}(q_x, q_y)$ with $k = 1, 2, 3$ in phosphorene supported by SiO₂ using optical model (solid red curves) and semiclassical model (solid blue curves), and for the dispersion $\omega = \omega_p(q_x, q_y)$ in free phosphorene using Drude model (dashed green curves) and optical model (dashed red curves). The two grey shaded regions are the Reststrahlen bands of the SiO₂ substrate, while the two orange shaded areas are the electron-hole intraband continuum in phosphorene. Yellow lines show the cross sections for the plane $\omega = v_B(q_x \cos \theta_0 + q_y \sin \theta_0)$ with $\theta_0 = 0$ and $\theta_0 = -\pi/2$.

surfaces of free-standing phosphorene, obtained with the optical model (dashed red curves) and from the Drude model (dashed green curves). From these curves, we notice that the interband contributions in the optical model become important for wavenumbers $q \sim 0.1 \text{ nm}^{-1}$. Comparing the free-standing phosphorene plasmon mode $\omega_p(q_x, q_y)$ to the hybrid modes of supported phosphorene $\omega_{pk}(q_x, q_y)$ within the optical model, we observe that the intermediate hybrid mode, $k = 2$, approaches the plasmon mode as $|q_y|$ increases, whereas the highest-lying hybrid mode, $k = 3$, approaches the plasmon mode as $|q_x|$ increases. These obviously are regions of the (q_x, q_y, ω) -space characterized by weak plasmon-phonon hybridization.

Finally, we show in Fig. 5.3(b) the cross sections of the plane $\omega = v(q_x \cos \theta_0 + q_y \sin \theta_0)$ (yellow lines), which is the kinematic resonance condition for an incident particle with speed $v = v_B$ and direction $\theta_0 = 0$ (AC) or $\theta_0 = -\pi/2$ (ZZ). The intersection of these lines with the dispersion curves indicate the major contribution from the ELF of the system to the longitudinal stopping force, as indicated in Eq. (2.45). We note that they occur at generally higher plasmon energies when the motion takes place in the AC direction (right side of the figure) than in the ZZ direction (left side of the figure). Hence, by inspection of the location of the intersections, we can predict that the magnitude of the longitudinal stopping force F_ℓ will be larger for a particle moving along the AC axis than for a particle moving along the ZZ axis. This is true for the longitudinal stopping force only, because the transverse stopping force is zero on a particle moving along the AC or ZZ axis.

5.2 Force components

Having seen that the non-local effects of the semiclassical model are negligible for small wavenumber q , it suffices to use the optical model to obtain the force components for large distances z_0 because the predominant contributions stem from dielectric dispersion at small wavenumbers. This motivates us to show the forces, given in Eqs. (2.44)-(2.46), on a particle moving above free-standing and supported phosphorene at the relatively large distance of $z_0 = 50 \text{ nm}$ obtained using the optical model as a function of reduced speed $\bar{v} = v/v_B$ and direction angle θ_0 .

5.2.1 Dependence on speed and direction of motion

In Fig. 5.4(a), we show the longitudinal stopping force, F_ℓ , for free-standing phosphorene. We note that it exhibits a dependence on speed that is typical in isotropic 2D materials, [59,

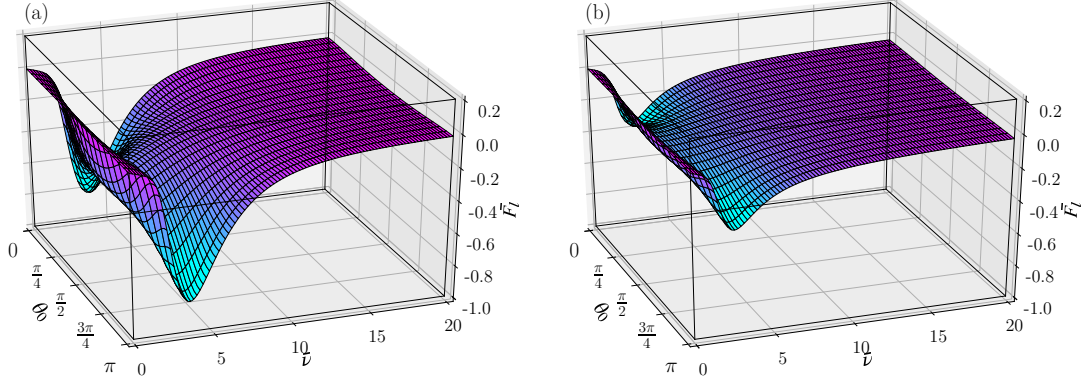


Figure 5.4: Normalized longitudinal stopping force $\overline{F}_\ell = F_\ell/F_0$ as a function of the normalized speed $\bar{v} = v/v_B$ and direction angle θ_0 for a particle moving a distance $z_0 = 50$ nm above: (a) free phosphorene and (b) phosphorene supported by a SiO_2 substrate.

93] as shown in Fig. 4.2 of Chapter 4 for graphene. But, unlike the isotropic case, the longitudinal stopping force exhibits a dependence on the direction of motion θ_0 that is the strongest near the speed $\bar{v} \sim 4$, where it shows a prominent dip. At that velocity, the longitudinal stopping force has the largest magnitude for $\theta_0 = 0, \pi$ (AC direction of phosphorene) and the smallest magnitude for $\theta_0 = \pi/2$ (ZZ direction). The ratio of those two values is about 2.3. The anisotropy in the force for varying direction of motion can be explained by drawing on the experience with other 2D materials, like graphene: it was observed that an increase in the doping density results in a larger stopping force [59, 93]. Therefore, considering that the effective number of charge carriers interacting with the incident charge is higher along the AC axis of phosphorene than the ZZ axis, $n_x^e > n_y^e$, [90] we expect that the longitudinal stopping force on an incident charge moving in the AC direction of phosphorene has a larger magnitude than in the ZZ direction. Recall that the inequality in the effective number of charge carriers is accounted in the model by having an inequality in the effective masses, $\overline{m}_x^* < \overline{m}_y^*$. In Fig. 5.4(b), we observe that the longitudinal stopping force is reduced in the presence of the substrate. However, the anisotropy is still prominent for velocities near the main dip, where the ratio of the magnitude of the force in the AC direction to the ZZ direction is reduced to 1.7. Lastly, we note that the anisotropy effects are diminished for reduced speeds higher than $\bar{v} \sim 10$ in both free-standing and supported phosphorene.

In Fig. 5.5, we show the transverse stopping force, F_t , for free-standing (a) and supported phosphorene (b). This force is generally zero for isotropic materials but shows a

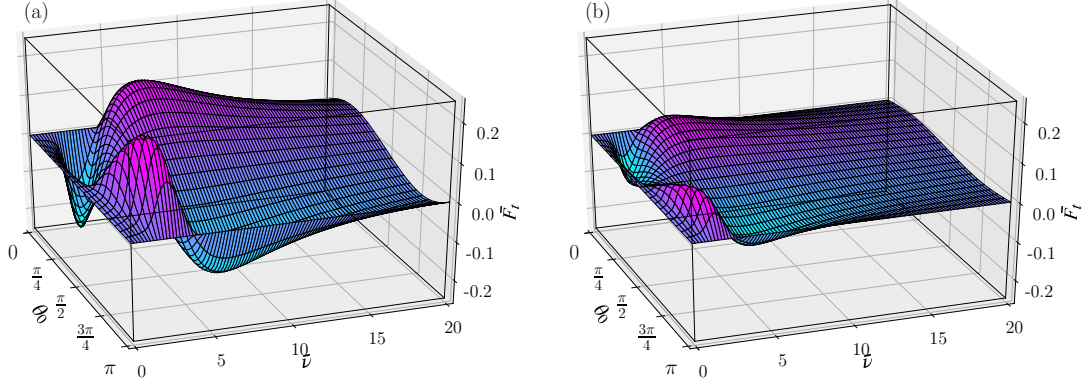


Figure 5.5: Normalized transverse stopping force $\bar{F}_t = F_t/F_0$ as a function of the normalized speed $\bar{v} = v/v_B$ and the direction angle θ_0 for a particle moving a distance $z_0 = 50$ nm above: (a) free phosphorene and (b) phosphorene supported by a SiO_2 substrate.

strong anisotropy for phosphorene, i.e., it varies drastically depending on the direction of motion θ_0 . In fact, F_t is an odd (anti-symmetric) function of θ_0 with respect to the AC direction ($\theta_0 = 0, \pi$) and the ZZ direction ($\theta_0 = \pi/2$). That means the transverse force is zero at the direction of the principal axes of phosphorene and has extrema with opposite sign at intermediate directions. Besides that, the transverse force shows a pair of local extrema at $\bar{v} \sim 2$ and $\bar{v} \sim 7$, which are minimum/maximum points for directions $0 < \theta_0 < \pi/2$ and maximum/minimum points for directions $\pi/2 < \theta_0 < \pi$. As a result, we can claim that the transverse stopping force on a particle moving along an intermediate direction is directed towards the AC axis when $\bar{v} \sim 2$ and towards the ZZ axis when $\bar{v} \sim 7$ because of the sign of F_t at those intervals of θ_0 . In Fig. 2.2(b), the charge is moving with a direction angle in the interval $0 < \theta_0 < \pi/2$ and the green arrow indicates a transverse stopping force with negative sign, which should be the case when $\bar{v} \sim 2$. Next, we note that the magnitude of the transverse force is reduced in the presence of the substrate, as in the longitudinal stopping force. But, unlike the longitudinal force, the effects of anisotropy in F_t persist for high speeds. Finally, we see that the magnitude of the transverse force near the local extrema is comparable to the magnitude of the longitudinal force. Therefore, we can expect that the transverse force should be observable in experiments of HREELS upon rotation of the target with respect to the z axis.

In Fig. 5.6, we show the image force, F_i , for free-standing (a) and supported phosphorene (b). At first glance, the dependence on speed of the image force shows the typical behavior of isotropic 2D materials, [59, 93] as seen in Fig. 4.3 of Chapter 4 for graphene. The image

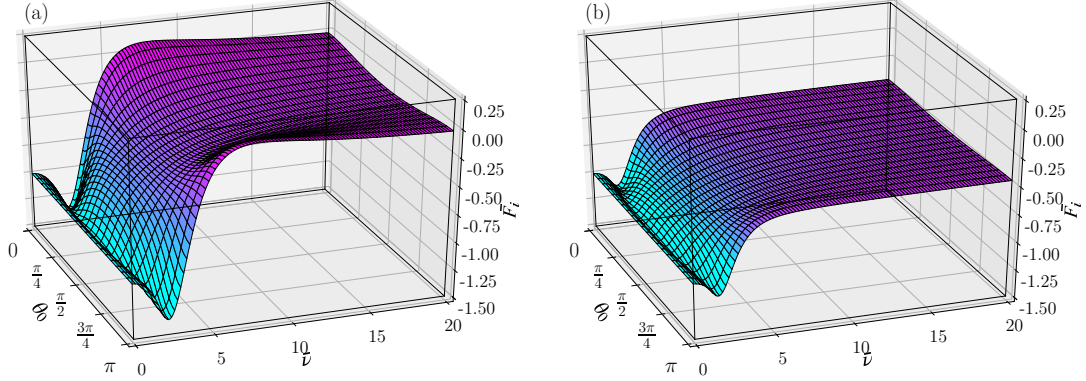


Figure 5.6: Normalized image force $\bar{F}_i = F_i/F_0$ as a function of the normalized speed $\bar{v} = v/v_B$ and the direction angle θ_0 for a particle moving a distance $z_0 = 50$ nm above: (a) free phosphorene and (b) phosphorene supported by a SiO_2 substrate.

force is finite, $F_i = -F_0$, at $v = 0$ due to the contribution of the Drude conductivity; it has a prominent dip around $\bar{v} \sim 2$; and approaches a constant value for $\bar{v} \gg 1$. But, as in the longitudinal stopping force F_ℓ , the image force exhibits large anisotropy, especially for speeds near the dip at $\bar{v} \sim 2$. That is, the magnitude of F_i has the largest value along the AC direction ($\theta_0 = 0, \pi$) and the smallest along the ZZ direction ($\theta_0 = \pi/2$). Namely, the ratio of the magnitude at the AC direction to the ZZ direction is about 1.7 at the dip. As for the longitudinal stopping force, the effects of the anisotropy can be explained by the fact that an incident particle interacts with a higher effective number of charge carriers when it moves along the AC axis of phosphorene than when it moves along the ZZ axis. Finally, we note that the presence of the substrate also reduces the magnitude and attenuates the effects of anisotropy in the image force for velocities near the dip, where the ratio of the of magnitude at the AC direction the ZZ direction becomes only 1.3. We observe that the image force approaches different finite values when $\bar{v} \gg 1$. It tends to zero for free-standing phosphorene in Fig. 5.6(a) but tends to $\sim -0.5 \times F_0$ for phosphorene supported with SiO_2 in Fig. 5.6(b). We can estimate those values using the effective dielectric function in the limit of infinite frequency in Eq. (2.46), as discussed in Chapter 4 for graphene.

The most outstanding feature of the image force in Fig. 5.6 is that it becomes positive for regions near the direction of motion $\theta_0 = 0, \pi$ and speeds in the broad interval $5.7 \lesssim \bar{v} \lesssim 16.5$. In other words, the image force of the optical model becomes repulsive for a particle moving at certain speeds and along the AC direction of phosphorene. On the other hand, F_i levels off at $\sim -0.5 \times F_0$ for speeds $\bar{v} \gtrsim 6$ in the presence of a substrate.

This means that the substrate, besides reducing the magnitude of F_i , prevents the image force from becoming positive. As discussed earlier in this chapter, it is not mathematically guaranteed that the image force is always negative for an anisotropic material. However, this result cannot be physically rationalized given that we have proved that the image force is always negative for an isotropic material by means of a [KK](#) transform in Chapter 4.

5.2.2 Exploring a broader parameter space

In the previous subsection, we restricted ourselves to the study of the forces for a fixed distance and a single model. We now calculate the force components for different fixed speeds, distances, and directions of motion. Our goal is to compare the results for free phosphorene and supported phosphorene, shed light on the feature that originates the positive image force, and evaluate the role of non-local effects. To do so we provide results using the Drude model, optical model, and semiclassical model. Additionally, we introduce a model that describes an hypothetical isotropic 2D material.

In Fig. 5.7, we show cross sections of the surfaces in Figs. 5.4, 5.5, and 5.6 at fixed speeds. The speeds were chosen to represent the regions with accentuated anisotropy in the direction of motion for each force. In Fig. 5.7(a), we show the longitudinal stopping force with $\bar{v} = 4$ and $\bar{v} = 9$ where F_ℓ has a dip and starts to level off, respectively. In Fig. 5.7(b), we show the transverse stopping force with $\bar{v} = 4$ and $\bar{v} = 9$ where F_t shows local extrema. Lastly, in Fig. 5.7(c), we show the image force with $\bar{v} = 2$ and $\bar{v} = 7$ where F_i exhibits a dip and a positive value along near the AC direction, respectively. We confirm that the SiO_2 substrate reduces the magnitude of the forces and attenuates, but does not completely eliminate, the anisotropy in the angular dependence. We observe that the angular dependence changes with velocity. For example, the maximum of the image force is at the ZZ direction and the minimum is at AC direction at the speed $\bar{v} = 2$, but this behavior is reversed at the speed $\bar{v} = 7$ for both free-standing and supported phosphorene. Moreover, the image force reaches positive values at the speed $\bar{v} = 7$ in an interval $|\theta_0| \lesssim \pi/12$ about the AC direction ($\theta_0 = 0, \pi$) for free-standing phosphorene, but it only oscillates around $\sim -0.5 \times F_0$ for supported phosphorene. Finally, we see that the transverse stopping force preserves the anisotropic behavior with the angular dependence in the presence of the substrate, i.e., it is still an odd function with respect to the principal axes of phosphorene.

Next, we investigate the effects of the interband conductivity in the optical model for free phosphorene by comparing the forces obtained with the (anisotropic) Drude model versus the forces obtained with the optical model. Additionally, we assess the effects of

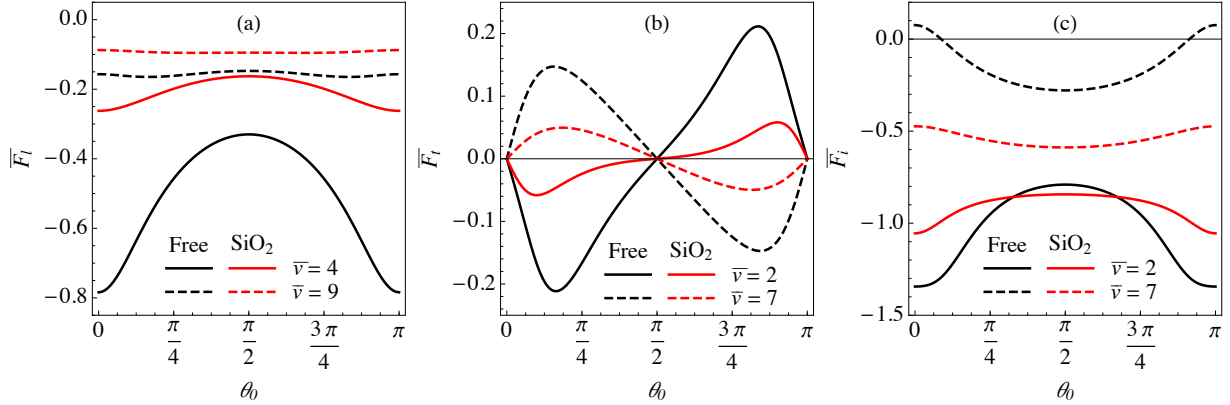


Figure 5.7: Normalized forces vs the direction angle θ_0 for a particle moving a distance $z_0 = 50$ nm above free phosphorene (black curves) and phosphorene supported by a SiO₂ substrate (red curves) at the normalized speeds: $\bar{v} = 4$ (solid lines) and 9 (dashed lines) for the longitudinal stopping force \bar{F}_l (a), and $\bar{v} = 2$ (solid lines) and 7 (dashed lines) for the transverse stopping force \bar{F}_t (b) and the image force \bar{F}_i (c).

the anisotropy in the Drude intraband conductivity by comparing the optical model to the model for the dielectric function of a related but hypothetical *isotropic* 2D material. This isotropic optical model is given by Eq. (5.1), but we set $\alpha_x = \alpha_y = \bar{\alpha}$ with $\bar{\alpha} = \frac{1}{2}(\alpha_x + \alpha_y) \approx 0.53$ nm, $\bar{m}_x^* = \bar{m}_y^* = \bar{m}^*$ with $\bar{m}^* = 2\bar{m}_x^*\bar{m}_y^*/(\bar{m}_x^* + \bar{m}_y^*) \approx 0.238$, and $\mu_x = \mu_y = \bar{\mu}$ with $\bar{\mu} = \frac{1}{2}(\mu_x + \mu_y) \approx 406$ cm²/(V s) so that $\gamma_x = \gamma_y = \bar{\gamma}$ where $\hbar\bar{\gamma} = \frac{\hbar e}{\bar{m}^*\bar{\mu}} \approx 12$ meV, which are obtained from the values of parameters adopted for the (anisotropic) optical model.

In Fig. 5.8, we show the velocity dependence of the image force acting on a particle moving above free phosphorene along the AC axis ($\theta_0 = 0$) at a distance of $z_0 = 10$ nm (a) and $z_0 = 50$ nm (b) calculated using the optical model, the isotropic optical model, and the Drude model. We choose the direction $\theta_0 = 0$ because it is in the interval where the image force becomes repulsive for the optical model, as it can be seen in Figs. 5.6(a) and 5.7(c). Note that the curve for the optical model in panel (b) is a cross section of the surface in Fig. 5.6(a). We observe that the Drude model gives rise to a positive image force for speeds higher than some cutoff v_c , which seems to scale with $\sqrt{z_0}$. Fig. 5.8 reveal that the interband contribution in the optical model lowers the image force back to negative values at speeds $v \gtrsim v_c$ for small distances. However, the lowering weakens with increasing distance z_0 so that there is still a domain of large distances and high speeds with a positive image force.

Similarly, in Fig. 5.9, we show the distance dependence for the three models at different

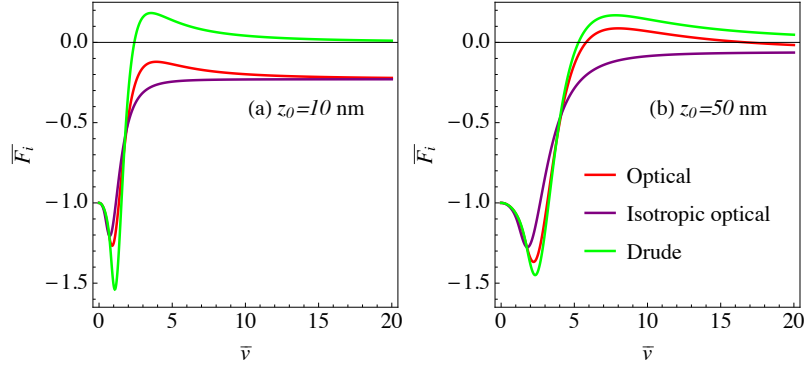


Figure 5.8: Normalized image force \bar{F}_i as a function of reduced speed \bar{v} for a particle moving above free phosphorene at distances $z_0 = 10$ nm and 50 nm with $\theta_0 = 0$.

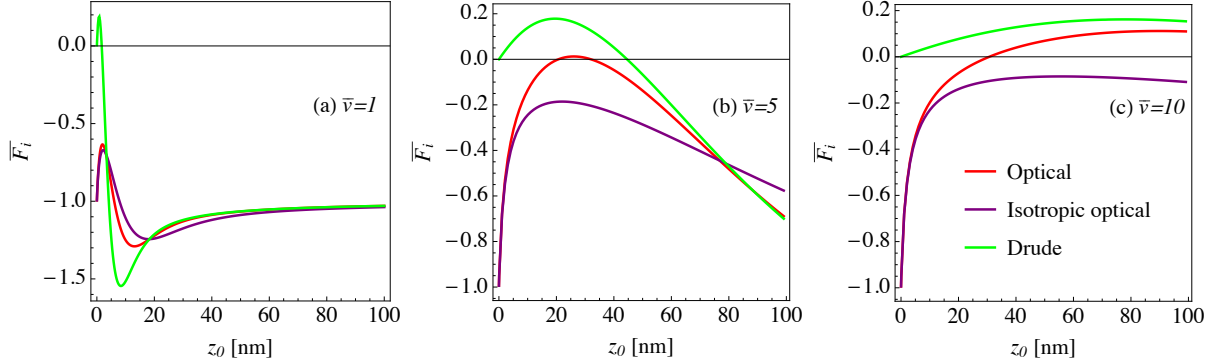


Figure 5.9: Normalized image force $\bar{F}_i = F_i/F_0$ as a function of distance z_0 for a particle moving above free phosphorene with three reduced speeds \bar{v} and with direction $\theta_0 = 0$.

speeds. There we see that the Drude model renders a positive image force in the interval $0 \leq z_0 \leq z_c$, where the upper endpoint, z_c , seems to increase with v^2 . Note that the isotropic optical model never yields a negative F_i . Hence, we confirm that the anisotropic character of the intraband Drude conductivity in the optical model is responsible for raising a positive image force. Contrarily, the interband transitions contribution tends to reduce the image force or bring it to a range of negative values.

In Fig. 5.10 and Fig. 5.11, we show the velocity dependence of the longitudinal stopping force and the transverse stopping force, respectively, calculated using the optical model, the isotropic optical model, and the Drude model. The longitudinal force was calculated for a particle moving above free phosphorene along the AC axis, whereas the transverse force was calculated at the intermediate direction $\theta_0 = \pi/4$. Recall that the stopping force

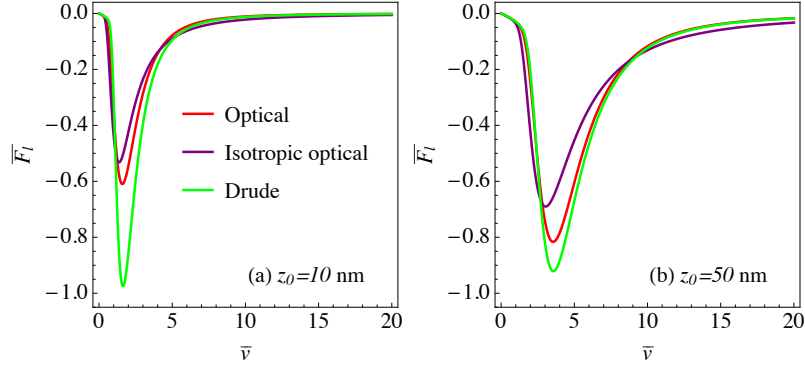


Figure 5.10: Normalized longitudinal stopping force \overline{F}_ℓ as a function of reduced speed \overline{v} for a particle moving above free phosphorene at distances $z_0 = 10$ nm and 50 nm and with direction $\theta_0 = 0$.

is zero for directions $\theta_0 = 0, \pi$ or $\theta_0 = \pi/2$ and vanishes for an isotropic 2D material. The forces do not change sign and maintain the same qualitative behavior among the models. However, the (isotropic) Drude model makes the image force increase in magnitude at its local extrema.

To further explore the role of anisotropy of the Drude intraband conductivity in a repulsive image force, in Fig. 5.12 we show F_i for particle moving above free phosphorene in the AC direction using a modified Drude model of the dielectric function. The product of the reduced effective electron masses, obtained from the *ab initio* data, is kept fixed $\overline{m}_x^* \overline{m}_y^* = 0.149$; meanwhile, the ratio of the masses $R = \overline{m}_x^* / \overline{m}_y^*$ is varied. In the figure we show the image force calculated using the modified Drude model with a mass ratio ranging from $R = 0.1$, describing a very anisotropic material, to $R = 1$, the isotropic case, as a function of distance with speed $\overline{v} = 5$ (a) and as a function of speed for the distance $z_0 = 20$ nm. We observe that the image force becomes positive even for deviations from the isotropic case. The ranges of repulsive F_i , $z_0 < z_c$ for fixed speed and $\overline{v} > \overline{v}_c$ for fixed distance, depend on the ratio of the masses R in a non-monotonous manner.

Figs. 5.8, 5.9 and 5.12 have revealed that the anisotropic nature of the intraband Drude conductivity gives rise to positive values of the image force. However, the interband transitions contribution in the optical model counteracts this effect. In fact, for lower speeds and smaller distances, the optical model can yield an image force that is only negative-valued. Therefore, and taking into account the fact that the integrand of the image force in Eq. (2.46) depends on the dielectric function at high frequencies, we speculate that including the contribution of a full description of interband transitions, we can ensure that

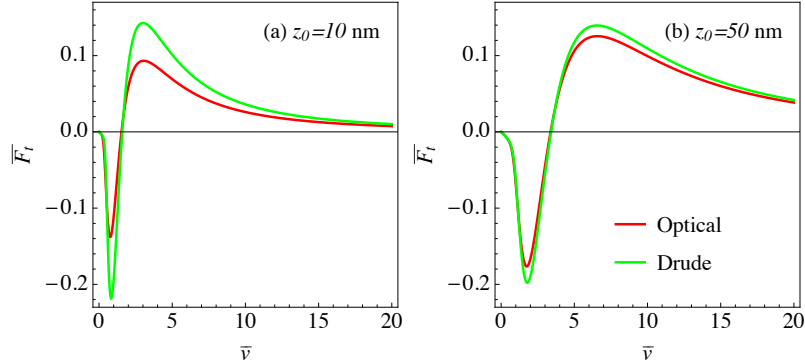


Figure 5.11: Normalized transverse stopping force \overline{F}_t as a function of reduced speed \overline{v} for a particle moving above free phosphorene at distances $z_0 = 10$ and 50 nm and with direction $\theta_0 = \pi/4$.

F_i will be negative in the complete range of the particle's trajectory parameters, θ_0 , v and z_0 .

Next, we illustrate the case of particle moving above free phosphorene at a relatively short distance, $z_0 = 5$ nm, and with low speeds, $v < v_B$, in order to shed light on the role of non-local effects of the semiclassical model. Recall that the predominant contributions to the integrals in Eq. (2.44)-(2.46) are given for wavenumbers $q \lesssim 1/(z_0)$. Then, the larger the distance z_0 , the smaller the contribution of non-local effects is. In Fig. 5.13, we show the image force and the longitudinal stopping force as function of the reduced speed for particle moving with direction $\theta_0 = 0$ (AC) and $\theta_0 = \pi/2$ (ZZ) using the Drude, optical, and semiclassical models. Additionally, in Fig. 5.14 we show the transverse stopping force as a function of the direction of motion for three different speeds using the same three models. The figures show a qualitative agreement of the semiclassical model with the optical model. Moreover, the quantitative difference is small to negligible. On the other hand, the Drude mode differs both quantitatively and qualitatively from the other two models. This suggests that the interband contribution in both the optical and classical models is important in the regime of low speeds and small distances.

Finally, we show in Fig. 5.15 the same cross sections in Fig. 5.7 comparing the forces obtained with the optical model (solid lines) and the semiclassical model (dashed lines). We observe again that the non-local effects have a negligible role even for the forces acting on a particle that moves at a relatively large distance of $z_0 = 50$ nm, since there is only a small quantitative difference between the two models. This result can also be confirmed by the calculating the forces as in Figs. 5.4-5.6 using the semiclassical model, which will

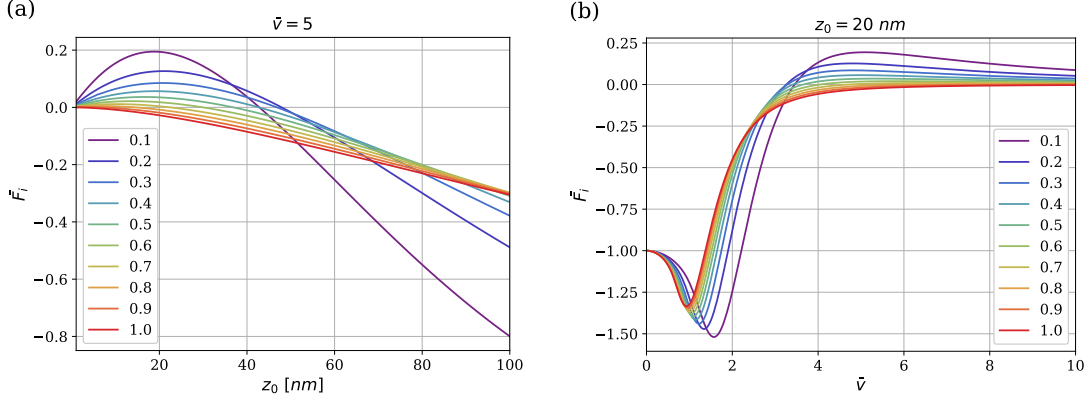


Figure 5.12: Normalized image force $\bar{F}_i = F_i/F_0$ as a function of: (a) the distance z_0 (in nm) for fixed normalized speed $\bar{v} = v/v_B = 5$, and (b) the normalized speed \bar{v} for fixed distance $z_0 = 20 \text{ nm}$. Results are shown for a Drude model of doped phosphorene with $n = 10^{13} \text{ cm}^{-2}$ where the product of the reduced electron masses is kept fixed at $\bar{m}_x^* \bar{m}_y^* = 0.149$, while their ratio $R = \bar{m}_x^*/\bar{m}_y^*$ is varied in an interval from $R = 0.1$ to $R = 1$ in steps of 0.1.

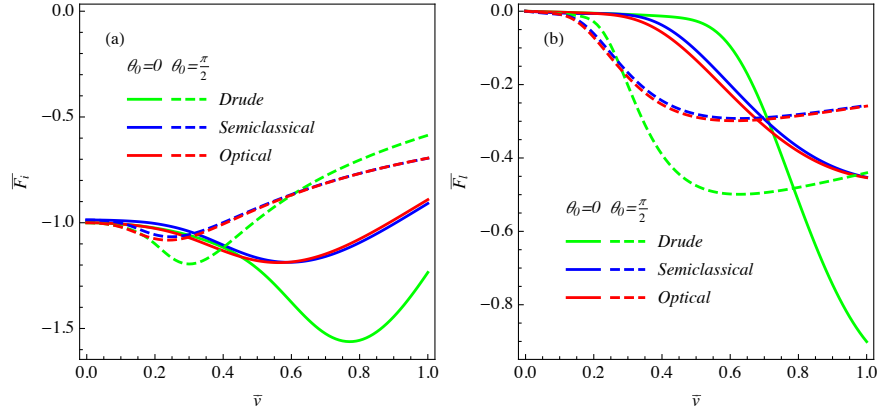


Figure 5.13: (a) Normalized image force $\bar{F}_i = F_i/F_0$ and (b) normalized longitudinal stopping force $\bar{F}_l = F_l/F_0$ vs normalized speed $\bar{v} = v/v_B$ with distance $z_0 = 5 \text{ nm}$ and the direction angles $\theta_0 = 0$ (solid lines) and $\theta_0 = \pi/2$ (dashed lines), obtained for free-standing phosphorene using: Drude model (green curves), optical model (red curves) and the semiclassical model (blue curves).

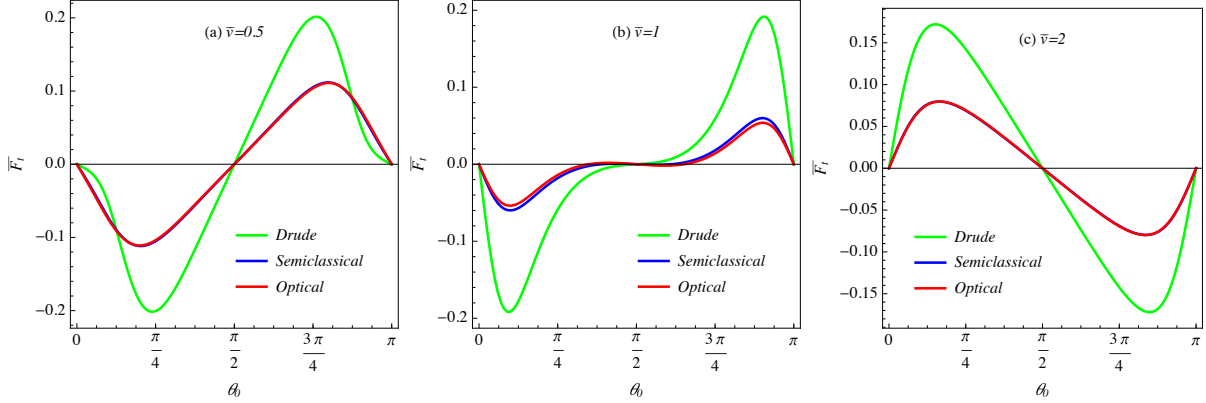


Figure 5.14: Normalized transverse stopping force $\bar{F}_t = F_t/F_0$ vs incidence angle θ_0 for three normalized speeds: (a) $\bar{v} = 0.5$, (b) 1 and (c) 2, with distance $z_0 = 5$ nm, obtained for free-standing phosphorene using: Drude model (green curves), optical model (red curves) and the semiclassical model (blue curves).

not show qualitative differences from the optical model.

To summarize, we remark some of the key findings of this section dedicated to explore the behavior of the forces acting on a particle moving above phosphorene. First, the anisotropic character of the intraband conductivity gives rise to a repulsive force for a direction of motion near the AC axis of phosphorene, which is a physically implausible result. However, the effect of the anisotropic intraband conductivity is counteracted by the interband transitions conductivity at relatively low speeds and small distances. Thus, we expect that considering a full interband description of the anisotropic material will prevent the image force from becoming repulsive for the whole range of parameters of the particle's trajectory. Additionally, the non-local effects of the intraband conductivity introduced in the semiclassical model were negligible in comparison to the optical model. Finally, we emphasize that the magnitude of the transverse stopping force is comparable to that of the longitudinal stopping force. Moreover, it shows an accentuated dependence on the angle of motion. We can then expect that transverse stopping force should be measurable in experiments of HREELS with anisotropic materials like phosphorene.

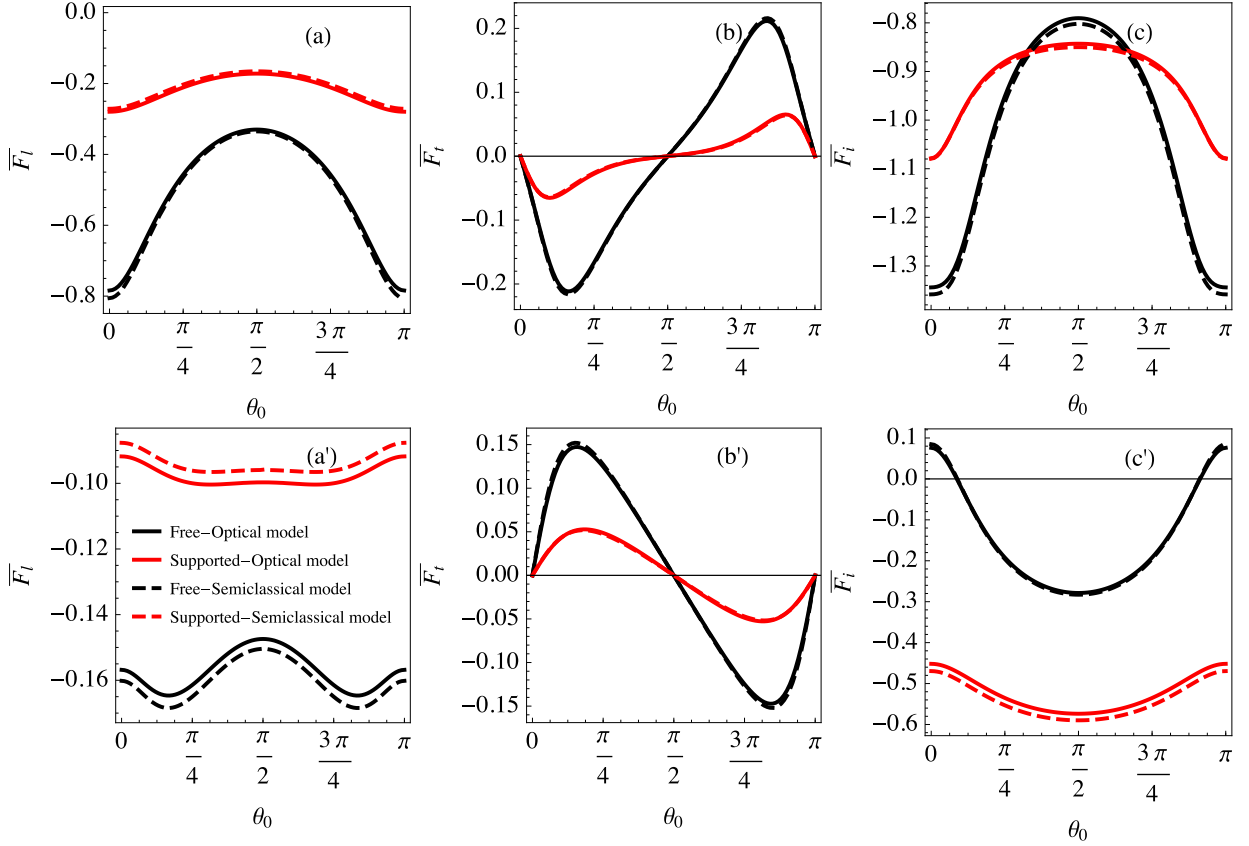


Figure 5.15: Normalized forces vs the direction angle θ_0 for a particle moving a distance $z_0 = 50$ nm above free phosphorene (black curves) and phosphorene supported by a SiO_2 substrate (red curves), using the optical model (solid curves) and the semiclassical model (dashed curves). Panels (a) and (a') show the longitudinal stopping force \bar{F}_l for the normalized speeds $\bar{v} = 4$ and 9, respectively, panels (b) and (b') show the transverse stopping force \bar{F}_t for the speeds $\bar{v} = 2$ and 7, respectively, and panels (c) and (c') show the image force \bar{F}_i for the speeds $\bar{v} = 2$ and 7, respectively.

Chapter 6

Conclusions

In Chapter 2, we have solved a time-dependent Poisson equation for the total electric potential in the presence of a classical charged particle that moves with constant velocity parallel to the flat surface of a layered structure with large area. The problem was further simplified by taking advantage of the temporal invariance and the translational invariance in the directions parallel to the surface of the structure, allowing us to perform a 1+2 dimensional Fourier transform, which converted the Poisson equation into a second-order ordinary differential equation. That equation was solved in a piece-wise manner as a function of the coordinate perpendicular to the surface, while taking into account the standard electrostatic boundary and matching conditions at sharp boundaries between regions in the structure that are occupied by different materials.

We assumed that the structure consists of a 2D material and a semi-infinite region filled with a solid material, with a gap between them that reflects the van der Waals nature of their interaction. By adopting the linear response formalism, we assumed that a polarization function, or an in-plane conductivity is available for the dynamic response electrons in the 2D material, and that the electric polarization of the substrate may be described by a dielectric function with temporal and possibly spatial dispersion. The main result of solving the Poisson equation in Chapter 2 was a formulation of the expressions for the stopping and image forces that act on the charged particle, which contain the in-plane conductivity of the 2D material and the dielectric function of the substrate as input functions.

In Chapter 3, we have described several analytical models for the response function that describes the dynamic polarization of electrons in a 2D material. We have primarily focused on models valid in a low-frequency regime, from the THz to the MIR, which is of

a substantial current interest in literature. The parameters in our models were calibrated against the data available from *ab initio* calculations of the response functions. We have specifically developed models suitable for an isotropic 2D material, represented by doped graphene, and an anisotropic material, represented by doped phosphorene. Two novel aspects were discussed in such models: a phenomenological treatment of the high-energy interband electronic transitions based on the [KK](#) analysis for both materials, and the non-local effects in the spatial dispersion based on a Boltzmann equation for intraband electron transitions in phosphorene.

In Chapter 4, we have used the definitions of stopping and image force on a point charge moving parallel to a 2D material, supported by an isotropic substrate, as derived in Section 2.3 with the effective dielectric response formulated in Section 2.2. Then, using a [KK](#) relation between the imaginary and real part of the [ELF](#) and provided that the 2D material is also isotropic, we have obtained an analytical expression of the image force in terms of the [ELF](#). This yields definitions of the forces as integrals of the [ELF](#) over complementary regions of the frequency and momentum space, separated by the kinematic resonance condition between the incident point charge and the target system. This result is relevant for the following reasons. First, the image force, which is classically conservative, can be analysed in particle-based spectroscopy because it is a function of the [ELF](#), in a similar way the stopping force is a function the [ELF](#). Second, models for the dielectric response of the target system can be compared on an equal footing for the stopping and image force based on whether they cover or miss the features of the [ELF](#), which shape the forces, in complementary regions of the frequency and momentum space.

We have illustrated the case of doped graphene supported by a SiC substrate for frequencies in the THz-MIR range. For that, we have employed models that describe the [TO](#) phonon in the substrate and the sheet plasmon in graphene. Specifically, we have used models in the optical limit of the dielectric function of the substrate and the conductivity of graphene, equipped with corrections coming from high-energy interband electronic transitions as discussed in Section 3.2.1. The resulting formulation of the dielectric response is simple enough that allows us to perform, in the limit of zero damping, a modal decomposition of the [ELF](#) with analytical expressions for the plasmon-phonon hybrid modes and their weight functions. Thus, we can study the components of the stopping and image force arising from the hybrid modes of the target system as functions of the velocity and the distance from the target of the incident particle. This result is promising because it allows us to approximate the components of the stopping and image force for target materials in which the collective modes are well-defined and long-lived. Moreover, it helps us to understand how the relative weight of plasmon-phonon hybrid modes affect the outcome of grazing-angle [EELS](#) of heterostructures involving 2D materials.

In the first section of Chapter 5, we used two analytical models to describe the conductivity associated to intraband electronic transitions in phosphorene, for the THz-MIR range of frequencies. These models were the Drude conductivity from Section 3.2.2 and the semiclassical intraband polarization from Section 3.3.2. Both had an anisotropic character, and their parameters were based in *ab initio* calculations. However, the Drude conductivity was valid in the optical limit, whereas the semiclassical model partially accounted for non-local effects. The novelty of this work was to include a correction in the total conductivity from high-energy interband electronic transitions in the static limit. The corrected total conductivity enabled us to find a transition in the isofrequency dispersion relations of the plasmon mode, from elliptical behavior in the THz regime to hyperbolic behavior in the MIR regime. The above description of the conductivity was used in free-standing phosphorene as well as in phosphorene supported by a SiO_2 substrate. In the later case, the conductivity of the two-dimensional material was coupled to the substrate's permittivity with two phonons in the optical limit. Consequently, we found three plasmon-phonon hybrid modes separated by the two Reststrahlen bands of SiO_2 and observed that they preserve the transition from elliptic to hyperbolic shape in the isofrequency dispersion relations as seen in free phosphorene. However, we noted that these isofrequency curves intersected themselves in the plane of the wavevector components, unlike free phosphorene.

In the second section of Chapter 5, by using the aforementioned models for the effective dielectric function, we calculated the electrodynamic forces acting on a particle moving with a classical trajectory at a fixed distance of $z_0 = 50$ nm and speeds relevant to experiments of HREELS with oblique incidence or the grazing scattering of ions. We observed that both quantitative and qualitative effects arose from the anisotropy of phosphorene. Namely, all forces had different behavior depending on the speed and direction of motion. This result is relevant since previous work have demonstrated that HREELS experiments under grazing angles are sensitive to the anisotropy of the target's surface. Another effect of the anisotropy of phosphorene was the emergence of the transverse stopping force, which is dissipative and parallel to the target's surface but perpendicular to the trajectory of the incident particle. This force was found to have a strong magnitude, comparable to that of the more typical longitudinal stopping force. Additionally, it also showed to change its character as the speed and direction of motion are varied. For example, the transverse force acting on a particle, that moves along an intermediate direction above phosphorene, will deflect the particle towards the AC direction when the reduced speed, $\bar{v} = v/v_B$ with v_B being the Bohr speed, is $\bar{v} \sim 2$, but reverse its sign and deflect the particle towards the ZZ direction when the reduced speed is $\bar{v} \sim 7$. Finally, the image force, which is conservative and normally attractive, also underwent the effects of phosphorene's anisotropy: its magnitude changed as a function of the speed and direction of motion.

Furthermore, the image force became repulsive for a direction of motion close to the AC axis with speeds in the interval $6 \lesssim \bar{v} \lesssim 16$. This striking and physically implausible result was traced back to the anisotropy of the models for the intraband conductivity of phosphorene at high frequencies, being an important issue for future research. Nevertheless, the flaw was partially avoided by the interband transitions correction of the total conductivity in the static limit. This finding motivate us to envision methods that could avoid a repulsive image force, such as including a full-description of the interband transitions. For example, future work can be done by using *ab initio* data of the in-plane conductivity over a broad range of frequencies. [90] It is worth mentioning that a repulsive image force was also obtained in works with a relativistic treatment of the particle beam, but the configuration of their target differs from ours. [126, 127] However, we recognize that a relativistic description of the particle’s trajectory as part of future research can help us gain insight on the nature of a repulsive image force, [128–130] especially for high particle speeds.

Lastly, we found that the main effect of the SiO_2 substrate was to reduce the magnitude of the three forces at speeds near their local extrema and to reduce the intensity of the anisotropy effect with respect to the direction of motion. Additionally, the image force approached a negative finite value and showed decreased angular dependence for speeds beyond $\bar{v} \approx 6$. Furthermore, the substrate eliminated the region where the image force became repulsive. Conversely, the transverse stopping force still had a large magnitude and strong anisotropy with the angular dependence. An implication of the latter finding is that the transverse force may be observable in carefully designed HREELS experiments using reflection of electrons with ~ 100 eV under grazing incidence. On the one hand, our approach meets some needs regarding the substrate of the system since it has been shown that the use of the bulk dielectric function suffices to capture all the essential features of its phonon spectra in HREELS using near-specular reflection under grazing incidence when the substrate exceeds 2–3 nm. [9, 10] On the other hand, an important limitation of our approach is that it is restricted to large distances separating the 2D material and the incident particle. Recall that this restriction allowed us to use conductivity models in the optical limit. Hence, the goal of future research would be to extend the validity to small distances, which could be attained by taking full account of non-local effects. For example, momentum dependent *ab initio* data for the conductivity of phosphorene may be used to numerically compute the forces on a full range of distances. Having a description for a full range of parameters bring us closer to simulate realistic trajectories of incident particles and to assess the role of a surface’s anisotropy in reflected electron spectra. For instance, a possible approach could be a Monte Carlo type simulation based in classical equations of motion for a particle that models grazing incidence upon phosphorene, which includes an anisotropic in-plane friction force that depends on speed and distance, while

the perpendicular motion is still treated adiabatically.

References

- [1] F. Hofer, F. P. Schmidt, W. Grogger, and G. Kothleitner, “Fundamentals of electron energy-loss spectroscopy”, *IOP Conference Series: Materials Science and Engineering* **109**, 012007 (2016).
- [2] O. Krivanek, N. Dellby, J. Hachtel, J. Idrobo, M. Hotz, B. Plotkin-Swing, N. Bacon, A. Bleloch, G. Corbin, M. Hoffman, C. Meyer, and T. Lovejoy, “Progress in ultrahigh energy resolution EELS”, *Ultramicroscopy* **203**, 60–67 (2019).
- [3] J. Lindon, *Encyclopedia of spectroscopy and spectrometry* (Elsevier Science, 2010).
- [4] R. J. Warmack, R. S. Becker, V. E. Anderson, R. H. Ritchie, Y. T. Chu, J. Little, and T. L. Ferrell, “Surface-plasmon excitation during aloof scattering of low-energy electrons in micropores in a thin metal foil”, *Phys. Rev. B* **29**, 4375–4381 (1984).
- [5] P. A. Crozier, “Vibrational and valence aloof beam EELS: a potential tool for nondestructive characterization of nanoparticle surfaces”, *Ultramicroscopy* **180**, 104–114 (2017).
- [6] F. S. Hage, R. J. Nicholls, J. R. Yates, D. G. McCulloch, T. C. Lovejoy, N. Dellby, O. L. Krivanek, K. Refson, and Q. M. Ramasse, “Nanoscale momentum-resolved vibrational spectroscopy”, *Science Advances* **4**, 10.1126/sciadv.aar7495 (2018).
- [7] H. Ibach and D. Mills, *Electron energy loss spectroscopy and surface vibrations* (Academic Press, New York, 1982).
- [8] P. Lambin, A. Lucas, and J. Vigneron, “On the role of the image force in the electron-energy-loss spectrum of a dielectric target”, *Surface Science* **182**, 567–575 (1987).
- [9] P. Senet, P. Lambin, J.-P. Vigneron, and I. D. A. A. Lucas, “Phonon surface loss function of ionic-crystal films: a comparison between microscopic and macroscopic approaches”, *Surface Science* **226**, 307–321 (1990).

- [10] P. Lambin, P. Senet, and A. A. Lucas, “Validity of the dielectric approximation in describing electron-energy-loss spectra of surface and interface phonons in thin films of ionic crystals”, *Phys. Rev. B* **44**, 6416–6428 (1991).
- [11] P. Lambin, L. Henrard, P. Thiry, C. Silien, and J. Vigneron, “The dielectric theory of HREELS, a short survey”, *Journal of Electron Spectroscopy and Related Phenomena* **129**, 281–292 (2003).
- [12] A. Politano and G. Chiarello, “Plasmon modes in graphene: status and prospect”, *Nanoscale* **6**, 10927–10940 (2014).
- [13] K. J. Snowdon, D. J. O’Connor, and R. J. MacDonald, “Observation of skipping motion in small-angle ion-surface scattering”, *Phys. Rev. Lett.* **61**, 1760–1763 (1988).
- [14] H. Winter, “Image charge effects in ion surface scattering”, *Journal of Physics: Condensed Matter* **8**, 10149–10183 (1996).
- [15] A. G. Borisov, A. Mertens, H. Winter, and A. K. Kazansky, “Evidence for the stopping of slow ions by excitations of optical phonons in insulators”, *Phys. Rev. Lett.* **83**, 5378–5381 (1999).
- [16] Y.-H. Song, Y.-N. Wang, and Z. L. Miskovic, “Energy loss of heavy ions specularly reflected from surfaces under glancing-angle incidence”, *Phys. Rev. A* **63**, 052902 (2001).
- [17] A. A. Lucas, M. Sunjic, and G. Benedek, “Multiple excitation of Fuchs–Kliewer phonons by Ne^+ ions back-scattered by the $\text{LiF}(100)$ surface at grazing incidence”, *Journal of Physics: Condensed Matter* **25**, 355009 (2013).
- [18] B. Jin, H. Zhou, Z. Zong, X. Zhang, G. Wang, L. Zhou, and X. Chen, “Negative ion formation by neutral hydrogen atom grazing scattering from a $\text{LiF}(100)$ surface”, *RSC Adv.* **11**, 4489–4498 (2021).
- [19] F. J. García de Abajo, “Optical excitations in electron microscopy”, *Reviews of Modern Physics* **82**, 209–275 (2010).
- [20] A. Polman, M. Kociak, and F. J. García de Abajo, “Electron-beam spectroscopy for nanophotonics”, *Nature Materials* **18**, 1158–1171 (2019).
- [21] R. F. Egerton, *Electron energy-loss spectroscopy in the electron microscope* (Springer, New York, 2011).
- [22] F. Huang, S. Fan, Y. Tian, X. Qu, X. Li, M. Qin, J. Muhammad, X. Zhang, Z. Zhang, and X. Dong, “Influence of n-doping on dielectric properties of carbon-coated copper nanocomposites in the microwave and terahertz ranges”, *Journal of Materiomics*, <https://doi.org/10.1016/j.jmat.2022.06.006> (2022).

- [23] K. Akbari, S. Segui, Z. L. Miskovic, J. L. Gervasoni, and N. R. Arista, “Energy losses and transition radiation in graphene traversed by a fast charged particle under oblique incidence”, *Phys. Rev. B* **98**, 195410 (2018).
- [24] M. Sunjic, G. Toulouse, and A. A. Lucas, “Dynamical corrections to the image potential”, *Solid State Communications* **11**, 1629–1631 (1972).
- [25] R. Ray and G. D. Mahan, “Dynamical image charge theory”, *Phys. Lett. A* **42**, 301–302 (1972).
- [26] J. Muscat and D. Newns, “Image force for a fast particle”, *Surface Science* **64**, 641–648 (1977).
- [27] P. M. Echenique, R. H. Ritchie, N. Barberán, and J. Inkson, “Semiclassical image potential at a solid surface”, *Phys. Rev. B* **23**, 6486–6493 (1981).
- [28] P. Echenique and A. Howie, “Image force effects in electron microscopy”, *Ultramicroscopy* **16**, 269–272 (1985).
- [29] D. Mills, “The image force on a moving charge; oblique and grazing incidence”, *Solid State Communications* **84**, A Festschrift Issue of Solid State Communication to Pay Tribute to Professor Ellias Burstein, 151–154 (1992).
- [30] N. R. Arista, “Dynamical image potential and induced forces for charged particles moving parallel to a solid surface”, *Phys. Rev. A* **49**, 1885–1896 (1994).
- [31] P. Sigmund, “Forces on swift ions near plane surfaces”, *Nuclear Instruments and Methods in Physics Research Section B: Beam Interactions with Materials and Atoms* **125**, Inelastic Ion-Surface Collisions, 77–96 (1997).
- [32] A. Reyes-Coronado, C. G. Ortíz-Solano, N. Zabala, A. Rivacoba, and R. Esquivel-Sirvent, “Analysis of electromagnetic forces and causality in electron microscopy”, *Ultramicroscopy* **192**, 80–84 (2018).
- [33] D. Borcka, S. Petrović, N. Nešković, D. J. Mowbray, and Z. L. Mišković, “Influence of the dynamical image potential on the rainbows in ion channeling through short carbon nanotubes”, *Phys. Rev. A* **73**, 062902 (2006).
- [34] Y. Liu, R. F. Willis, K. V. Emtsev, and T. Seyller, “Plasmon dispersion and damping in electrically isolated two-dimensional charge sheets”, *Phys. Rev. B* **78**, 201403 (2008).
- [35] Y. Liu and R. F. Willis, “Plasmon-phonon strongly coupled mode in epitaxial graphene”, *Phys. Rev. B* **81**, 081406 (2010).
- [36] R. J. Koch, T. Seyller, and J. A. Schaefer, “Strong phonon-plasmon coupled modes in the graphene/silicon carbide heterosystem”, *Phys. Rev. B* **82**, 201413 (2010).

- [37] T. Langer, D. F. Förster, C. Busse, T. Michely, H. Pfnür, and C. Tegenkamp, “Sheet plasmons in modulated graphene on ir(111)”, *New Journal of Physics* **13**, 053006 (2011).
- [38] R. J. Koch, S. Fryska, M. Ostler, M. Endlich, F. Speck, T. Hänsel, J. A. Schaefer, and T. Seyller, “Robust phonon-plasmon coupling in quasifreestanding graphene on silicon carbide”, *Phys. Rev. Lett.* **116**, 106802 (2016).
- [39] L. Ju, B. Geng, J. Horng, C. Girit, M. Martin, Z. Hao, H. A. Bechtel, X. Liang, A. Zettl, Y. R. Shen, and F. Wang, “Graphene plasmonics for tunable terahertz metamaterials”, *Nat. Nanotech.* **6**, 630 (2011).
- [40] H. Yan, X. Li, B. Chandra, G. Tulevski, Y. Wu, M. Freitag, W. Zhu, P. Avouris, and F. Xia, “Tunable infrared plasmonic devices using graphene/insulator stacks”, *Nat. Nanotech.* **7**, 330 (2012).
- [41] T. Low and P. Avouris, “Graphene Plasmonics for Terahertz to Mid-Infrared Applications”, *ACS Nano* **8**, 1086–1101 (2014).
- [42] P. Goncalves and N. Peres, *An introduction to graphene plasmonics* (World Scientific, Singapore, 2016).
- [43] A. Moradi, *Canonical problems in the theory of plasmonics* (Springer, Cham, 2020).
- [44] A. Politano, G. Chiarello, and C. Spinella, “Plasmon spectroscopy of graphene and other two-dimensional materials with transmission electron microscopy”, *Materials Science in Semiconductor Processing* **65**, Advanced transmission electron microscopy for semiconductor and materials science, 88–99 (2017).
- [45] T. Eberlein, U. Bangert, R. R. Nair, R. Jones, M. Gass, A. Bleloch, K. Novoselov, A. Geim, and P. Briddon, “Plasmon spectroscopy of free-standing graphene films”, *Phys. Rev. B* **77**, 233406 (2008).
- [46] V. B. Jovanovi, I. Radovic, D. Borka, and Z. L. Miskovic, “High-energy plasmon spectroscopy of freestanding multilayer graphene”, *Phys. Rev. B* **84**, 155416 (2011).
- [47] V. Despoja, D. Novko, K. Dekanic, M. Sunjic., and L. Marusic, “Two-dimensional and π plasmon spectra in pristine and doped graphene”, *Phys. Rev. B* **87**, 075447 (2013).
- [48] P. Wachsmuth, R. Hambach, M. K. Kinyanjui, M. Guzzo, G. Benner, and U. Kaiser, “High-energy collective electronic excitations in free-standing single-layer graphene”, *Phys. Rev. B* **88**, 075433 (2013).

- [49] F. Nelson, J.-C. Idrobo, J. Fite, Z. Miskovic, S. Pennycook, S. Pantelides, J. Lee, and A. Diebold, “Electronic excitations in graphene in the 1.50 eV range: the π and $\sigma + \pi$ peaks are not plasmons”, *Nano Lett.* **14**, 3827–3831 (2014).
- [50] S. Liou, C. Shie, C. Chen, R. Breitwieser, W. Pai, G. Guo, and M. Chu, “ π -plasmon dispersion in free-standing graphene by momentum-resolved electron energy-loss spectroscopy”, *Phys. Rev. B* **91**, 045418 (2015).
- [51] T. Djordjevic, I. Radovic, V. Despoja, K. Lyon, D. Borka, and Z. Miskovic, “Analytical modeling of electron energy loss spectroscopy of graphene: ab initio study versus extended hydrodynamic model”, *Ultramicroscopy* **184**, 134–142 (2018).
- [52] R. Senga, K. Suenaga, P. Barone, S. Morishita, F. Mauri, and T. Pichler, “Position and momentum mapping of vibrations in graphene nanostructures”, *Nature* **573**, 247–250 (2019).
- [53] Z.-Y. Ong and M. V. Fischetti, “Charged impurity scattering in top-gated graphene nanostructures”, *Phys. Rev. B* **86**, 121409 (2012).
- [54] Z. L. Mišković, P. Sharma, and F. O. Goodman, “Ionic screening of charged impurities in electrolytically gated graphene”, *Phys. Rev. B* **86**, 115437 (2012).
- [55] K. F. Allison and Z. L. Miskovic, “Friction force on slow charges moving over supported graphene”, *Nanotechnology* **21**, 134017 (2010).
- [56] Z. Fei, G. O. Andreev, W. Bao, L. M. Zhang, A. S. McLeod, C. Wang, M. K. Stewart, Z. Zhao, G. Dominguez, M. Thiemens, M. M. Fogler, M. J. Tauber, A. H. Castro-Neto, C. N. Lau, F. Keilmann, and D. N. Basov, “Infrared nanoscopy of Dirac plasmons at the graphene–SiO₂ interface”, *Nano Letters* **11**, PMID: 21972938, 4701–4705 (2011).
- [57] I. Radovic, V. B. Jovanovic, D. Borka, and Z. L. Miskovic, “Interactions of slowly moving charges with graphene: the role of substrate phonons”, *Nuclear Instruments and Methods in Physics Research Section B: Beam Interactions with Materials and Atoms* **279**, Proceedings of the Fifth International Conference on Elementary Processes in Atomic Systems Belgrade, Serbia, 21-25 June 2011, 165–168 (2012).
- [58] H. Yan, T. Low, W. Zhu, Y. Wu, M. Freitag, X. Li, F. Guinea, P. Avouris, and F. Xia, “Damping pathways of mid-infrared plasmons in graphene nanostructures”, *Nature Photonics* **7**, 394–399 (2013).
- [59] T. Marinkovic, I. Radovic, D. Borka, and Z. L. Miskovic, “Probing the plasmon-phonon hybridization in supported graphene by externally moving charged particles”, *Plasmonics* **10**, 1741–1749 (2015).

- [60] V. Despoja, T. Djordjevic, L. Karbunar, I. Radovic, and Z. L. Miskovic, “Ab initio study of the electron energy loss function in a graphene-sapphire-graphene composite system”, *Phys. Rev. B* **96**, 075433 (2017).
- [61] B. Li, C. Lai, G. Zeng, D. Huang, L. Qin, M. Zhang, M. Cheng, X. Liu, H. Yi, C. Zhou, F. Huang, S. Liu, and Y. Fu, “Black phosphorus, a rising star 2D nanomaterial in the post-graphene era: synthesis, properties, modifications, and photocatalysis applications”, *Small* **15**, 1804565 (2019).
- [62] F. Xia, H. Wang, and Y. Jia, “Rediscovering Black Phosphorus: A Unique Anisotropic 2D Material for Optoelectronics and Electronics”, *Nat. Commun.* **5**, 4458 (2014).
- [63] L. Li, Y. Yu, G. J. Ye, Q. Ge, X. Ou, H. Wu, D. Feng, X. H. Chen, and Y. Zhang, “Black phosphorus field-effect transistors”, *Nat. Nanotechnol.* **9**, 372 (2014).
- [64] H. Liu, A. T. Neal, Z. Zhu, Z. Luo, X. Xu, D. Tománek, and P. D. Ye, “Phosphorene: an unexplored 2D semiconductor with a high hole mobility”, *ACS Nano* **8**, 4033–4041 (2014).
- [65] X. Wang and S. Lan, “Optical properties of black phosphorus”, *Adv. Opt. Photon.* **8**, 618–655 (2016).
- [66] W. Ma, P. Alonso-Gonzalez, S. Li, A. Y. Nikitin, J. Yuan, J. Martin-Sanchez, J. Taboada-Gutierrez, I. Amenabar, P. Li, S. Velez, C. Tollan, Z. Dai, Y. Zhang, S. Sriram, K. Kalantar-Zadeh, S.-T. Lee, R. Hillenbrand, and Q. Bao, “In-plane anisotropic and ultra-low-loss polaritons in a natural van der waals crystal”, *Nature* **562**, 557–562 (2018).
- [67] X. Chen, J. S. Ponraj, D. Fan, and H. Zhang, “An overview of the optical properties and applications of black phosphorus”, *Nanoscale* **12**, 3513–3534 (2020).
- [68] H. Liu, A. T. Neal, M. Si, Y. Du, and P. D. Ye, “The effect of dielectric capping on few-layer phosphorene transistors: tuning the schottky barrier heights”, *IEEE Electron Device Letters* **35**, 795–797 (2014).
- [69] C. Wang, G. Zhang, S. Huang, Y. Xie, and H. Yan, “The optical properties and plasmonics of anisotropic 2D materials”, *Advanced Optical Materials* **8**, 1900996 (2020).
- [70] P. Shekhar, J. Atkinson, and Z. Jacob, “Hyperbolic metamaterials: fundamentals and applications”, *Nano Convergence* **1**, 14 (2014).
- [71] J. S. Gomez-Diaz and A. Alú, “Flatland optics with hyperbolic metasurfaces”, *ACS Photonics* **3**, 2211–2224 (2016).

- [72] B. Deng, R. Frisenda, C. Li, X. Chen, A. Castellanos-Gomez, and F. Xia, “Progress on black phosphorus photonics”, *Advanced Optical Materials* **6**, 1800365 (2018).
- [73] J. Miao, L. Zhang, and C. Wang, “Black phosphorus electronic and optoelectronic devices”, *2D Materials* **6**, 032003 (2019).
- [74] T. Low, A. S. Rodin, A. Carvalho, Y. Jiang, H. Wang, F. Xia, and A. H. Castro Neto, “Tunable optical properties of multilayer black phosphorus thin films”, *Phys. Rev. B* **90**, 075434 (2014).
- [75] T. Low, R. Roldán, H. Wang, F. Xia, P. Avouris, L. M. Moreno, and F. Guinea, “Plasmons and screening in monolayer and multilayer black phosphorus”, *Phys. Rev. Lett.* **113**, 106802 (2014).
- [76] J. Kim, S. S. Baik, S. H. Ryu, Y. Sohn, S. Park, B.-G. Park, J. Denlinger, Y. Yi, H. J. Choi, and K. S. Kim, “Observation of tunable band gap and anisotropic dirac semimetal state in black phosphorus”, *Science* **349**, 723–726 (2015).
- [77] D. T. Debu, S. J. Bauman, D. French, H. O. Churchill, and J. B. Herzog, “Tuning infrared plasmon resonance of black phosphorene nanoribbon with a dielectric interface”, *Sci. Rep.* **8**, 3224 (2018).
- [78] E. van Veen, A. Nemilentsau, A. Kumar, R. Roldán, M. I. Katsnelson, T. Low, and S. Yuan, “Tuning two-dimensional hyperbolic plasmons in black phosphorus”, *Phys. Rev. Applied* **12**, 014011 (2019).
- [79] J. S. Gomez-Diaz, M. Tymchenko, and A. Alù, “Hyperbolic plasmons and topological transitions over uniaxial metasurfaces”, *Phys. Rev. Lett.* **114**, 233901 (2015).
- [80] D. Correas-Serrano, J. S. Gomez-Diaz, A. A. Melcon, and A. Alú, “Black phosphorus plasmonics: anisotropic elliptical propagation and nonlocality-induced canalization”, *Journal of Optics* **18**, 104006 (2016).
- [81] A. Nemilentsau, T. Low, and G. Hanson, “Anisotropic 2D materials for tunable hyperbolic plasmonics”, *Phys. Rev. Lett.* **116**, 066804 (2016).
- [82] Z. Su and Y. Wang, “Anisotropic photonics topological transition in hyperbolic metamaterials based on black phosphorus”, *Nanomaterials* **10**, 1694 (2020).
- [83] S. A. Hassani Gangaraj, T. Low, A. Nemilentsau, and G. W. Hanson, “Directive surface plasmons on tunable two-dimensional hyperbolic metasurfaces and black phosphorus: green’s function and complex plane analysis”, *IEEE Transactions on Antennas and Propagation* **65**, 1174–1186 (2017).

- [84] A. Nemilentsau, T. Stauber, G. Gómez-Santos, M. Luskun, and T. Low, “Switchable and unidirectional plasmonic beacons in hyperbolic two-dimensional materials”, *Phys. Rev. B* **99**, 201405 (2019).
- [85] H. Hajian, I. D. Rukhlenko, G. W. Hanson, T. Low, B. Butun, and E. Ozbay, “Tunable plasmon-phonon polaritons in anisotropic 2D materials on hexagonal boron nitride”, *Nanophotonics* **9**, 3909–3920 (2020).
- [86] S. Xiao, T. Liu, L. Cheng, C. Zhou, X. Jiang, Z. Li, and C. Xu, “Tunable anisotropic absorption in hyperbolic metamaterials based on black phosphorous/dielectric multilayer structures”, *J. Lightwave Technol.* **37**, 3290–3297 (2019).
- [87] R. J. Wu, M. Topsakal, T. Low, M. C. Robbins, N. Haratipour, J. S. Jeong, R. M. Wentzcovitch, S. J. Koester, and K. A. Mkhoyan, “Atomic and electronic structure of exfoliated black phosphorus”, *Journal of Vacuum Science & Technology A* **33**, 060604 (2015).
- [88] B. Ghosh, P. Kumar, A. Thakur, Y. S. Chauhan, S. Bhowmick, and A. Agarwal, “Anisotropic plasmons, excitons, and electron energy loss spectroscopy of phosphorene”, *Phys. Rev. B* **96**, 035422 (2017).
- [89] E. Gaufrés, F. Fossard, V. Gosselin, L. Sponza, F. Ducastelle, Z. Li, S. G. Louie, R. Martel, M. Côté, and A. Loiseau, “Momentum-resolved dielectric response of free-standing mono-, bi-, and trilayer black phosphorus”, *Nano Letters* **19**, PMID: 31603690, 8303–8310 (2019).
- [90] D. Novko, K. Lyon, D. J. Mowbray, and V. Despoja, “Ab initio study of electromagnetic modes in two-dimensional semiconductors: application to doped phosphorene”, *Phys. Rev. B* **104**, 115421 (2021).
- [91] O. H. Crawford, “Directional effects on the motion of swift ions in anisotropic media”, *Phys. Rev. A* **42**, 1390–1395 (1990).
- [92] C. Maciel-Escudero, A. Konečná, R. Hillenbrand, and J. Aizpurua, “Probing and steering bulk and surface phonon polaritons in uniaxial materials using fast electrons: hexagonal boron nitride”, *Phys. Rev. B* **102**, 115431 (2020).
- [93] K. F. Allison, D. Borka, I. Radovic, L. Hadzievski, and Z. L. Miskovic, “Dynamic polarization of graphene by moving external charges: random phase approximation”, *Phys. Rev. B* **80**, 195405 (2009).
- [94] I. Radovic, L. Hadzievski, and Z. L. Miskovic, “Polarization of supported graphene by slowly moving charges”, *Phys. Rev. B* **77**, 075428 (2008).

- [95] N. Kang, “Green’s function for Poisson equation in layered nano-structures including graphene”, MA thesis (University of Waterloo, 2015).
- [96] R. Anicic, “Effects of the dielectric environment on the electrical properties of graphene”, MA thesis (University of Waterloo, 2013).
- [97] B. Wunsch, T. Stauber, F. Sols, and F. Guinea, “Dynamical polarization of graphene at finite doping”, *New Journal of Physics* **8**, 318–318 (2006).
- [98] E. H. Hwang and S. Das Sarma, “Dielectric function, screening, and plasmons in two-dimensional graphene”, *Phys. Rev. B* **75**, 205418 (2007).
- [99] D. Zill, W. Wright, and M. Cullen, *Advanced engineering mathematics*, Jones and Bartlett Publishers series in mathematics: Advanced engineering mathematics (Jones & Bartlett Learning, 2011).
- [100] L. Landau and E. Lifshitz, *Statistical physics: volume 5* (Elsevier Science, 2013).
- [101] M. R. Preciado Rivas, M. Moshayedi, and Z. L. Mišković, “On the role of the energy loss function in the image force on a charge moving over supported graphene”, *Journal of Applied Physics* **130**, 173103 (2021).
- [102] M. N. Gjerding, L. S. R. Cavalcante, A. Chaves, and K. S. Thygesen, “Efficient ab initio modeling of dielectric screening in 2D van der waals materials: including phonons, substrates, and doping”, *The Journal of Physical Chemistry C* **124**, 11609–11616 (2020).
- [103] H. Ehrenreich and M. H. Cohen, “Self-consistent field approach to the many-electron problem”, *Phys. Rev.* **115**, 786–790 (1959).
- [104] A. Hill, S. A. Mikhailov, and K. Ziegler, “Dielectric function and plasmons in graphene”, *EPL (Europhysics Letters)* **87**, 27005 (2009).
- [105] V. A. Margulis and E. E. Muryumin, “Theory for surface polaritons supported by a black-phosphorus monolayer”, *Phys. Rev. B* **98**, 165305 (2018).
- [106] G. Lovat, G. W. Hanson, R. Araneo, and P. Burghignoli, “Semiclassical spatially dispersive intraband conductivity tensor and quantum capacitance of graphene”, *Phys. Rev. B* **87**, 115429 (2013).
- [107] A. M. Holmes and G. W. Hanson, “Conditions for photonic bandgaps in two-dimensional materials”, *Journal of Applied Physics* **129**, 015302 (2021).
- [108] L. A. Falkovsky and S. S. Pershoguba, “Optical far-infrared properties of a graphene monolayer and multilayer”, *Phys. Rev. B* **76**, 153410 (2007).

- [109] S. Das Sarma, S. Adam, E. H. Hwang, and E. Rossi, “Electronic transport in two-dimensional graphene”, *Rev. Mod. Phys.* **83**, 407–470 (2011).
- [110] S. Biswas, W. S. Whitney, M. Y. Grajower, K. Watanabe, T. Taniguchi, H. A. Bechtel, G. R. Rossman, and H. A. Atwater, “Tunable intraband optical conductivity and polarization-dependent epsilon-near-zero behavior in black phosphorus”, *Science Advances* **7**, eabd4623 (2021).
- [111] S. Biswas, M. Y. Grajower, K. Watanabe, T. Taniguchi, and H. A. Atwater, “Broadband electro-optic polarization conversion with atomically thin black phosphorus”, *Science* **374**, 448–453 (2021).
- [112] N. M. Peres, “Graphene, new physics in two dimensions”, *Europhysics News* **40**, 17–20 (2009).
- [113] A. K. Geim and K. S. Novoselov, “The rise of graphene”, *Nature Materials* **6**, 183–191 (2007).
- [114] D. Novko, M. Šunjić, and V. Despoja, “Optical absorption and conductivity in quasi-two-dimensional crystals from first principles: Application to graphene”, *Physical Review B* **93**, 125413 (2016).
- [115] P. Cudazzo, I. V. Tokatly, and A. Rubio, “Dielectric screening in two-dimensional insulators: implications for excitonic and impurity states in graphene”, *Phys. Rev. B* **84**, 085406 (2011).
- [116] A. S. Rodin, A. Carvalho, and A. H. Castro Neto, “Excitons in anisotropic two-dimensional semiconducting crystals”, *Phys. Rev. B* **90**, 075429 (2014).
- [117] S. Ahn and S. Das Sarma, “Theory of anisotropic plasmons”, *Phys. Rev. B* **103**, L041303 (2021).
- [118] N. D. Mermin, “Lindhard dielectric function in the relaxation-time approximation”, *Phys. Rev. B* **1**, 2362–2363 (1970).
- [119] P. L. Bhatnagar, E. P. Gross, and M. Krook, “A model for collision processes in gases. i. small amplitude processes in charged and neutral one-component systems”, *Phys. Rev.* **94**, 511–525 (1954).
- [120] A. Srivastava, “Causality and passivity: from electromagnetism and network theory to metamaterials”, *Mechanics of Materials* **154**, 103710 (2021).
- [121] G. E. Jellison and F. A. Modine, “Parameterization of the optical functions of amorphous materials in the interband region”, *Applied Physics Letters* **69**, 371–373 (1996).

- [122] M. V. Fischetti, D. A. Neumayer, and E. A. Cartier, “Effective electron mobility in si inversion layers in metal–oxide–semiconductor systems with a high-k insulator: the role of remote phonon scattering”, *Journal of Applied Physics* **90**, 4587–4608 (2001).
- [123] D. A. Kirzhnits, “General properties of electromagnetic response functions”, *Soviet Physics Uspekhi* **30**, 575–587 (1987).
- [124] K. Akbari, Z. L. Miskovic, S. Segui, J. L. Gervasoni, and N. R. Arista, “Energy losses and transition radiation in multilayer graphene traversed by a fast charged particle”, *ACS Photonics* **4**, 1980–1992 (2017).
- [125] A. N. Rudenko, S. Brener, and M. I. Katsnelson, “Intrinsic charge carrier mobility in single-layer black phosphorus”, *Phys. Rev. Lett.* **116**, 246401 (2016).
- [126] I. Carmeli, M. A. Itskovsky, Y. Kauffmann, Y. Shaked, S. Richter, T. Maniv, and H. Cohen, “Far- and near-field electron beam detection of hybrid cavity-plasmonic modes in gold microholes”, *Phys. Rev. B* **85**, 041405 (2012).
- [127] P. R. Ribic, “Can a metal surface repel electric charges?”, *Phys. Rev. Lett.* **109**, 244801 (2012).
- [128] A. Rivacoba and N. Zabala, “Relativistic force between fast electrons and planar targets”, *New Journal of Physics* **16**, 073048 (2014).
- [129] K. Akbari, Z. L. Miskovic, S. Segui, J. L. Gervasoni, and N. R. Arista, “Energy losses and transition radiation in multilayer graphene traversed by a fast charged particle”, *ACS Photonics* **4**, 1980–1992 (2017).
- [130] Z. L. Miskovic, K. Akbari, S. Segui, J. L. Gervasoni, and N. R. Arista, “Relativistic effects in the energy loss of a fast charged particle moving parallel to a two-dimensional electron gas”, *Nuclear Instruments and Methods in Physics Research Section B: Beam Interactions with Materials and Atoms* **422**, 18–23 (2018).